# Investigation of Microstructure, Heat Treatment and Hydroxyapatite Addition in Selective Laser Melting of Ti6Al4V Alloys

A Ph.D. Dissertation submitted in partial fulfillment of the requirements for the degree of Doctor of Philosophy in Materials Science and Engineering

**By**
**Hassanen L. Jaber**
M.Sc. in Materials Sciences and Engineering

**Supervisor**
**Dr. Kovács Tünde**

ÓBUDAI EGYETEM
ÓBUDA UNIVERSITY

**Óbuda University, Doctoral School of Materials Sciences and Technologies**

Budapest, Hungary
2022

# Abstract

Additive manufacturing, particularly selective laser melting (SLM), is an important process in biomedical engineering applications due to the SLM technology has the potential to produce functionally graded materials, lattice structures, and complex structures. Titanium alloys, particularly Ti6Al4V (Ti64), are among the most widely used materials in biomedical engineering due to their high biocompatibility, excellent corrosion resistance, and low elastic modulus (110 GPa).

One of the main topics in the literature on SLM of Ti64 for biomedical implants is the formation of an α′-martensitic microstructure. It has been experimentally demonstrated that SLM parts that are fully α′ martensitic have low ductility of less than 10%. In addition, residual stresses are associated with the formation of an α′ martensitic structure, resulting in lower mechanical performance. However, according to ASTM F13-12a and ASTM F2924-14, the microstructure of an implant or SLM part must have a minimum strain of 10% and an alpha (α)-beta (β) dual phase. Therefore, there is clearly a practical need to study the microstructure development and mechanical performance of heat treatment of SLM parts. The results show that heat treatment at 850 ℃ followed by furnace cooling gives the optimal possible combination of ductility and strength properties, and the microstructure consists of β and α phases among other heat treatments.

Bone resorption is a process of bone loss resulting from the large difference in Young's modulus between bone (10-30 GPa) and the Ti64 implant (105-110 GPa) in younger patients under 40 years of age. The significant difference in Young's modulus results in a non-gradual transfer of stresses to the bone surrounding the implant, leading to stress shielding and thus bone absorption. Stability and fixation of the Ti64 implant inside the bone and bone ingrowth at the interface are the main challenges after the implantation. To improve or enhance bone formation, accelerate bonding, and achieve good interfacial bonding between bone tissue and metal implants, new composite materials of Ti64 and hydroxyapatite (HA) are needed. It is well known that the crystallographic and chemical composition of HA ($Ca_{10}(PO_4)_6(OH)_2$) is similar to that of bone tissue, which can greatly improve osseointegration and biological fixation. Other advantages of HA that could reduce inflammatory reactions or allergic risks and accelerate bonding are bioactive, biocompatible, non-inflammatory, non-toxic, non-immunogenic and osteoconductive.

The results showed that the microstructure of SLM of Ti64 -2% HA composite was a complex mixture of α Ti, HA, $Ti_3P$, $Ti_xO$, P and $CaTiO_3$. The average volume fraction of HA in the microstructure of Ti64 -2% HA was about 10%, based on the software Image J. The formation of HA and dispersed Ca, P and O elements in the microstructure of implants may lead to a higher tendency of good bone osseointegration and biocompatibility.

One of the main barriers to using spherical titanium powder in powder bed additive manufacturing is that it is often very expensive. Irregularly shaped hydride dehydride (HDH) powder is a less expensive product than spherical titanium powder. Therefore, it is necessary to determine whether the hybrid powder of Ti64, which consists of 50% by weight of a plasma atomized (PA) spherical powder and 50% by weight of an irregularly shaped HDH powder with a flowability of 36.5 s, can be printed without affecting the microstructural and mechanical properties of the components produced by the SLM system. It was shown that the reduction of the powder flowability leads to an increased susceptibility to the formation of lack of fusion defects with decreasing tensile properties. The results of this study would seem to suggest that the absence of lack of fusion defects can be reduced by using the double scanning or remelting strategy.

# Acknowledgements

It gives me great pleasure to seize this opportunity to express my sincere gratitude and thankfulness to my supervisor, ***Dr. Kovács Tünde***, for her continuous supervision, inspiring and valuable advice, encouragement, and great sacrifices throughout my academic and research journey. My experience was greatly influenced and enhanced by the approach of ***Dr. Kovács Tünde*** whereby we shared many moments of laughter, beneficial discourse, and memories of trips to Győr and Miskolc. I will forever be grateful for the value ***Dr. Kovács Tünde*** has added to my learning experience.

I gratefully acknowledge the help provided by ***Mr. Kónya János*** for providing of laboratory facilities at the Dent-Art-Technik Center in Győr, without his help this work would never have been possible. I also thank ***Prof. Z. Dankházi*** (ELTE TTK.hu) for his collaboration and support in scanning electron microscopy work. I am grateful to ***Prof. Ján Dusza*** for his collaboration and support in X-ray diffraction test. The author wishes to thank ***Prof. Paulo Quadros*** (fluidinova.com), who provide us hydroxyapatite and gave us much valuable advice in the early stages of this work. The authors give special thanks to the staff in the ***Toho titanium co. ltd/Japan*** for providing hybrid powder and information regarding the manufacture of hybrid powder. I would also like to thank the Director of the PhD School, ***Prof. Judit Borsa***, and the ***Prof. Réger Mihály*** who provided me with useful tips, advice, motivation, or support during my PhD process. My thanks to ***Hersics Katalin***, and all the Óbuda University staff. I would also like to thank ***Mr. Lajos Bozsanyi*** from Dent-Art-Technik center for assisting me in performing the SLM procedure, and ***Dr. Fábián Enikő Réka*** and ***Ms. Huszák Csenge, MSc*** from Banki faculty for helping me at many various tasks and experiments related to my work.

I would like to express my profound gratitude to my beloved Mum, ***Kulah Hyder***, and my brothers and sister, for their support, good wishes, endless encouragement, and the many sacrifices they have made over the years to bring me to where I am now.

I am forever in their debt. Finally, I have no words to express my appreciation to my lovely and beautiful wife ***Athraa*** for her love, motivation, support, tolerance, patience, and enthusiasm during my research. Her constant encouragement has made this work possible. I am deeply grateful to my daughter ***Fatmah*** and my son ***Hydrah***, who always managed to relieve me of all stress with their kindness and fun.

# Contents

Abstract ..... II

Acknowledgements ..... IV

1 Introduction ..... 1

1.1 Additive Manufacturing ..... 1

1.1.1 Selective laser melting (SLM) ..... 2

1.2 Metallic Implant Materials ..... 7

1.2.1 Titanium Alloys ..... 7

1.3 Hydroxyapatite Bio-Ceramic ..... 10

1.4 Current issues and problems of metallic implant materials ..... 11

1.5 Selective laser melting of composite Ti – Hydroxyapatite. ..... 14

1.6 Microstructural evolution in 3D printing of Ti alloys ..... 17

1.6.1 Chemical composition ..... 17

1.6.2 Cooling rates ..... 18

1.7 Thesis Objectives ..... 19

2 Heat Treatments of SLM Ti6Al4V ..... 22

2.1 Introduction ..... 22

2.2 Objective ..... 23

2.3 Microstructure of Ti6Al4V ..... 23

2.4 Materials and Methods ..... 24

2.4.1 Materials preparation ..... 24

2.4.2 Heat treatments processes ..... 25

2.4.3 Materials characterization ..... 26

2.5 Results and Discussion ..... 27

2.5.1 Microstructure investigation ..... 27

2.5.2 Tensile properties ..... 47
2.6 Conclusions ..... 48
3 Selective Laser Melting of Ti6Al4V-Hydroxyapatite ..... 50
3.1 Introduction ..... 50
3.2 Objective ..... 51
3.3 Materials and Methods ..... 51
3.3.1 Materials preparation ..... 51
3.3.2 SLM system and processing ..... 52
3.3.3 Materials characterization ..... 53
3.4 Results and Discussion ..... 53
3.4.1 Material behavior during the SLM process of Ti6Al4V -HA composites ..... 53
3.4.2 Phase structure evolution ..... 55
3.4.3 Mechanical properties ..... 63
3.5 Conclusions of the SLM of Ti6Al4V-Hydroxyapatite ..... 65
4 SLM Process on Ti6Al4V Alloy Hybrid Powders with Spherical and Irregular Shapes ..... 66
4.1 Introduction ..... 66
4.2 Objective ..... 66
4.3 Experimental work ..... 68
4.4 Results and Discussion ..... 70
4.4.1 Formation of defects in building sample ..... 70
4.4.2 Mechanical performance ..... 72
4.4.3 Metallurgical characteristic ..... 73
4.5 Conclusion ..... 77
5 Summary of New Scientific Results ..... 78
6 List of Publications ..... 80

6.1 Articles in internationally reviewed academic journals ..... 80

6.2 Papers at international scientific conferences ..... 80

6.3 Unrelated publications in other scientific fields ..... 81

7 Future studies ..... 82

Figures ..... 83

Tables ..... 87

Bibliography ..... 88

# Abbreviations

| Variable | Description |
|---|---|
| Ti6Al4V (Ti64) | Titanium -6 Aluminum -4 Vanadium |
| HA | Hydroxyapatite |
| AM | Additive Manufacturing |
| 3D | 3-Dimensional |
| ASTM | American Society of Testing and Materials |
| ISO | International Organization for Standards |
| STL | Stereolithography |
| SLM | Selective Laser Melting |
| FGM | Functionally Graded Material |
| FGS | Functionally Graded Structure |
| FGMs | Functionally Graded Material and Structure |
| XRD | X-Ray Diffraction |
| EDX | Energy-dispersive X-Ray Spectroscopy |
| SEM | Scanning Electron Microscope |
| BSE | Backscattered Electrons |
| HDH | hydride dehydride |
| FC | Furnace Cooling |
| WC | Water cooling |
| HT850FC | Heat treatment at 850 ºC followed by furnace cooling |
| HT1020FC | Heat treatment at 1020 ºC followed by furnace cooling |
| HT850WC | Heat treatment at 850 ºC followed by water cooling |
| HT1020WC | Heat treatment at 1020 ºC followed by water cooling |
| HT850WC+AG | Heat treatment at 850 ºC followed by water cooling and ageing |
| HT1020WC+AG | Heat treatment at 1020 ºC followed by water cooling and ageing |

# Nomenclature

| Titanium Metallurgy | |
|---|---|
| Symbol | Definition |
| α | A hexagonal close-packed crystalline phase of Titanium and its alloys. Stable below the beta transus ($\beta_{tr} = 975^{\circ}C$). |
| β | A body-centered cubic crystalline phase of Titanium and its alloys. Stable above the beta transus ($\beta_{tr} = 975^{\circ}C$). |
| α + β | Titanium with a microstructure containing α and β, stable below the beta transus. |
| α′ | α′ (Martensitic) is a supersaturated substitutional solid solution of elements (vanadium) in a hexagonal close-packed crystalline system of the (α) phase. It is a hard phase that can form during the quenching of Titanium. |
| α″ | orthorhombic martensitic phase of Titanium alloys. |
| Beta transus ($\beta_{tr} = 975^{\circ}C$) | The temperature that designates the phase boundary between the α and α + β fields. |

# 1 Introduction

## 1.1 Additive Manufacturing

Additive manufacturing (AM) or 3D printing is defined as the technologies for manufacturing 3D components by adding/welding the material layer by layer using computer software (CAD model) [1]. As shown in Figure 1-1, the ASTM/ISO 52900-2015 standard [2] divides the additive manufacturing into seven kinds: Powder Bed Fusion (PBF), Directed Energy Deposition (DED), Binder Jetting, Material Extrusion, Sheet Lamination, Material Jetting, and Vat Polymerization. Only four of these seven kinds are used for metal printing. These include PBF, DED, sheet lamination and binder jetting. Only the first three of these four kinds are used for printing titanium and its alloys [3]. PBF is widely considered the most important technology, which also includes selective laser melting (SLM), selective laser sintering (SLS), and electron beam melting (EBM). PBF is divided into four stages: Creation of the CAD model, conversion of the CAD model into an STL (Standard Triangulation Language) file, slicing of the STL file, and layer by layer printing. A brief schematic of the PBF process is shown in Figure 1-2.

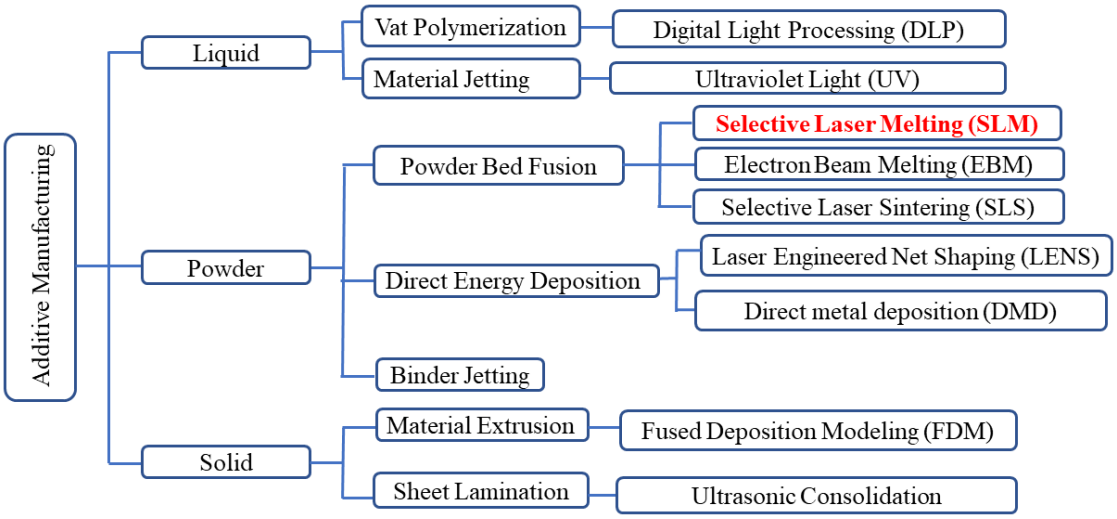


*Figure 1-1: Classification of AM technologies.*

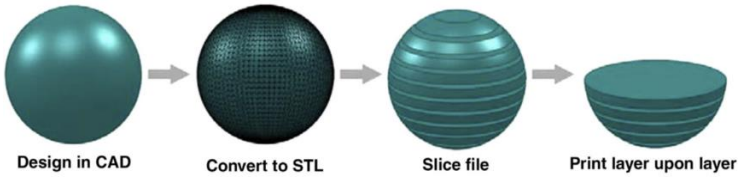


*Figure 1-2: Powder bed fusion (PBF)process flow* [4].

Despite the fact that there are many advanced additive manufacturing techniques, such as Electron Beam Melting (EBM) and Direct Energy Deposition, the Selective Laser Melting (SLM) is the preferred process in the powder bed melting family [5]. The key features of the SLM process are high precision, high manufacturing speed and additional degrees of freedom in the design of complex structures [6].

### 1.1.1 Selective laser melting (SLM)

Selective laser melting (SLM) is an additive manufacturing process in which heat is generated by the absorptivity of the powder material to be bonded under laser irradiation [7]. In this process, the powder material is heated and melted beyond the melting point, and this molten material rapidly solidifies to form the desired part. The laser beam is generated in a continuous single mode laser with a wavelength of 1075 nm via a Nd:YAG or Yb:YAG crystal. The generated laser is selectively scanned onto the surface of the powder layer via optics and a scanner system. Once a single layer has been scanned, the powder conditioner places a new layer on top of the previous layer for the beam to scan. The process repeats layer by layer until the product is finished, as shown in Figure 1-3. The experimental setup for this system is shown in Figure 1-4.

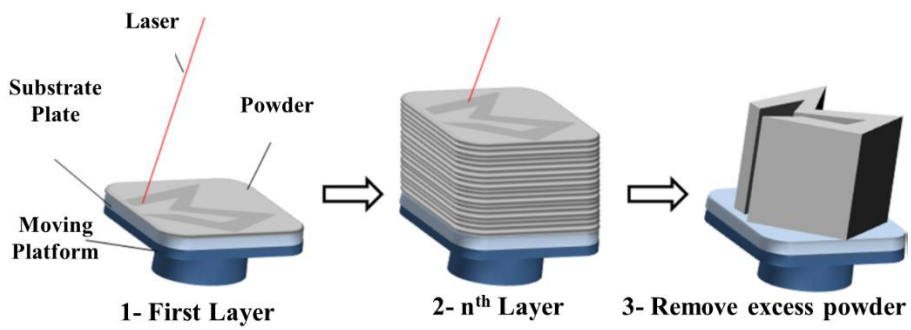


*Figure 1-3:Concept of SLM process* [7].

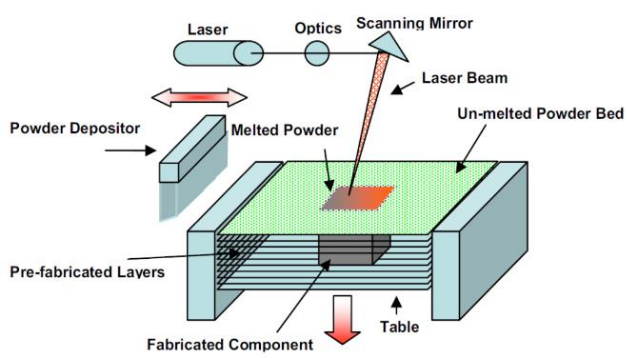


*Figure 1-4: The experimental setup of Selective Laser Melting (SLM)* [8].

Selective laser sintering (SLS) is a solid-state additive manufacturing process that produces compounds by solid-state sintering or melting of binders into the material powder [7]. The binders melt at lower laser energies, allowing the material powder particles to sinter. This process involves heating and softening the powder material below the melting point, and this softened material rapidly solidifies to form the desired part.

SLM is a complex process in which a large number of parameters can affect the mechanical performance and microstructure of the final part, as shown in Figure 1-5. Layer thickness, scan speed, hatch spacing, and laser power (Figure 1-6) are the main input parameters that affect the energy density of the laser beam impinging on the molten powder layer and influence the quality of the final part [7, 9].

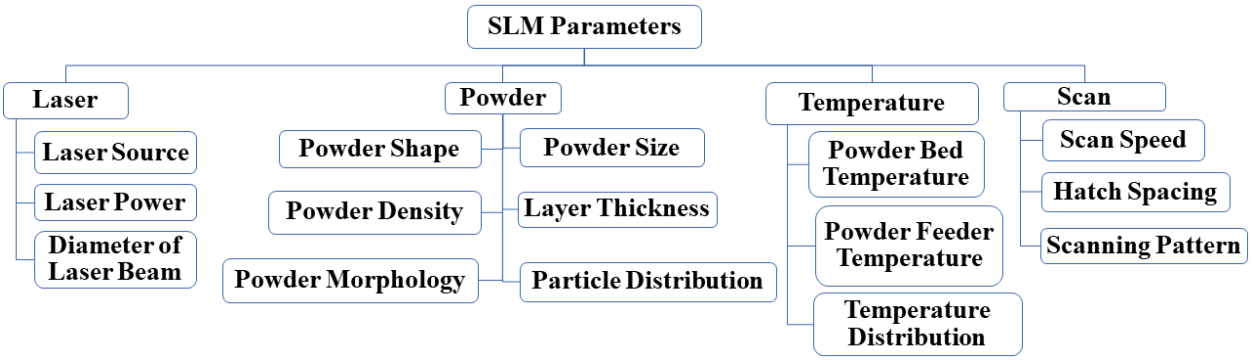


*Figure 1-5: Parameters in SLM process*[10].

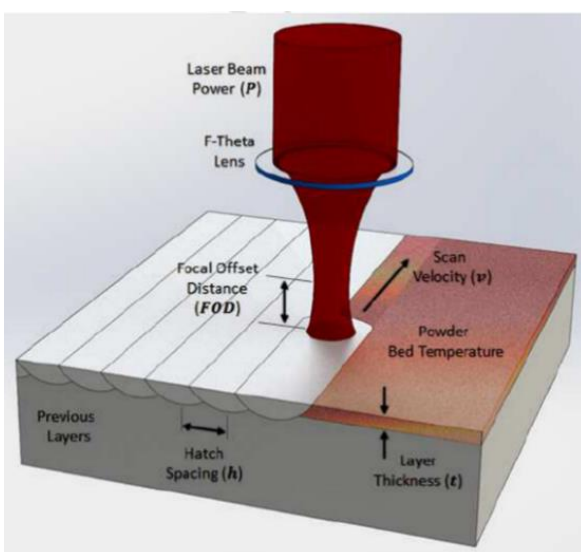


*Figure 1-6: Schematic diagram of SLM process parameters: laser power, scanning speed, hatch spacing, and layer thickness* [11].

#### *1.1.1.1 Applications of SLM Technology*

SLM has many applications in the biomedical, automotive, and aerospace fields. Figure 1-7 shows medical implants such as dental prosthesis, 3-unit dental bridges, and hip stems made with SLM technology. Automotive applications made with SLM technology include oil pump housings, exhaust manifolds, and water pumps for a motor sports car (see Figure 1-8). Aerospace metal parts made with SLM technology include the flight crew rest compartment bracket, engine housing, and turbine blade, as shown in Figure 1-9.

*Figure 1-7: Biomedical parts: (a) and (b) Dental prosthesis manufactured by SLM* [12], *(c) 3-unit dental bridge manufactured by SLM* [13], *and (d) Hip stems manufactured by EBM* [13].

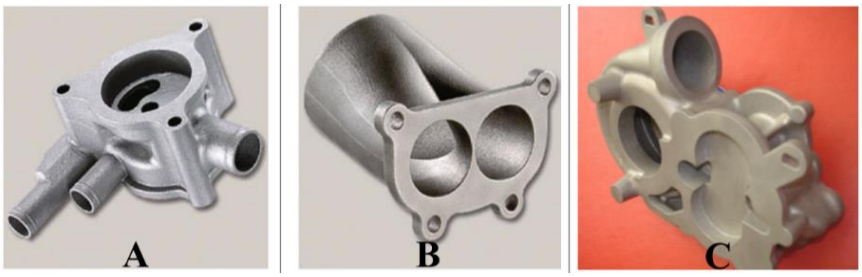


*Figure 1-8: Automotive parts manufactured by SLM technology* [13]*: (a) Oil pump housing, (b) Exhaust manifold, and (c) Water pump for a motorsport's car.*

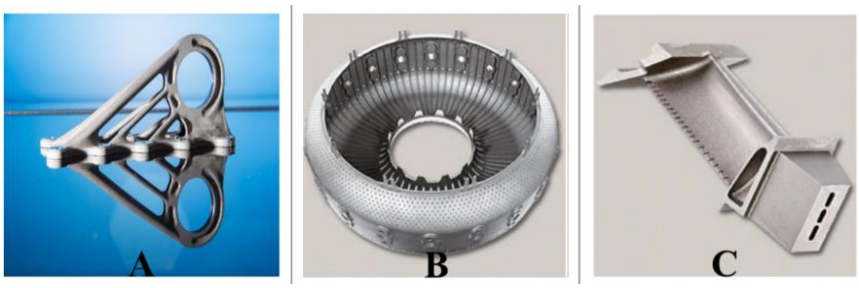


*Figure 1-9: Aerospace parts manufactured by SLM technology: (a) Flight crew rest compartment bracket* [14], *(b) Engine housing* [13], *and (c) Turbine blade with internal cooling channels*[13].

#### *1.1.1.2 Features of SLM Technology*

Due to the increasing use of functionally graded materials (FGM) and functionally graded structures (FGS) in the biomedical applications, the use of SLM processes is rapidly increasing. From this, the advantages of SLM compared to conventional manufacturing can be derived.

- SLM is capable of creating functional parts with high osseointegration, including a porosity gradient or lightweight scaffold structures, a microstructure gradient, and a chemical composition gradient.
- Titanium is highly reactive and sensitive to oxygen, nitrogen, hydrogen, and carbon in the liquid state or when heated in air to temperatures above 650°C. For these reasons, conventional manufacturing processes (such as casting) and welding of titanium are very difficult. The SLM process uses a laser beam with sufficient energy density to melt and fuse a small, localized area of titanium powder (rapid heating) and to rapidly cool the molten titanium to reduce the uptake of oxygen, carbon and hydrogen. In addition, a protective shield, such as an inert gas, is used to displace atmospheric air and prevent embrittlement and contamination by nitrogen and oxygen.
- Special designs are preferred for most anatomical processes, and in some cases these are complex shapes with thin-walled sections and curvatures. These designs can be easily fabricated using SLM techniques, as the design process in SLM has additional degrees of freedom.
- Cost savings: since no highly skilled personnel, molds, dies and equipment are required, manufacturing costs are reduced.
- Environmentally friendly: AM is an environmentally friendly process as little waste is produced during manufacture.

#### *1.1.1.3 Unfavorable Issues and Defects of SLM*

The major drawbacks in SLM of materials are the high probability of failure due to balling [15, 16], lack of fusion (unmelted particles) [17], and keyholing [18, 19] depending on the parameters of the SLM process. As mentioned above, the energy density of the laser beam, which is crucial for the formation of the molten pool, is determined by the energy input, which in turn is controlled by the SLM parameters. Therefore, the SLM parameters, especially the layer thickness, scan speed, hatch spacing and laser power, which determine the energy density of the

laser beam, should be adjusted to achieve sufficient energy density. In general, there is an optimum energy density of the laser beam to obtain a high-quality SLM product. It is known that increasing the energy density by decreasing the layer thickness and scan speed or increasing the laser power improves the mechanical properties, mainly due to the reduction of balling and porosity. On the other hand, increasing the energy density beyond a critical range has a negative effect on the mechanical strength of the final product due to keyholing porosity. Keyholing leads to the evaporation of powder materials and the development of circular porosity throughout the component [20].

Insufficient energy input (due to decreasing laser power and high scanning speed and large layer thickness) leads to unfused powder, such as lack of fusion (Figure 1-10) and balling of CP -Ti and Ti64. Balling is a common phenomenon in SLM and affects the quality of the SLM process. Balling is generally associated with the formation of several metallic agglomerates of spherical or ellipsoidal balls due to the lack of wetting ability of the molten pool with the previous layer [16]. In contrast, some authors [21, 22] concluded that the presence of balling phenomena in aluminum alloys and iron powders is due to high energy density.

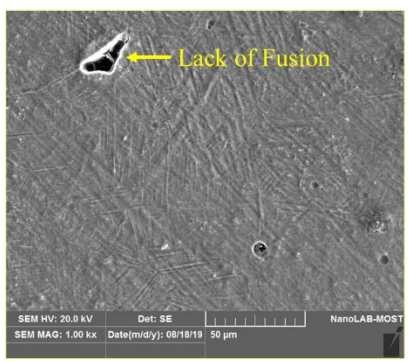


*Figure 1-10: Lack of fusion during SLM process.*

The physical basis for the energy density of the laser beam ($E_{density}$) is defined by the volumetric laser energy density with the unit Joule/Millimeter$^3$ (J/mm$^3$) and can be expressed by equation 1-1 [23].

$$E_{density} = \frac{P_{laser}}{V_{scan}\, h_{spacing}\, t_{layer}} \quad \ldots\ldots\ldots\ldots\ldots\ldots\ldots\ldots\ldots\ldots \text{Equation 1-1}$$

Where P is the laser power used in watts, v is the scan speed (mm/s), h is the hatch spacing in mm, and t is the layer thickness in mm. The energy density of the laser beam must be selected to

create a molten pool of the desired shape/size, but not so high that the molten metal vaporises at the bottom of the pool (i.e., keyholing defects) and not so low that the molten metal does not penetrate deep enough (i.e., lack of fusion and balling defects). Consequently, SLM parameters must be set to avoid balling and keyholing defects.

## 1.2 Metallic Implant Materials

Metallic alloys biomaterials (Ti alloys, CoCrMo or stainless steel) are alloys used for orthopaedic bone and joint replacements and dental implants that are intended to interact with living tissues for a long time due to their biocompatibility, high wear resistance, and strength and ductility [24]. The selection of metallic alloys is an important step in the fabrication of implants [7, 24, 25]. Due to the ever-increasing requirements for biocompatibility of hard tissues of the human body, such as bone and dental tissue, the use of Ti alloys in biomedical and dental applications is rapidly increasing. In addition, the need for excellent corrosion resistance and low modulus of elasticity in the application of bone tissue engineering, dental implants, makes this metal valuable for applications in the medical field.

### 1.2.1 Titanium Alloys

Titanium is an allotropic phase transformation metal; it can exist in two crystal structures depending on temperature. When cooled to 880°C, the beta-β phase (BCC structure) in the solid state transforms into a hexagonal close-packed (HCP) structure known as the alpha-(α) phase [26]. In titanium alloys, this temperature at which the allotropic transformation from β-phase to α-phase occurs is known as beta-transus ($\beta_{tr}$). This temperature is strongly influenced by alloying elements and impurities [24, 27].

There are three types of alloying elements for titanium (Figure 1-11), depending on how they affect phase stabilization or crystal structure: Alpha (α) stabilizing, Beta (β) stabilizing, and neutral. Alloying elements, such as Al, that are soluble in the alpha phase and increase the beta transus are called alpha (α)-stabilizing elements. Elements, such as V-Mo-Nb, that dissolve in the beta phase and decrease the beta transus are called beta (β)-stabilizing. The elements Zr and Sn can be classified as neutral since they exhibit high solubility in both the alpha and beta phases.

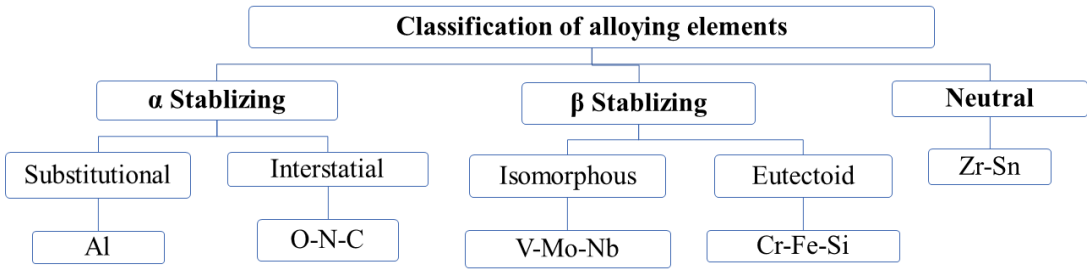


*Figure 1-11: Classification of alloying elements in titanium alloys.*

Recently, titanium alloys can be divided into four different categories based on their microstructure: Commercially pure, alpha (α) and near-alpha, alpha-beta (α+β), and beta (β) titanium alloys [28]. Table 1-1 describes a list of titanium alloys according to ASTM designations and assigned Unified Numbering System (UNS) numbers.

- Commercially pure grades or unalloyed grades of titanium alloys that have microstructures mainly based on the alpha (α)-phase. Commercially pure grades are designated by a variety of designations, including ASTM Grade 1, ASTM Grade 2, ASTM Grade 3, and ASTM Grade 4.
- Alpha (α)-titanium alloys containing an alpha (α)-phase and a small amount of β-phase (2-5% by volume), and near-alpha titanium alloys containing an alpha (α)-phase and a small amount of less than about 10% by volume of beta-phase in the microstructure.
- Alpha-beta (α+β)-alloys are an important type of titanium alloys, which include Ti64. (α+β)-alloys contain a complex composite microstructure of alpha and beta phases (in volume fractions between 10-50%), which determine their mechanical behavior [29]. The evolution of the microstructure in (α+β)-titanium alloys is determined by the cooling rate during the solidification process [30]. During cooling, the beta phase decomposes into a variety of alpha phase morphologies. Figure 1-12 shows the schematic diagram of the structure of different alpha phase morphologies during the decomposition of beta phase during cooling under beta transus temperature of Ti64 alloy [31]. At low cooling rates of less than 20 ºC/s, the beta phase transforms into allotriomorphic ($\alpha_{GB}$) and widmanstaetten ($\alpha_P$) alpha, and at cooling rates between (20-410) ºC/s, the beta phase transforms into massive ($\alpha_m$) alpha. The microstructure will be an (hcp) crystal structure and will be called alpha prime (α′) martensite due to the high cooling rates of more than 410 ºC/s inherent in the solidification process. At higher cooling rates, the beta phase in

higher concentrations of β-stabilizers alpha-beta alloys transforms into an orthorhombic structure and is called alpha double prime (α″) martensite [32].

- The microstructure of beta-titanium alloys containing a high proportion of beta-phase stabilizing elements is completely preserved in the beta phase at room temperature [33]. Beta titanium alloys are classified as stable beta, metastable beta, and beta-rich α/β alloys [34].

*Table 1-1: Titanium alloys with the ASTM designations and (UNS) numbers.*

| Unalloyed Grades | Alpha and Near-Alpha Alloys | Alpha-Beta Alloys | Beta Alloys | | | |
|---|---|---|---|---|---|---|
| | | | Stable | Metastable | Near beta | Beta-rich |
| ASTM grade 1<br>ASTM F1341 | Ti-5Al-2.5Sn<br>UNS R54520 | **Ti-6Al-4V**<br>ASTM F 1472 | Ti-30Mo | Ti-25Nb-2Mo-4Sn | Ti-20Nb-10Zr-5Ta | Ti–13Nb–13Zr<br>ASTM F1713 |
| ASTM grade 2<br>ASTM F1341 | Ti-8Al-1Mo-1V<br>UNS R54810 | Ti-6Al-6V-2Sn<br>UNS R56620 | Ti-40Mo | Ti–12Mo–6Zr–2Fe<br>ASTM F1813 | Ti-5Al-5Mo-5V-3Cr | Ti–4.5Al–3V–2Mo–2Fe |
| ASTM grade 3<br>ASTM F1341 | Ti-6Al-2Sn-4Zr-2Mo<br>UNS R54620 | Ti–6Al–7Nb<br>ASTM F1295 | Ti-35V-15Cr | Ti–15Mo<br>ASTM 2066 | Ti-11.5Mo-6Zr-4.5Sn | Ti–5Al–2Sn–2Zr–4Mo–4Cr |
| ASTM grade 4<br>ASTM F1341 | Ti-6Al-2Nb-1Ta-0.8Mo<br>UNS R56210 | Ti-6Al-2Sn-4Zr-6Mo | | Ti-13V-11Cr-3Al<br>UNS 58010 | Ti-10V-2Fe-3Al | |
| ASTM grade 7 | Ti-0.3Mo-0.8Ni | Ti-7Al-4Mo | | Ti–1Al–8V–5Fe | | |
| ASTM grade 11 | Ti-5Al-5Sn-2Zr-2Mo | Ti-8Mn<br>UNS R56080 | | Ti–8V–8Mo–2Fe–3Al<br>UNS R58820 | | |
| ASTM grade 12 | Ti-5Al-1Sn-1Zr-1V-0.8Mo | Ti-3Al-2.5V | | Ti-29Nb-13Ta-4.6Zr | | |

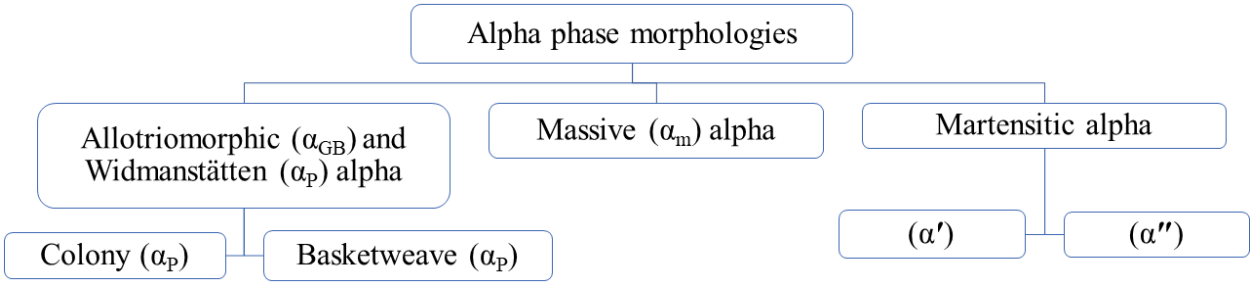


*Figure 1-12: Characteristics of the Beta → Alpha + Beta Transformation.*

Titanium is very reactive and sensitive to oxygen, nitrogen, hydrogen, and carbon when in the liquid state or heated in air to temperatures above 650°C [7]. Because of the high temperatures

and the tendency of Ti alloys to release discrete amounts of oxide into solution, it is necessary to use an inert gas atmosphere when SLMing titanium alloys to prevent embrittlement and contamination by nitrogen and oxygen. Titanium has a relatively low coefficient of thermal expansion of 8.41 ( $\mu$ m/m/°C at 20°C) and a low conductivity of 6.6 (W/m.K ). This results in a lower possibility of deformation by the SLM process compared to other common implant metals (stainless steel and CoCr alloys), as shown in Table 1-2.

*Table 1-2: Thermal properties of metallic implants.*

| Implants Metals | Thermal Conductivity W/m.K | Coefficient of thermal expansion µm/m/°C at 20°C |
|---|---|---|
| Ti64 | 6.6 [35] | 8.41[36] |
| Stainless Steel 316L | 14.4 [37] | 17.3 [38] |
| CoCrMo | 13 [39] | 13 [40] |

#### *1.2.1.1 Ti6Al4V Alloys*

Ti6Al4V (Ti64) is one of the most commonly used titanium alloys in aerospace, automotive and biomedical applications due to its high mechanical properties, excellent corrosion resistance, low ion release and excellent biocompatibility [41]. Ti64 consists primarily of a body-centered cubic β-phase and a hexagonal close-packed α-phase at room temperature. It is known that an α-β titanium alloy such as Ti64 undergoes a solid-state phase transformation. The BCC-β phase transforms into an HCP-α phase when cooled by the β-transus temperature ($\beta_{tr}$=1273 K or 995°C). The final microstructure, which determines the mechanical properties of Ti alloys produced by conventional processes such as welding and casting, is mainly influenced by the cooling rate.

## 1.3 Hydroxyapatite Bio-Ceramic

Calcium phosphate (CaP) ceramics are a group of ceramic materials containing calcium ions ($Ca^{2+}$), various phosphate ions [$PO_4^{3-}$, $PO_4$, $P_2O_7^{4-}$], and sometimes hydroxide ($OH^-$) or carbonate ions ($CO_3^{2-}$) [42]. CaP can be divided into 3 types: Hydroxyapatite (HA), Tricalcium Phosphate (TCP) and Tetracalcium Phosphate (TTCP), based on the atomic ratio of Ca/P [43]. It is well known that the atomic ratio of Ca/P is the most important factor in identifying the

bioactivity and dissolution properties of CaP. A decrease in the Ca/P atomic ratio increases the dissolution rate of CaP [44]. The atomic ratio of Ca/P in human body bones and teeth exceeds (1.67) and represents HAp [$Ca_{10}(PO_4)_6(OH)_2$] compared to the Ca/P atomic ratio of TCP (1.5) and TTCP (2) [45].

Due to the continued rising similarity and biomimetic requirements for the hard tissues of the human body, such as bone and dental tissues, the use of HA in biomedical and dental applications is rapidly increasing. In addition, the need for biocompatibility, osteoconductivity and bioactivity in biomedical applications, dental implants and oral surgery makes this ceramic valuable for medical device applications. HA is one of the main components of the hard tissues (bones and teeth) of the human body. Table 1-3 shows the biological, mechanical, and physiochemical properties of HA.

*Table 1-3: Physiochemical, mechanical and biological properties of HA* [46–48].

| Properties | Data | Properties | Data |
|---|---|---|---|
| Chemical composition | $Ca_{10}(PO_4)_6(OH)_2$ or $Ca_5(PO_4)_3(OH)$ | Hardness (HV) | 600 |
| Ca/P molar ratio | 1.67 | Decomposition Temp. (ºC) | More than 1000 |
| Crystal system | Hexagonal | Melting point (ºC) | 1614 |
| a=b<br>c | 0.942 nm<br>0.688 nm | Thermal conductivity (W/cm. K) | 0.013 |
| Young's modulus (GPa) | 80-110 | Biocompatibility | High |
| Elastic modulus (GPa) | 114 | Bioactivity | High |
| Density (g/cm$^3$) | 3.16 | Biodegradation | Low |

## 1.4 Current issues and problems of metallic implant materials

Osseointegration between metallic implants and the bone of the human body is one of the important factors affecting the application of metallic implants in the biomedical field [49–54]. Osseointegration has been associated with a variety of problems, including a large difference in elastic modulus between implants and bone, osteolysis and aseptic loosening, lack of bioactivity, and release of metal ions [55]. Osseointegration, defined as the capability of providing good

interfacial bond between bone tissue and metallic implants, is largely dependent on the implant material, implant design, surface condition, and loading conditions of the implant [50, 54].

The modulus of elasticity of a metallic implant is one of the main factors that determine its application in the biomedical field [56]. One of the most important problems to be solved for metallic implant materials is the large difference in elastic modulus between hard tissue (human bone) and the metallic implant materials [57–59]. The modulus of elasticity of titanium alloys (55-110 GPa) is lower than that of 316LSS (210 GPa) and Co-Cr alloys (240 GPa) [60]. However, the modulus of elasticity of titanium alloys is much higher than that of human bone (10-30 GPa). This large discrepancy leads to a non-gradual or irregular transfer of stresses through the human bone/tissue to the metal implant, resulting in a stress-shielding effect (Figure 1-13). The main cause of osteolysis and aseptic loosening of metal implants is the stress-shielding effect [61].

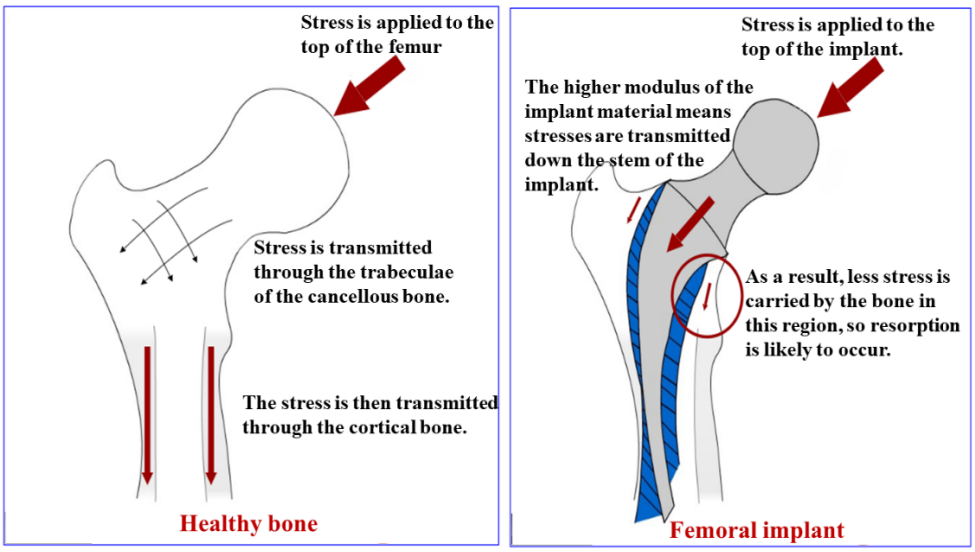


*Figure 1-13: : Healthy bone and femoral implant after applying stress* [62].

To clarify, bone in nature is a living tissue (dynamic, not static) that undergoes constant recycling, replacing old bone with new bone (resorption and replenishment), resulting in a strong bone structure with age. The resorption and replenishment process are controlled by the stress applied to the bone. Human bone tissue consists of spongy bone (porosity structure) protected by compact bone (denser structure). The density and porosity structure of the bone changes as the region in the bone changes, depending on how much stress is concentrated or acting in that region. Therefore, the strength and stiffness of the bone that carries the load applied to it are

determined by density and porosity. But in the case of the bone surrounding the implant, the large discrepancy in elastic modulus between bone and implants results in a 'stress-shielding effect' that causes the bone covering the metal implant to resorb without replenishment, leading to aseptic loosening, periprosthetic fractures, and implant migration [63–65]. The 'stress shielding effect' is observed in both orthopaedic bone and dental implants [66–68]. Therefore, in practice, there is a clear need to use a metal implant with a modulus of elasticity closer to the bone to prevent the development of the stress shielding effect.

Bandyopadhyay et al [69] investigated the effect of porosity (cell structure) on the elastic modulus of Ti-6Al-4V implants. They showed that the elastic modulus of implants with porosity in the range of (23-32) vol% is close to that of cancellous bone in humans. España et al [51] found that the elastic modulus of implant specimens with porosity in the range of 10-18 vol% of CoCrMo implants was reduced in the range of 33 to 43 GPa compared to the 248 GPa of solid implants. Similar conclusions were drawn by [59, 70–72]. In addition, the work of Bobyn et al [73] and Mullenet al [74] showed that increasing the porosity of implants to 75-80% leads to an increase in fixation strength and provides a system that allows the transfer of stress from the implant to the bone. Usually, there are different types of pore geometries (unit cells) to create a cellular structure (scaffolds), including: octahedral [75, 76], (trigonal, hexagonal, diamond-shaped) with different pore sizes [70], (cubic and rhombic) [57], and (triangular, hexagonal and rectangular) [77].

In order to enable a metallic implant to mimic the host bone as closely as possible, new functionally graded porosities are required. The functionally graded structure can be divided into gradation of porosity density and gradation of pore size [78]. Limmahakhun et al [75] in their work on SLM of CoCr with functionally graded structure stated that gradation of pore size of CoCr allows greater stress transfer to the bone surrounding the implant. Limmahakhun et al [76] also found that the octahedral columnar unit cell had the best mechanical properties and the best proliferation rate of bone cells. Han et al [79] investigated the fabrication of a functionally graded structure (porous scaffolds) of CP Ti by SLM based on a gradation of porosity density from 7.97% to 19.99%. They found that the elastic modulus was close to that of cancellous bone. No other information on the SLM of Ti alloys with functionally graded structure has been reported so far.

Another solution is to use titanium alloys with low beta (β) modulus of elasticity such as SLM with Ti13Nb13Zr cell structure [70] and SLM with Ti24Nb4Zr8Sn [17], which have low modulus of elasticity in the range of (14-69) GPa, as shown in Table 1-4. In addition, beta (β)-titanium alloys are known for their high biocompatibility [27], better mechanical properties [80], superior corrosion resistance [81], and lack of flammable or allergic reactions [60]. Interestingly, beta (β)-titanium alloys do not contain V and Al elements compared to Ti64 alloys. In the literature, vanadium is a toxic element [82] and Al causes Alzheimer's disease [83, 84].

*Table 1-4: Young's modulus of biomedical β- titanium alloys.*

| β- titanium alloys | Young's modulus (Gpa) | Ref |
|---|---|---|
| Ti-19Nb-14Zr | 14 | [85] |
| Ti–29Nb–(6-11)Ta–5Zr | 20 | [86] |
| Ti–15Nb–9Zr | 39 | [87] |
| Ti–24Nb–4Zr–7.9Sn | 42 | [88] |
| Ti–25Ta–25Nb | 55 | [89] |
| Ti–25Ta | 64 | [90] |
| Ti–12Mo–5Zr | 64 | [91] |
| Ti–13Zr–13Nb | 64-69 | [92] |

## 1.5 Selective laser melting of composite Ti – Hydroxyapatite.

New functionally graded porosities with hydroxyapatite are required to improve or enhance bone formation, accelerate bonding, and establish a good interfacial connection between bone tissue and metallic implants. Hydroxyapatite (HA) has a crystallographic and chemical composition similar to bone minerals, which could facilitate good osseointegration into bone. In addition, HA is known to be highly biocompatible, non-toxic, bioactive, non-inflammatory, osteoconductive, and non-immunogenic [47]. Despite the advantages of HA, there are also some challenges. The complexity of SLM of HA and Ti alloys is due to a number of factors, including:

- The differences in physical (thermal expansion coefficients), chemical and mechanical properties between Ti alloys and HA,
- Volume fraction and distribution of HA in the matrix of Ti alloys,
- The effects of SLM parameters.

- In addition, HA undergoes phase transformation at high temperatures during sintering and melting, which should be taken into account because HA splits into TTCP (tetracalcium phosphate) and (TCP) (tricalcium phosphate) at 1000 ºC in vacuum or 1300 ºC in air, which are unfavorable phases and can easily dissolve in the human body environment [93, 94]. Kaya et al [95] pointed out that due to heating to very high temperatures (up to 1600 °C) and rapid cooling during plasma spraying, HA may subsequently transform into some undesirable phases (such as CaO) that are incompatible with the human body. Similar conclusions were drawn by [96]. Several studies, e.g., [97], [98], and [99], focused only on improving the thermal behavior and sintering ability of HAp powder. Therefore, it is necessary to avoid phase decomposition of HAP powders at high temperatures during SLM.

Several studies have addressed the enhanced bone formation and ingrowth of natural bone into osseointegrated implants by HA coating. Santhanakrishnan et al [100] investigated the biodegradability of HA-coated Mg. They showed that the biodegradability of HA-coated Mg was improved by 180% compared to Mg alloy. Biemond et al [101] investigated and implanted the HA-coated Ti samples into the femoral condyle of goats. They concluded that there was good interfacial bonding between bone tissue and specimen after 15 weeks. Vilotijevic et al [96] studied the microstructure of plasma sprayed HA coated on SS AISI 316. They concluded that higher plasma power leads to more decomposition of HA. In addition, there are critical issues related to the coating of metallic implants with HA, which have been extensively addressed in modern research. Zhang et al [102] reported the emergence of weak Ti/HA interfacial adhesion due to the mechanical differences between HA and Ti substrates and the sharp interface. In addition, metal-coating interface failure has been identified as an important problem in coating processes that has not yet been solved [94–96].

Recently, Wei et al. [103] investigated the SLM of 316L SS and nano-HA layer by layer using microstructural studies and nanoindentation tests. They concluded that increasing the volume fraction of HA increases the extent and amount of crack and increases the hardness value. Hao et al [104] performed the same studies using 316 SS and HA powder. They performed tensile tests at different scanning speeds. They found that the scanning speed has a significant effect on the stress-strain behavior of the SLM of SS 316 and HA. The optimized scanning speed is 0.160m/s with a highest tensile strength of 95MPa.

Han et al [105] in their work on the fabrication of FGM parts from Ti-HA from 0% to 5% HA with a gradient of 1 % by weight by SLM found that the phase constituents are α Ti, $Ti_6O$, $Ti_5P_3$ and $CaTiO_3$. Han et al [106] also investigated the tensile and hardness behaviour of SLM Ti-HA with HA contents of 2% and 5% HA (wt%). They reported that with increasing HA content, the tensile strength decreases to 289 MPa and the microhardness increases from 336.2 to 600.8 HV.

There is evidence that with the development of SLM, functionally graded materials and structures (FGM/S) with porosity and chemical composition have become possible. By designing FGM/S implants with 100% Ti alloys forming the core of the implants, followed by different ratios of Ti-HA and 100% HA the surface of the implants, and the structure of the implants containing different size and density of porosity, as shown in Figure 1-14, to eliminate the mismatch of elastic modulus between bone and metal implant. As far as we know, additive manufacturing (SLM) of functionally graded materials and structures (FGM/S) of Ti alloys and HA has never been published.

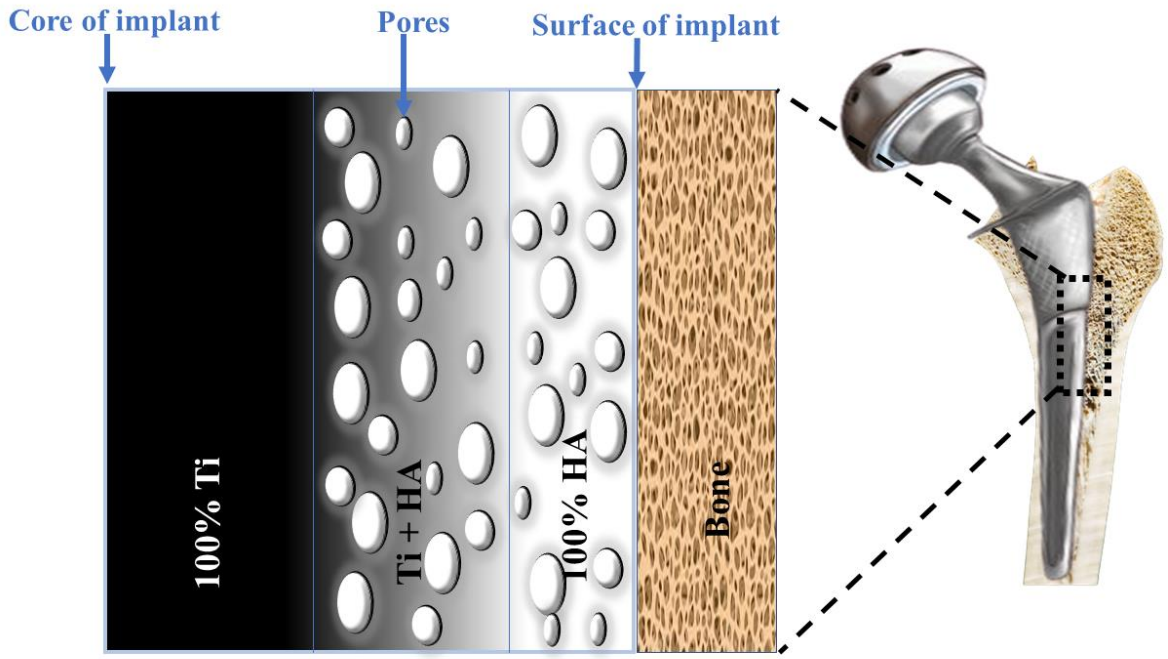


*Figure 1-14: Functionally graded materials and structures (FGM/S) implant with porosity and chemical composition.*

## 1.6 Microstructural evolution in 3D printing of Ti alloys

Microstructure evolution in 3D printing of Ti alloys is related to chemical composition and cooling rate.

### 1.6.1 Chemical composition

Figure 1-15 shows titanium alloyed with an isomorphic beta stabilizer phase diagram, which can be used as a reference to follow the phase transformation in the (α+β)-titanium alloys during additive manufacturing and welding. In this system, the beta transus and the martensite starting temperature (Ms) are decreased when the beta stabilizer content is increased. Figure 1-16 shows the phase diagram of titanium alloyed with a beta-eutectoid stabilizer. It can be used as a reference to follow phase transformations in (α+β)-titanium alloys during additive manufacturing and welding.

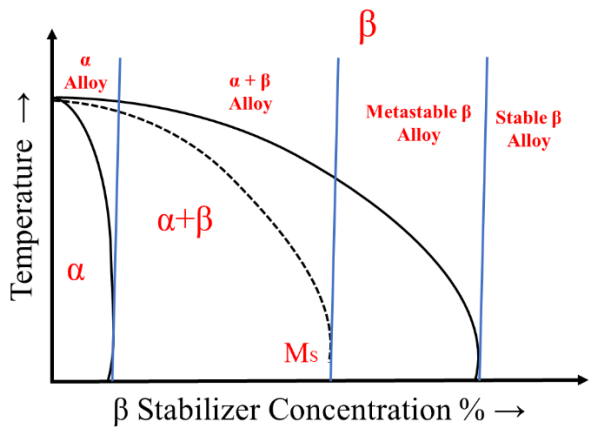


*Figure 1-15: Pseudo-binary β isomorphous phase diagram* [107].

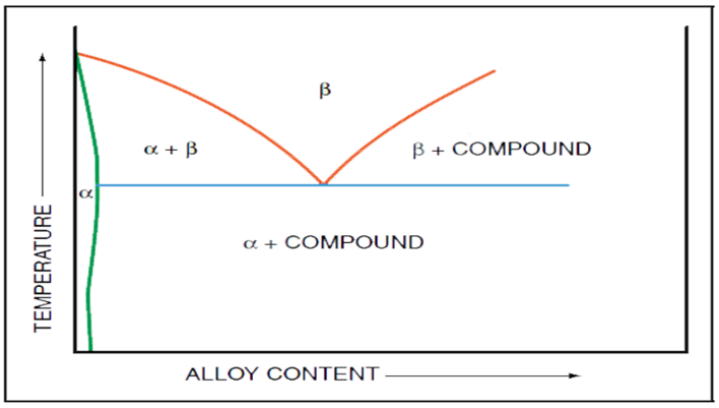


*Figure 1-16: Equilibrium phase diagram for titanium alloyed with a Beta eutectoid stabilizer* [107].

### 1.6.2 Cooling rates

Rapid heating and cooling caused by thermal gradients in additive manufacturing can significantly change the microstructure of Ti alloys. Depending on the cooling rates, the beta phase can subsequently transform into the martensite, massive, allotriomorphic and widmanstatic microstructure [31]. At cooling rates above 410 C°/s, complete martensitic transformation occurs. Massive transformation occurs between 410 and 20 C°/s. Formation of an allotriomorphic and widmanstatic microstructure occurs at lower cooling rates below 20 C°/s. Vilaro et al [108], William [1] and Song et al [109] reported that the cooling rate of SLM is in the range of 103-108 K/s. Therefore, martensite formation in SLM of titanium alloys is confirmed when the cooling rate in SLM is higher than 410 C°/s. Many authors [110–113] have demonstrated that the microstructure is fully martensitic (α′) in SLM of Ti64. Similar results have been obtained in SLM of Cp-Ti [114, 115] and Ti6Al7Nb [116]. Figure 1-17 shows the SEM micrograph showing the α′ martensite structure of the Ti64 manufactured by SLM. It has been shown that SLM parts that are fully martensitic (α′) have a low ductility of less than 10% [9, 108, 117, 118]. Some authors have tried to change the microstructure from (α′) martensite to (α+β). Vrancken et al [119] studied the effects of heat treatment on the microstructure and ductility of parts produced by SLM. Heat treatment converted (α′) to (α+β) and increased ductility from 7.36 to 12.84. Similar conclusions were found by [108, 120]. Figure 1-18 (a) and (b) demonstrates SEM micrographs showing the microstructure of annealed SLMed Ti64 at 850 and 1020 C, respectively, indicating the transformation of α′ to α+β. Xu et al [121] in their work on the SLM of Ti64 found that the microstructure was a lamellar (α+β) at an interlayer time of 1 s and a lamellar (α+β) with (α′) martensite at an interlayer time of 10 s. They also investigated the effect of layer thickness on microstructure in SLM of Ti64. Their results showed that the microstructure is a coarser lamellar (α+β) at a layer thickness of 90 µm. Therefore, the microstructure in SLM of Ti alloys strongly depends on the layer thickness in addition to the time between layers.

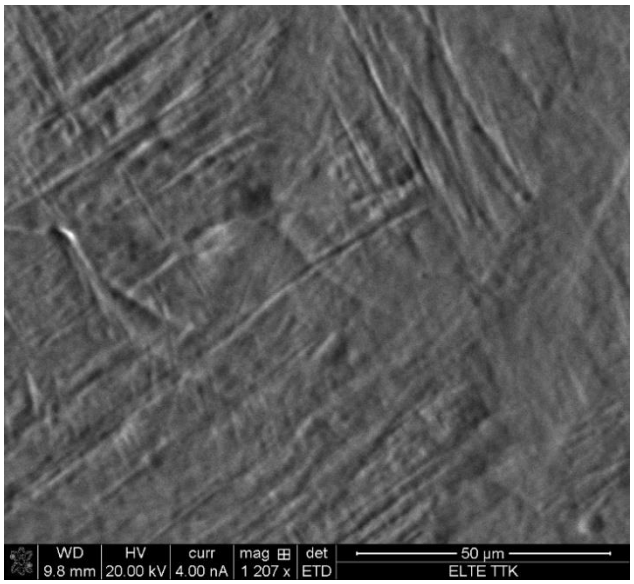


*Figure 1-17: SEM micrograph showing the α' martensite structure of the Ti64 manufactured by SLM.*

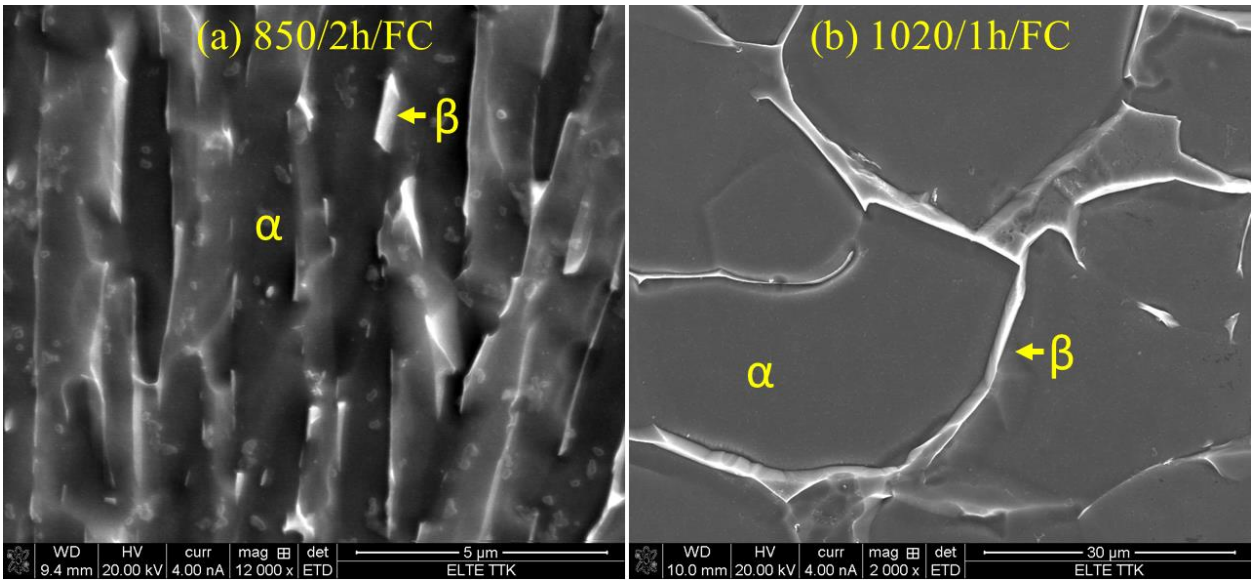


*Figure 1-18: SEM micrographs showing microstructure of annealed SLMed Ti64 at (a) 850 and (B) 1020 C, respectively, indicating the transformation of α' to α+β.*

## 1.7 Thesis Objectives

Titanium alloys, especially Ti6Al4V (Ti64), are among the most widely used materials in biomedical engineering thanks to their high biocompatibility, high specific strength, and excellent corrosion resistance. The stability and fixation of a Ti64 implant inside the bone and bone ingrowth at the interface are the greatest challenges after implantation. The resorption of

the bone is a process of bone loss resulting from the large difference in Young's modulus between the bones (10–30 GPa) and the Ti64 implants (105–110 GPa).

AM, especially SLM, is suitable for revolutionize the global parts manufacturing and logistics landscape. SLM is an important process in biomedical engineering. This is due to features of SLM technology that produce lattice (scaffolds) or complex structures and functionally graded materials (FGM). Due to the continued rising similarity and biomimetic requirements to the hard tissue of human body such as bone and dental, the use of HA in biomedical and dental applications is rapidly increasing. In addition, the need for biocompatibility, osteoconductivity, and bioactivity in the biomedical application, tooth implants, and maxillofacial surgery, make this ceramic valuable for applications in the medical engineering. The development of functionally graded materials/structures of Ti64 and HA for applications in biomedical field is to improve the osseointegration between metallic implants and hard tissue of human body has become possible with the development of SLM. The complexity and challenges of the SLM of HA and Ti64 alloys comes from a number of factors including:

- The different in physical (thermal expansion coefficients), chemical and mechanical properties between Ti64 alloys and HA,
- Volume fraction and distribution of HA in Ti64 alloys matrix,
- The effects SLM parameters.
- In addition, the HA is subject to phase transformation at high temperatures during melting should be considered

Another main problem in the literature on SLM of Ti64 for biomedical implants is that the formation of an α′-martensitic microstructure. It has been experimentally demonstrated that SLM parts that are fully α′ martensitic have low ductility of less than 10%. Furthermore, one of the main barriers to the use of spherical titanium powder in SLM is that it is often very expensive (200–450 $/kg). Irregularly shaped hydride dehydride (HDH) powder is a less expensive product than spherical titanium powder (66–176 $/kg).

By presenting the problems and challenges above, the specific objectives of this study are summarized below:

- Investigate the effects of annealing and solution treatment at 850 and 1020 ºC below and above the β-transus temperature on the microstructure and mechanical properties of Ti64 structure fabricated by SLM to improve ductility.
- Analyze the phases, microstructure, and mechanical properties of Ti64-2%HA composite samples fabricated by SLM.

  The Ti64 powder was mixed with different weight ratios of HA, including 1, 2, 3, 4, and 5 wt%. It was decided that the best ratio for this study was 2 wt% of HA (optimum addition). The Ti64 - HA composites, especially with high amounts of HA (3 to 5 wt%), showed complicated production behavior; during SLM processing, several explosions (popups) occurred, causing the support structure to crash.
- Propose, describe, explain, and analyze a functional implant of functionally graded materials and structures (FGM/S) with porosity and chemical composition of Ti and HA by SLM process, which ensures good biological fixation and osseointegration between implant and bone tissue without using bone cements.
- Determine whether the hybrid powder of Ti64 (50 wt% plasma atomized (PA) spherical and 50 wt% hydride dehydride (HDH) irregular shaped powder) can be printed without affecting the microstructural and mechanical properties of the components fabricated by SLM system to reduce the cost.

  This ratio 50/50 was chosen to reduce the cost as much as possible and also because of the limited amount of powder, which did not allow me to use other ratios.

# 2 Heat Treatments of SLM Ti6Al4V

## 2.1 Introduction

SLM involves a complex interaction between the phenomena of the process (including melting and solidification) and microstructural changes or phase transformations of the material being manufactured [7]. The heating and cooling rates of the SLM technique are much higher than those of casting and welding processes and can significantly change the microstructure of Ti64 alloys [122]. The main causes for the complete transformation of the (β)-phase into a martensitic (α′)-structure during the SLM process are the complete melting mechanism and the very high cooling rate [11]. Martensitic (α′) is a supersaturated substitutional solid solution of elements (vanadium) in a hexagonal crystal system of the (α) phase [123].

One of the main issues in the literature about SLM of Ti64 for biomedical implants is the formation of an α′-martensitic microstructure [11, 112]. It has been experimentally demonstrated that SLM parts that are fully α′ martensitic have low ductility of less than 10% [9, 108, 117, 118, 124, 125]. Moreover, the residual stresses are associated with the formation of an (α′) martensitic structure, resulting in lower mechanical performance [126]. Due to the highly localized heat input, short interaction times, rapid solidification, and large thermal gradients during the SLM process, thermal stresses are formed. It is well known that the fatigue performance of SLM parts can be affected by residual stresses generated by the high cooling rates and thermal gradient of the SLM process [127]. In addition, according to ASTM F13-12a [128] and ASTM F2924-14 [129], the microstructure of an implant or SLM part requires a minimum strain of 10% and an alpha (α)-beta (β) dual phase.

In [111, 121, 130–132], the authors changed the microstructure of the SLM part from (α′) to (α+β) to improve ductility and reduce internal residual stresses. The work by Xu et al [121] revealed that the microstructure of 90 μm layer thickness is an (α+β) structure compared to the microstructure of 30 μm layer thickness is an (α′) martensitic structure. Ali et al [130] presented a new principle of (α′)-martensite decomposition, in which increasing the bed temperature (preheating) to 570 °C enables the decomposition of (α′) into (α+β)-structure. As indicated by Qiu et al [111], (α′) transforms into (α) plus (β) during heat treatment by hot isostatic pressing (HIP). Vrancken et al [131] in their work on the addition of 10 wt% Mo to Ti64 powder during SLM process found that the conversion of (β) to (α′) is completely suppressed due to the

reduction of **β**-transus temperature from 995ºC to 900ºC. Muhammad et al [132] investigated the heat treatments of Ti64 parts produced by SLM at 950ºC near the β-transus temperature for 1h, followed by furnace and air cooling. They found that the Ti64 microstructure has almost the same microstructure (α) plus (β) due to the converging cooling rate.

## 2.2 Objective

Consequently, there is clearly a practical need to study the microstructure evolution and mechanical performance of heat treatment of SLM parts. The heat treatments of Ti64 parts produced by SLM have not been studied in depth. Therefore, the purpose of this research is to analyze the effects of annealing and solution treatments at 850 and 1020 ºC below and above the β-transus temperature ($\beta_{tr}$) on the microstructure and mechanical properties of Ti64 microstructure manufactured by SLM. After the solution treatment, the specimens were aged (reheated) to 550 ºC for 3 hours.

## 2.3 Microstructure of Ti6Al4V

Phase transformations in Ti64 alloy can be divided into two types depending on the cooling rate: diffusive processes (nucleation and growth) and martensitic transformation (shear mechanism). Due to the fast-cooling rates of more than 410 °C $s^{-1}$, the β-phase transforms into the (hcp) crystal structure called alpha prime (α′) martensite β→ α′ or into the orthorhombic structure called alpha double prime (α′′) martensite β→ α′′. During the diffusive transformation, the Ti64 alloy undergoes a phase transformation in the solid state. The BCC-β phase transforms into the HCP-α and BCC-β phases at slow cooling rates of less than 20 °C $s^{-1}$ through the β-transus temperature ($\beta_{tr}$), as shown in Figure 2-1. For this study, the $\beta_{tr}$ temperature was calculated to be 975 °C according to Eq. 2-1 [133].

$$\beta tr = 882 + 21.1\,[Al] + 4.2\,[Sn] + 123\,[O] + 23.3\,[Si] - 9.5\,[Mo] - 6.9\,[Zr] - 11.8\,[V] - 12.1\,[Cr] - 15.4\,[Fe] \quad \text{Equation 2-1.}$$

$$\beta tr = 882 + 21.1\,[6.11] + 4.2\,[0] + 123\,[0.090] + 23.3\,[0] - 9.5\,[0] - 6.9\,[0] - 11.8\,[4.02] - 12.1\,[0] - 15.4\,[0.17]$$

$$\beta tr = 882 + 128.93 + 0 + 11.7 + 0 - 0 - 0 - 47.44 - 0 - 2.62 = 973 \sim 975\ °C$$

Depending on the $\beta_{tr}$ temperature, the heat treatment of Ti64 can be divided into the following zones: Subtransus heating (in the α+β zone) and Supertransus heating (in the β zone), as shown in Figure 2-1.

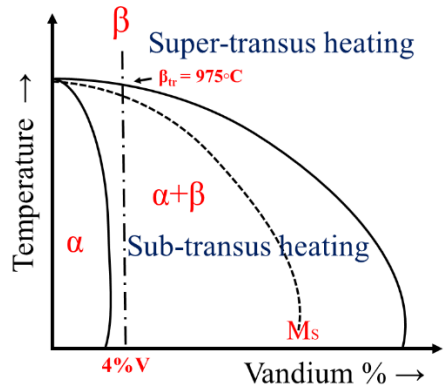


*Figure 2-1: Typical Equilibrium Phase diagram for Ti64 alloys.*

## 2.4 Materials and Methods

### 2.4.1 Materials preparation

The SLM Ti64 components are manufactured at Dent-Art-Technik Kft (Győr, Hungary) using a commercial SLM machine (Sisma mysint 100/Italy) equipped with a 200 W fiber laser and a 55 µm laser spot. In this study, Ti64 plasma-atomized spherical powder (Gr.23) supplied by (LPW Technology/UK), as shown in Figure 2-2, was used as the base material. Table 2-1 reports the chemical composition of Ti64 powder. The size distribution is in the range of 15-45 µm (D10:14.28 µm- D50:25.06 µm-D90:42.15 µm). SLM parameters were selected based on the guidelines available in the SLM machine, resulting in optimal build conditions. Throughout the process, the layer thickness, scan speed, and laser power were kept constant at 20 µm, 1000 mm/s, and 125 W, respectively. For shielding, Pure argon gas was used with a flow rate of 35 L/min. The dimensions of the specimens and the configuration of the tensile test performed during the investigation are shown in Figure 2-3.

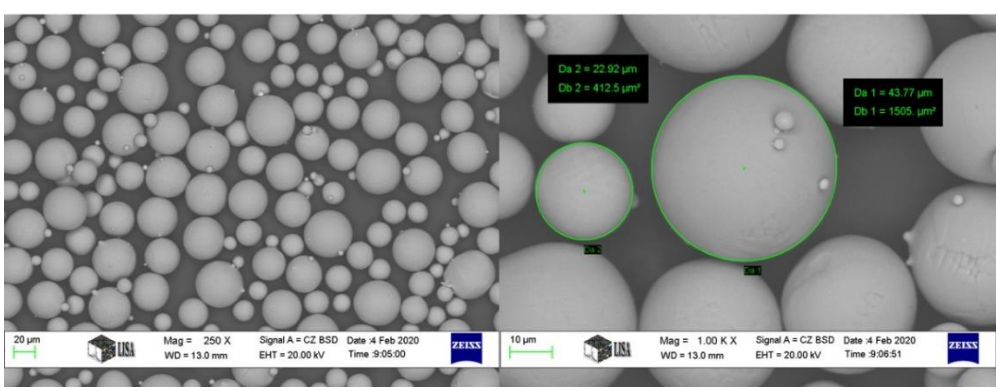


*Figure 2-2:SEM micrographs show morphology of Ti64 powder at different magnifications (250x and 1000x).*

*Table 2-1: Chemical composition of Ti64 powder and ASTM specification.*

| (Mass%) | | Al | V | Fe | O | N | C | H | Ti |
|---|---|---|---|---|---|---|---|---|---|
| Ti64 powder | | 6.11 | 4.02 | 0.17 | 0.090 | 0.023 | 0.01 | 0.003 | Bal |
| ASTM B348 Gr.23 | Max | 6.50 | 4.50 | 0.25 | 0.13 | 0.03 | 0.08 | 0.0125 | Bal |
| | Min | 5.50 | 3.50 | - | - | - | - | - | - |

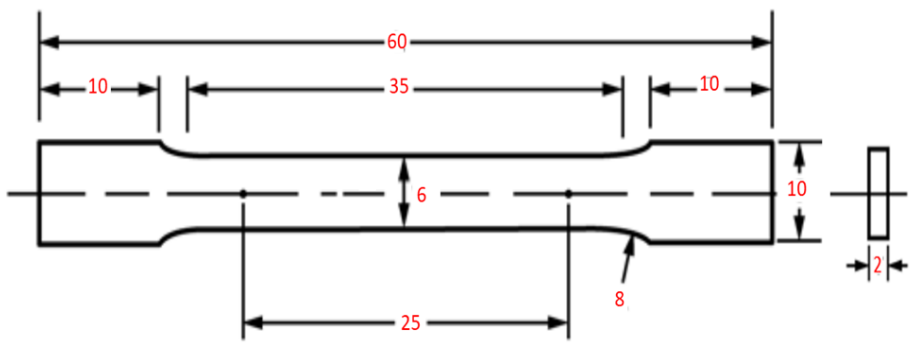


*Figure 2-3: The shape and size of the tensile specimen (mm).*

### 2.4.2 Heat treatments processes

After fabrication, four different heat treatments were performed, as shown schematically in Figure 2-4. In heat treatments 1 and 2, the SLM Ti64 specimens were heated to 850 ℃ (α 73%+β27%) for 2 hours and then some specimens cooled in the furnace (FC) and others quenched with water (WC) to room temperature. In heat treatments 3 and 4, the SLM Ti64 specimens were heated at 1020℃ (β100%) for 1 h, some specimens followed by FC and others followed by WC. After WC, the specimens were aged at 550 ℃ for 3 hours and then cooled in the furnace. For shielding, Pure argon gas was used with a flow rate of 35L/min. HT850FC, HT850WC, HT850WC+ AG, HT1020FC, HT1020WC, and HT1020WC+ AG were the designations for the corresponding heat-treated specimens at different temperatures.

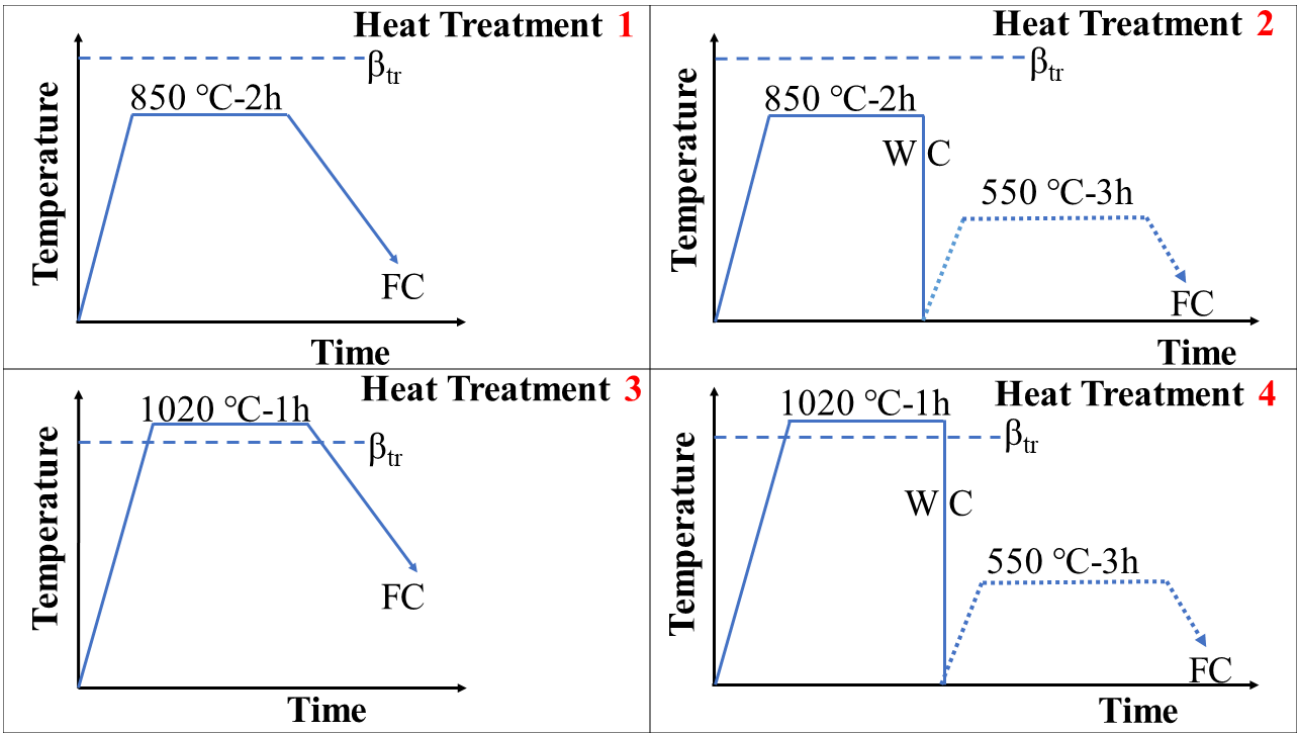


*Figure 2-4: Schematic representation of heat treatment cycle used in this work.*

### 2.4.3 Materials characterization

To understand how the microstructures affect the mechanical properties, three tensile test specimens were performed at room temperature for each treatment. The tensile test was performed using a non-computerized testing machine (FORM + TEST, Model: TTM 100, Germany) at a crosshead speed of 1 mm/min. All metallographic examinations of the specimens were prepared according to the standard procedure for titanium alloy metallography. Optical microscopy (OM, Neophot 2, Germany) and FEI Quanta 3D scanning electron microscope (SEM, Hitachi, Japan) equipped with an energy dispersive X-ray spectrometer (EDS) were used to study the microstructure of the specimens. A (EDS) was used to evaluate the chemical composition of the phases. Keller's etchant No. 193 [134] was used to visualize the microstructure of the specimens. X-ray diffraction analysis (XRD, PhilipsX'-PertPro) with CuKα radiation was performed to analyze the phases composing all the specimens. The tube current and tube voltage of the XRD are 20mA and 40kV, respectively. Vickers microhardness testing was performed with a dwell time of 10 seconds and a load of 0.5 kg f.

## 2.5 Results and Discussion

### 2.5.1 Microstructure investigation

The final microstructure, which determines the mechanical properties of the as-manufactured Ti64 alloy, is determined by the heat treatment parameters, mainly the cooling rate, time, and temperature. The research objectives in this study focused on heating the specimens to 850 ℃ and 1020 ℃ followed by furnace cooling (FC) and water quenching (WQ) to understand the effects of different heat treatment temperatures and cooling rates on the resulting microstructure and mechanical properties.

#### *2.5.1.1 Microstructure of as-manufactured Ti6Al4V*

Figure 2-5 reports the XRD pattern of the as-manufactured specimens, in which hexagonal close-packed reflections related to the α′ martensite or α phase and a weak orthorhombic reflection related to the α″ martensite of titanium were observed. The α″ structure is indicated at the reflection plane of (111) according to Ref [135]. Moreover, a new reflection plane (101) is seen at 2Θ=36.53°. Unfortunately, there is no possible explanation for this result. It would seem that this new reflection is related to the α″ structure.

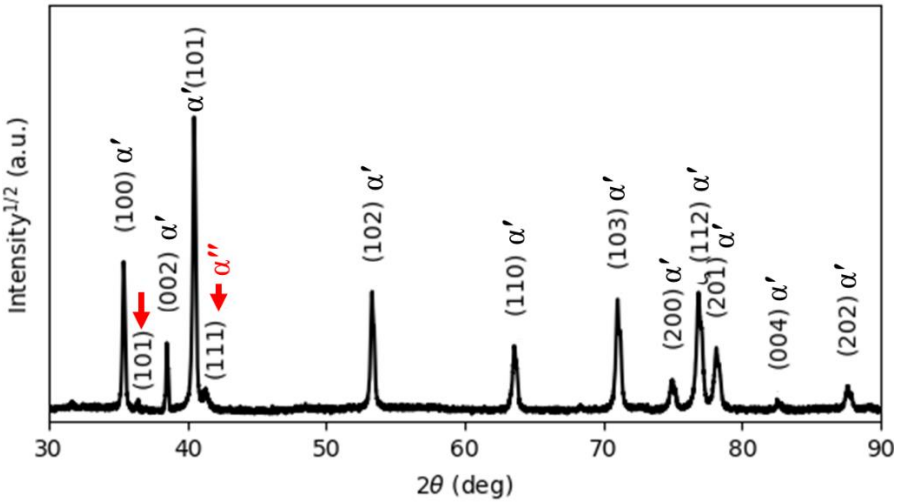


*Figure 2-5: The XRD pattern of the as printed Ti64 indexing α′ and α″ phases.*

It is well known that both of α and α′ have a hexagonal structure. Therefore, it is very difficult for XRD analysis to distinguish them from each other. However, there is an important metallurgical difference between α′ and α phases, which is correlated to the content of V in the atomic structure. Due to the fast-cooling rates, vanadium diffusion is inhibited; therefore, the

vanadium content in α′ phase is higher than in α phase, leading to the development of significant deformations of the crystal structure of the α′ phase, which causes broadening of the XRD peaks. Full width at half maximum (FWHM) values were measured for the peaks around 2Θ= 40.56° and 39.80°, which correspond to the diffraction of the (101) and (110) peaks of the α and β phases, respectively. Table 2-2 compares and summarizes the changes in the FWHM and lattice parameters of the phases in the as-manufactured state and after different heat treatments. It can be seen from Table 2-2 that the FWHM value of the as-manufactured specimens (0.1466) is significantly higher than that of the other heat-treated specimens because the as-manufactured specimen is mainly composed of α′ martensite. Moreover, the lattice parameters a and c of the as-manufactured specimens are 2.9324Å and 4.6716Å, respectively, which is in line with the lattice parameters for the α′ martensite in Ref [136].

*Table 2-2: Lattice parameters and FWHM of the main α/α′ and β peaks at 2θ=40.56° and 39.80° respectively of as printed sample and samples subjected to different heat treatments.*

| | α/α′ Phase | | | | | β Phase | | |
|---|---|---|---|---|---|---|---|---|
| | Lattice parameters (Å) | | | (101) | | Lattice parameters (Å) | (110) | |
| Sample Name | a | c | c/a | 2Θ° | FWHM | a | 2Θ° | FWHM |
| As printed | 2.9324 | 4.6716 | 1.5930 | 40.56 | 0.1466 | - | - | - |
| HT850FC | 2.9218 | 4.6667 | 1.5972 | 40.54 | 0.0876 | 3.1989 | 39.80 | 0.253 |
| HT850WC | 2.9236 | 4.6701 | 1.5973 | 40.51 | 0.094 | 3.2419 | 39.25 | 0.27 |
| HT850WC+AG | 2.9228 | 4.6692 | 1.5975 | 40.52 | 0.0792 | 3.2001 | 39.80 | 0.211 |
| HT1020FC | 2.9264 | 4.6819 | 1.5956 | 40.46 | 0.1008 | 3.2316 | 39.41 | 0.366 |
| HT1020WC | 2.9295 | 4.6699 | 1.5968 | 40.43 | 0.114 | - | - | - |
| HT1020WC+AG | 2.9238 | 4.6714 | 1.5977 | 40.47 | 0.1373 | 3.1973 | 39.80 | 0.243 |

No amounts of β phase were revealed by XRD analysis. In contrast, EBSD phase maps (Figure 2-6) of the cross section indicate the formation of a body centered β phase. The EBSD phase maps highlighted that the volume fraction of β is about 8.5% of the Ti64 structure formed by SLM. The α′ phase and β phase are colored red and green, respectively, in the EBSD maps. It is shown that the prior β is formed by epitaxial growth during successive layer depositions [11].

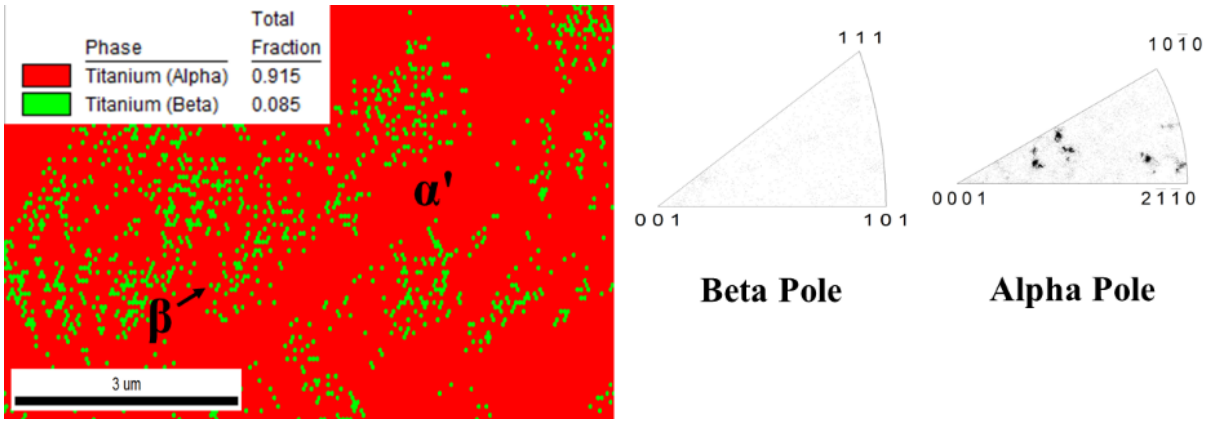


*Figure 2-6:EBSD phase maps of as printed Ti64 sample indicating the volume fraction of α′ and β phases.*

As was hypothesized, the SEM experiments (Figure 2-7) prove that the microstructure of the as-fabricated Ti64 specimens is full α′ martensitic, with a lath morphology and a small amount of β phase. The average value for α′ lath thickness was 0.420 µm. Figure 2-8 shows the EBSD orientation maps and grain size of the α′ martensite microstructure in detail. Moreover, this martensitic microstructure is defined as a hierarchical structure (Figure 2-9), which is composed of four different types of α′ on the basis of the dimensions: primary (L=125 µm), secondary (64 µm), tertiary (32 µm), and quartic (8 µm). The formation of α′ martensite depends on the cooling rate. According to Ref [31], the critical cooling rate of Ti64 for the formation of α′ martensite in the microstructure is 410°C $s^{-1}$. The cooling rate during SLM of Ti64 is $10^4$ K $s^{-1}$ [108], which is significantly higher than 410°C $s^{-1}$. Therefore, the formation of α′ martensite during SLM of Ti64 is not surprising. The average hardness of the α′ is 377 HV (Figure 2-10). It is important to note that the hardness of α′ martensite has the highest value among the microstructures of the other specimens, except for HT1020WC and HT1020WC+AG.

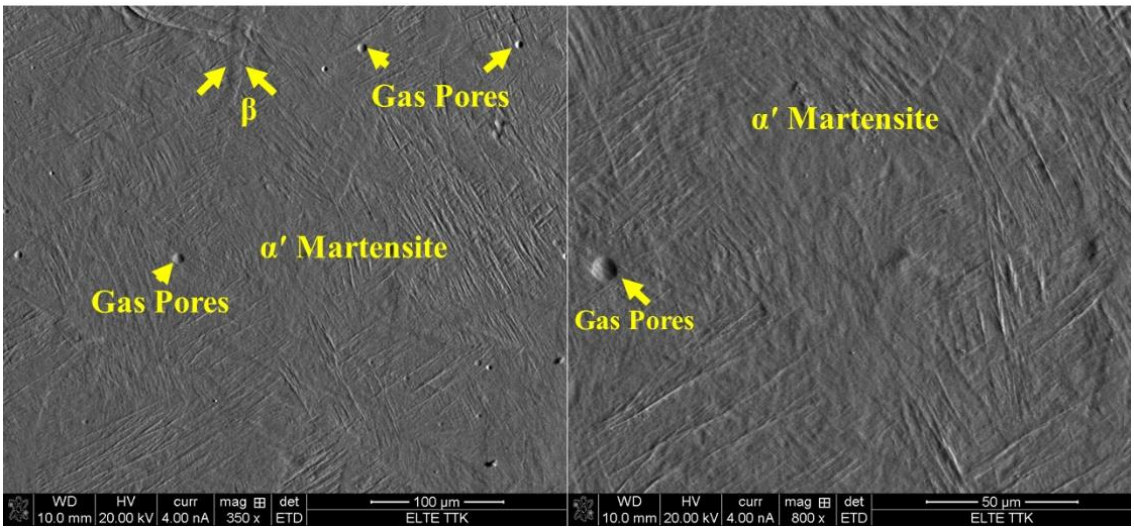


*Figure 2-7:SEM images of Ti64 produced by SLM showing α′ martensite microstructure and the formation of gas pores.*

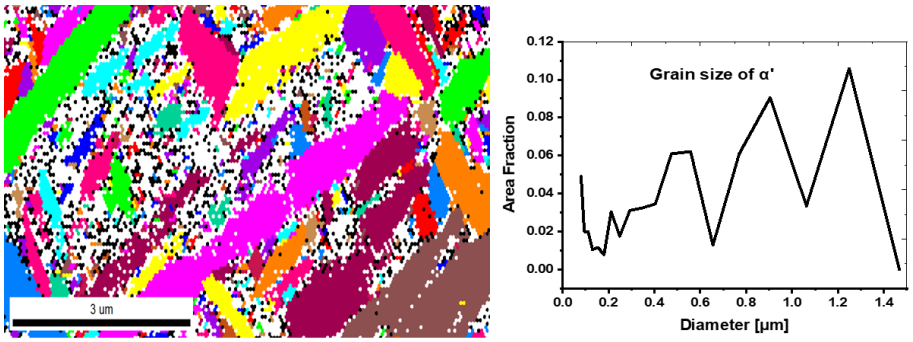


*Figure 2-8: EBSD phase maps and grain size of the α′ martensite microstructure.*

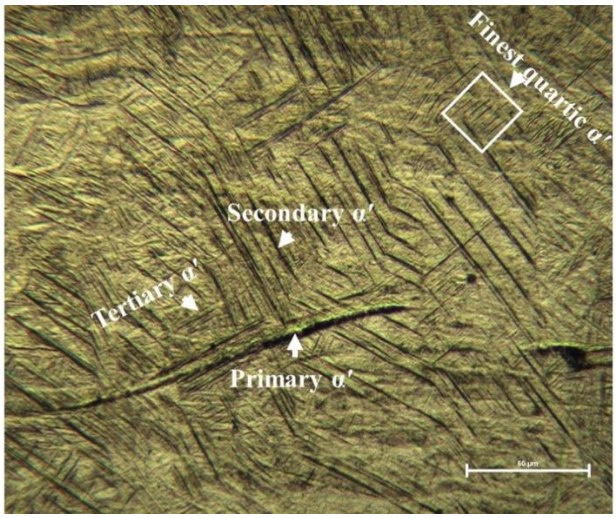


*Figure 2-9: An optical micrograph showing hierarchical structure of α′ martensitic microstructure.*

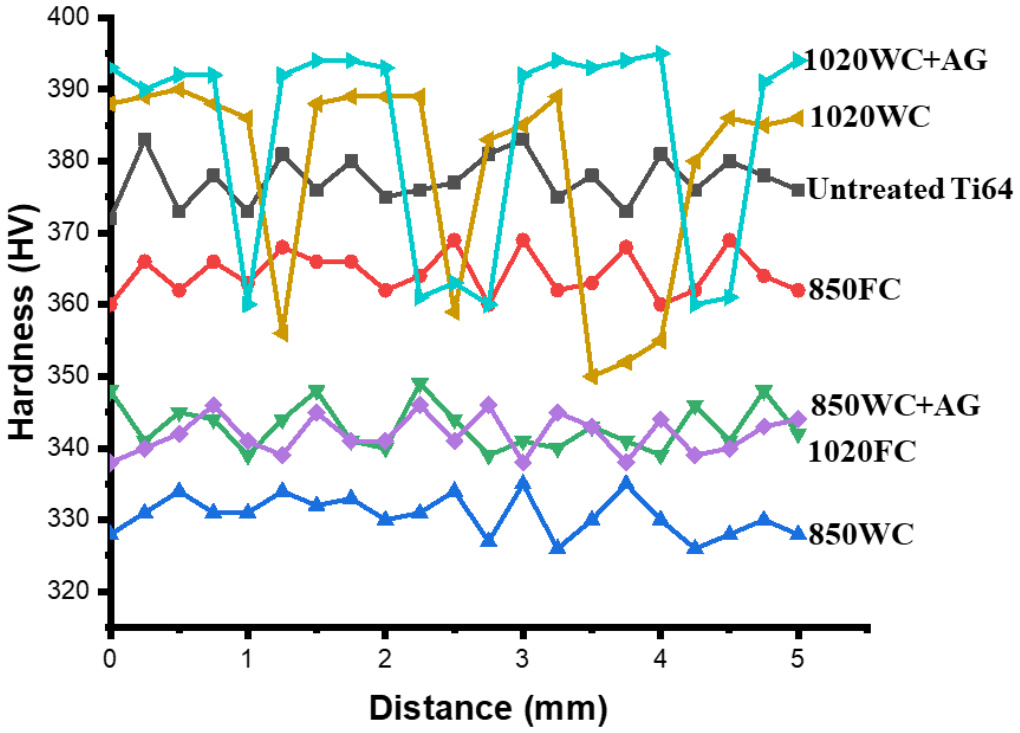


*Figure 2-10: Typical hardness profile of as printed sample and samples subjected to different heat treatments.*

Figure 2-11 a and b show the microstructure of as-manufactured Ti64 at low magnification by optical microscope for the top and side views, respectively. The microstructures do not exhibit homogeneous morphologies. In the top view, equiaxed β-grains with an average diameter of 72 µm were observed to be completely interspersed with α′ martensite (Figure 2-11 a), which can be attributed to recrystallization during the SLM process. This is completely different from what was identified in the side view (Figure 2-11 b). The morphology in the side view consists of β columnar grains that grow epitaxially due to the re-melting and re-solidification of the material during the successive layer depositions. The width of the β columnar grains is around 78 µm, which corresponds to the hatch spacing chosen for the fabrication of the specimens. Figure 2-7 shows a typical SEM micrograph of Ti64 produced by SLM, indicating the existence of spherical gas pores (7.5 µm) in the microstructure. Gas pores are formed by the formation of a void in the solidified pool due to trapped gas, which is not insoluble in liquid metals, resulting in a spherical void shape [122]. There are two sources of trapped gas: gas from the powder manufacturing process and inert shielding gas used with SLM.

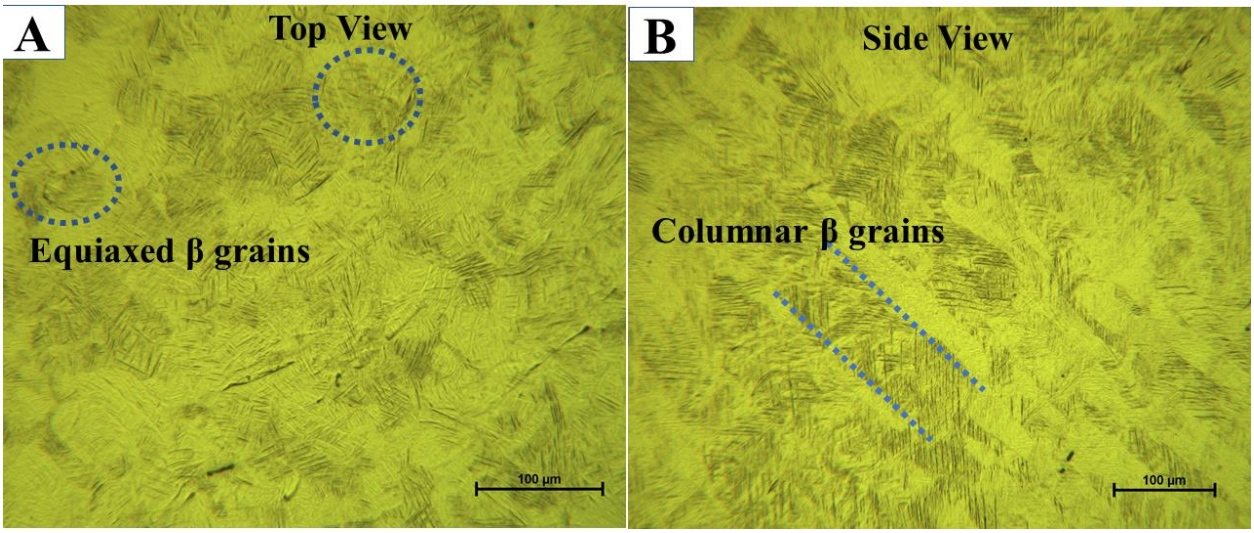


*Figure 2-11: a: An optical micrograph of the top view of as printed Ti64 indicating equiaxed β grains morphologies fully with α′ martensite. b: An optical micrograph of the side view of as printed Ti64 indicating β columnar grains.*

#### *2.5.1.2 Microstructure of subtransus heat treatments*

Figure 2-12 reports the X-ray diffraction pattern of the HT850FC specimen in which reflections of the α, β, and α″ phases were observed. The β phase can be seen in the four reflection planes (110), (200), (211), and (220). It is interesting to note that the α″ structure is displayed at a new weak reflection plane of (110)(2Θ=34.73°) according to Ref [136, 137]. This would appear to indicate that the α″ is a new phase precipitated from the α′ phase during FC cooling. The reflection plane (101) at 2Θ=36.53° remains visible in the XRD pattern of the specimen after HT850FC. Figure 2-13 presents the microstructure of the HT850FC specimen at various magnifications, indicating α phase (dark phase) associated with β phase (lighter phase), confirmed by EDS analysis as a V-rich element (Figure 2-13 D). The V content of the β phase (2.76 Wt%) is slightly higher than that of the α phase (2.18 Wt%). This β phase, which is poor in vanadium, is called metastable βr phase. Back scattered electron mode (BSE, Figure 2-14) confirmed the slight chemical contrast between the α and β phases. It is interesting to note that the Al content in the βr phase (7.67 Wt%) is higher than that of the α phase (6.27 Wt%). The hardness values of the HT850 FC averaged at 364 HV, is lower than the hardness of the as-manufactured specimen (377 HV). This is due to the decomposition of α′ martensite into α, β, and α″ phases.

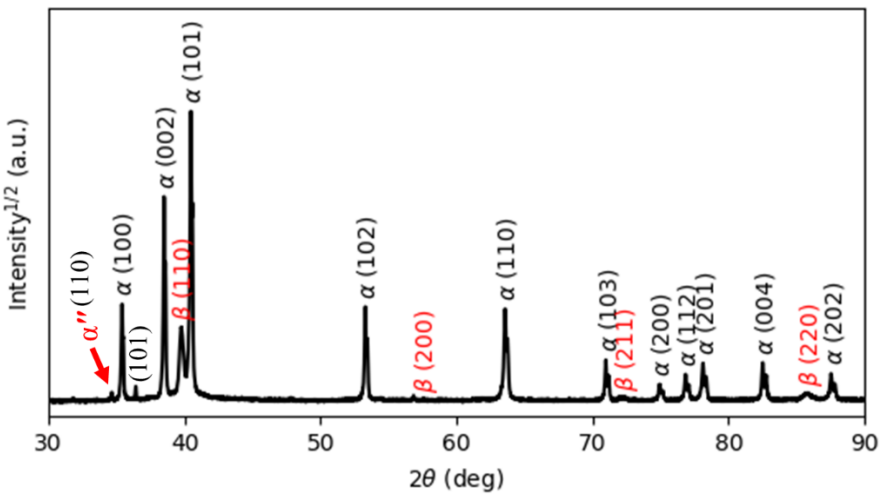


*Figure 2-12: The XRD pattern of the HT850FC sample indexing α, β, and α" phases.*

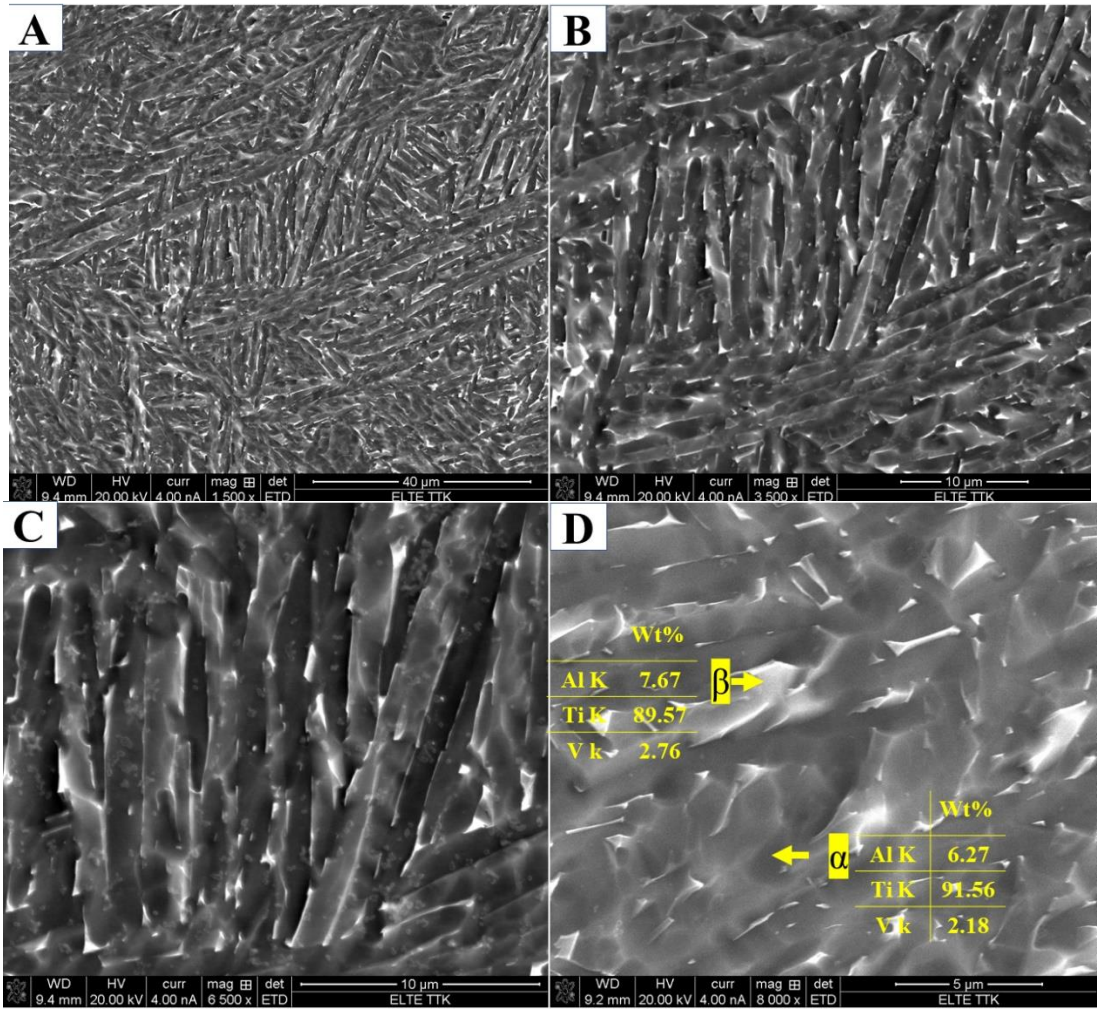


*Figure 2-13:SEM micrographs showing microstructure of the HT850FC sample at different magnifications indicating α phase (dark phase) coupled with β phase (lighter phase).*

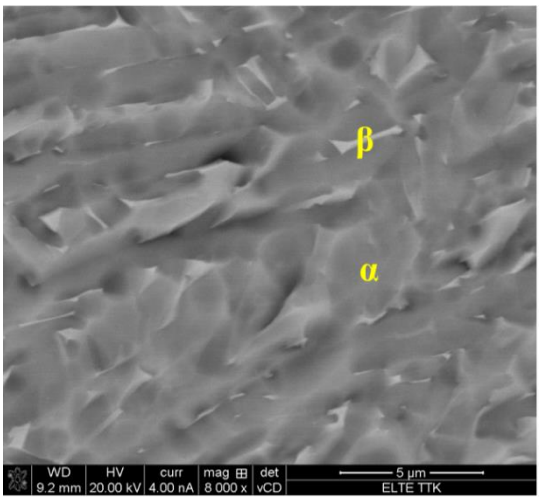


*Figure 2-14: SEM (BSE) micrograph showing microstructure of the HT850FC sample indicating the slight chemical contrast between the α and β phases.*

It has been shown that the α phase begins to transform into the β phase when heated to a temperature above 705 °C [138]. The formation of the β phase at elevated temperature can be attributed to the expulsion of vanadium atoms from the α′ phase, leading to the nucleation of the α-phase along the α′ boundaries and the precipitation of the β phase in the grain boundaries of the α phase [112]. As highlighted in Table 2-2, the angle of the XRD peak (101) in the heat-treated specimens is shifted to lower diffraction angles, compared to the as-manufactured specimen, suggesting that there is significant diffusion of vanadium in the Ti structure. The loss of interstitial or substitutional atoms (V or Al) in the hcp lattice of Ti leads to a slight increase in the c/a ratio of the α phase. All heat-treated specimens exhibited an increase in the c/a ratio of the XRD peak (101) compared to the as-manufactured specimen. From these results, it can be inferred that more vanadium was dissolved in the β phase during the heat treatments.

In this region, at temperatures of 850 °C, below the $\beta_{tr}$, the α′ microstructure transforms to about 73% α and 27% β upon heating [139]. Cooling to room temperature reveals a lamellar mixed structure of α plus β, in which the α phase is appear as fine needles. Figure 2-15 shows the microstructure of the HT850FC specimen at a higher magnification. It can be seen that some nanoscale particles are dispersed on the α phase. It was found that these nanoscale particles are the β phase [132].

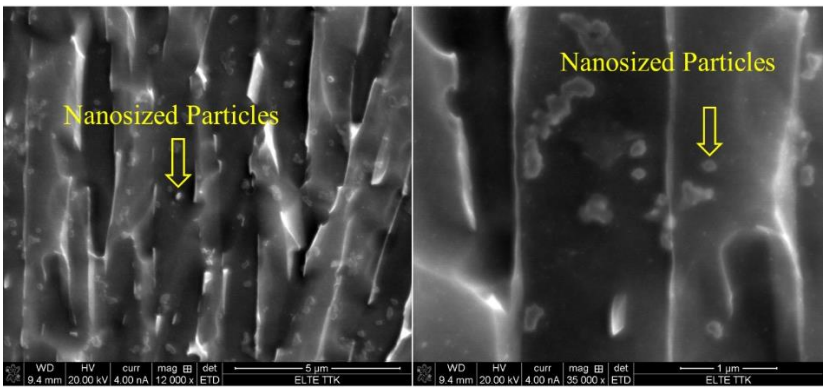


*Figure 2-15: SEM micrographs at higher magnifications showing microstructure of the HT850FC sample indicating the formation of β nanosized particles dispersed on the α phase.*

The XRD analysis of the HT850WC specimen is illustrated in Figure 2-16. It can be identified that the HT850WC specimen has strong reflection peaks of the α phase. There are two reflection peaks of the β phase at (110) and (200). In addition, one reflection peak (111) of the α″ phase was identified. The reflection plane (101) at 2Θ=36.53° remains visible in the XRD pattern of the specimen after HT850WC. The fullwidth half maximum (FWHM) of the HT850WC specimen (Table 2-2) confirms that this specimen has narrower α reflections (0.094) compared to HT1020FC (0.1008) and is broader than that of the HT850FC specimen (0.0876). These results show that the HT850WC produces an orthorhombic α″ instead of α′.

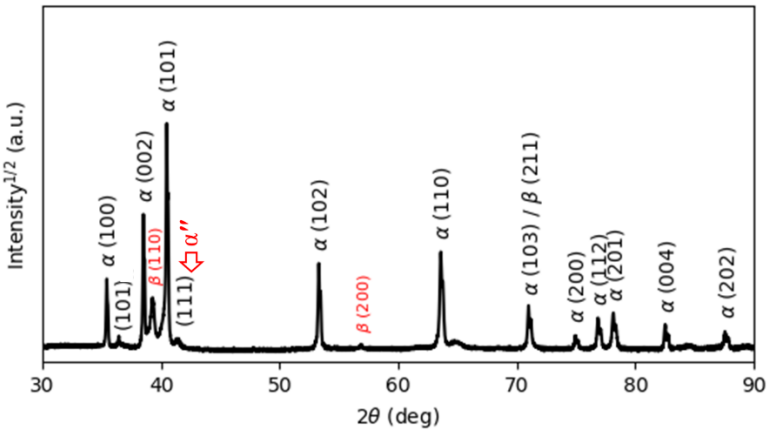


*Figure 2-16: The XRD pattern of the HT850WC sample indexing α, β, and α″ phases.*

Figure 2-17 (a to d) presents the SEM micrographs of the microstructure of the HT850WC specimen at various magnifications. The EDS-spot analysis of these formed phases is presented in Figure 2-17 (c). The average V content of the β and α phases was found to be 2.28 and 1.64

Wt%, respectively, which is confirmed by the backscattered electron (BSE) mode as a significant chemical contrast (Figure 2-18). As can be seen, this β phase is not very rich in V, indicating the formed metastable βr phase. In fact, the very high cooling rate in water, which prevents the diffusion of vanadium that has not reached the equilibrium state, can explain the formation of α″ martensite. It has been shown that the formation of α″ martensite depends on the V content [108]. Figure 2-19 is the EDS line scan across the microstructure of the HT850WC specimen. From the analysis of the composition profile, it can be deduced that some areas are rich in V and others are poor in V. The presence of high and low amounts of V can explain the formation of α″ and βr phases.

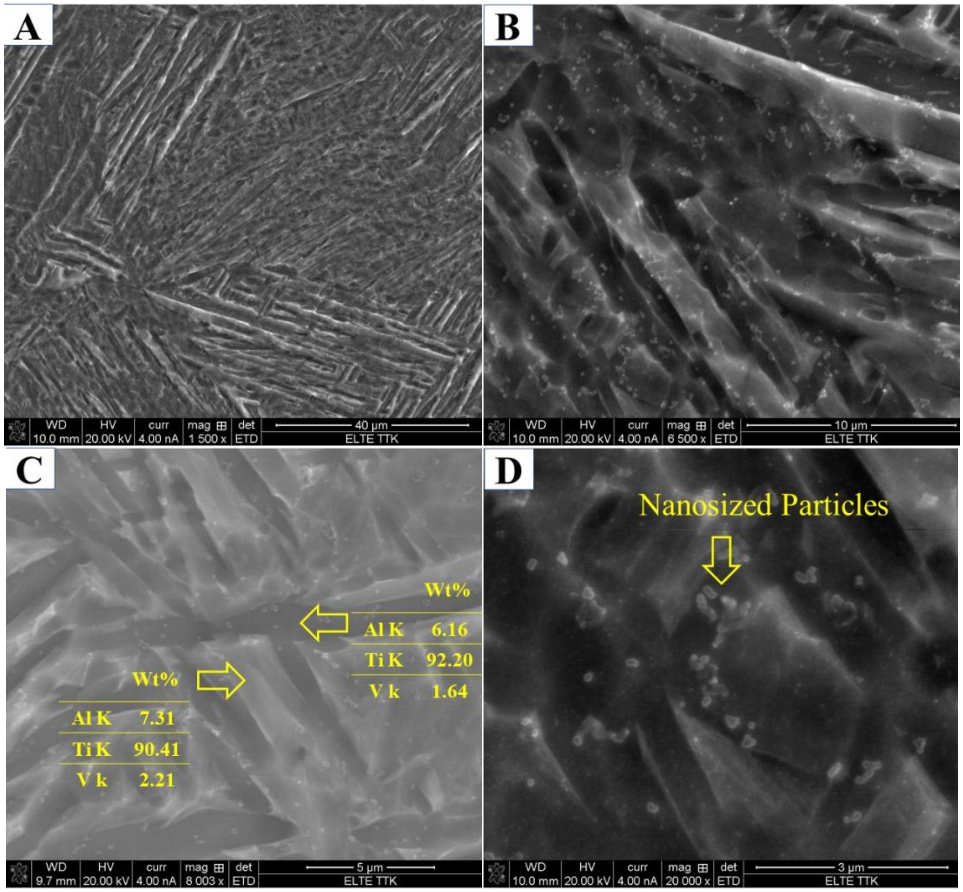


*Figure 2-17: SEM micrographs showing microstructure of the HT850WC sample at different magnifications indicating the formation of a dual phase microstructure.*

The decrease in microhardness in the microstructure of the HT850WC specimens from 377 to 331 HV, as shown in Figure 2-10, indicates that the α″ formed during water quenching. Consequently, the microstructure of the HT850WC specimen was a complex mixture of α, α″, β

and $\beta_r$. Figure 2-17 (d) shows the microstructure of the HT850WC specimen at high magnification, indicating that some nanoscale particles are dispersed on the α phase, which are confirmed to be β phase by Ref [132].

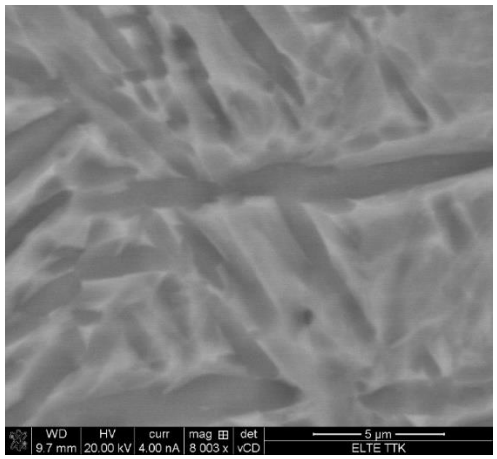


*Figure 2-18: SEM (BSE) micrograph showing microstructure of the HT850WC sample indicating the consid-erable chemical contrast between two phases.*

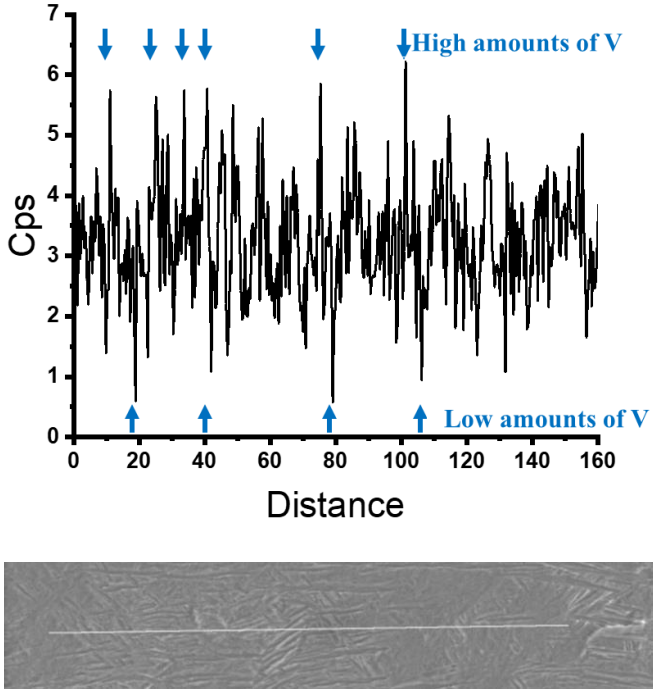


*Figure 2-19: The line scan EDS results of HT850WC showing some areas are rich in V and some are poor in V.*

Ageing of the HT850WC specimen at 550 °C for 3h results insignificant changes in the diffraction pattern (Figure 2-20). Three reflection peaks (110), (211), and (220) belonging to the

β phase have formed instead of two in comparison to the HT850WC specimen. In addition, a new weak reflection peak (110) belonging to the α″ phase is observed at 2Θ=34.73°. This indicates that new phases (β and α″) are precipitated during ageing. On the other hand, the microhardness measurements of the HT850WC+AG specimen (Figure 2-10) indicated an increase in hardness compared to the HT850WC specimen (343 HV versus 330 HV). On combining the XRD result with the microhardness result, we deduce that the α″ partially decomposed and transformed into the α, β and α″ phases. Figure 2-21 (a to d) presents the SEM and optical micrographs showing microstructure of the HT850WC+AG specimen at various magnifications. The lattice parameters (a) of the β phase in the HT850WC specimen (a = 3.2419 °A) were higher than those in HT850WC+AG specimens (a = 3.2001 °A) as shown in the Table 2-2. The reason for this result is the difference in chemical composition. The EDS analysis of the β phase in the HT850WC specimen (7.31 wt.% Al, 90.41 wt.% Ti and 2.21 wt.% V) (Figure 2-17 c) confirms that this phase has a different composition than that of the HT850WC+AG specimen (5.50 wt.% Al, 88.44 wt.% Ti and 6.05 wt.% V) (Figure 2-21 d). The concentration of V in the β phase of the HT850WC+AG specimen is higher than HT850WC. The atomic radii of V (0.132 nm) are smaller than those of Al (0.143 nm) and Ti (0.147 nm) [140]. As a result of the enrichment of the phase with Vanadium, the lattice parameter of (a) decreases. As shown in Table 2-2, decreasing the lattice parameter of (a) causes the phase angle to move to a higher angular location, from 2Θ = 39.25 to 39.80° for the (11 0) peak.

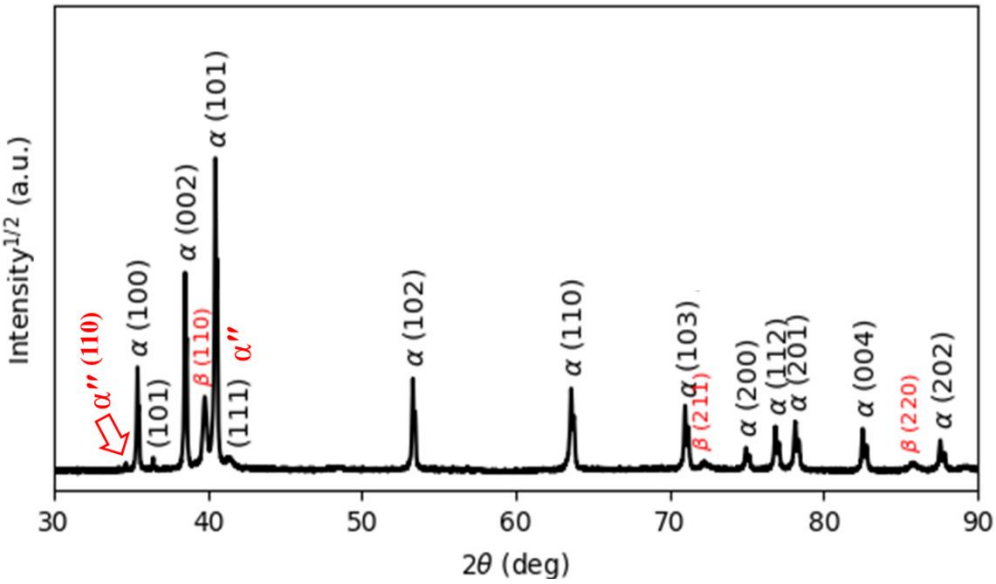


*Figure 2-20: The XRD pattern of the HT850WC+AG sample indexing α, β, and α″ phases.*

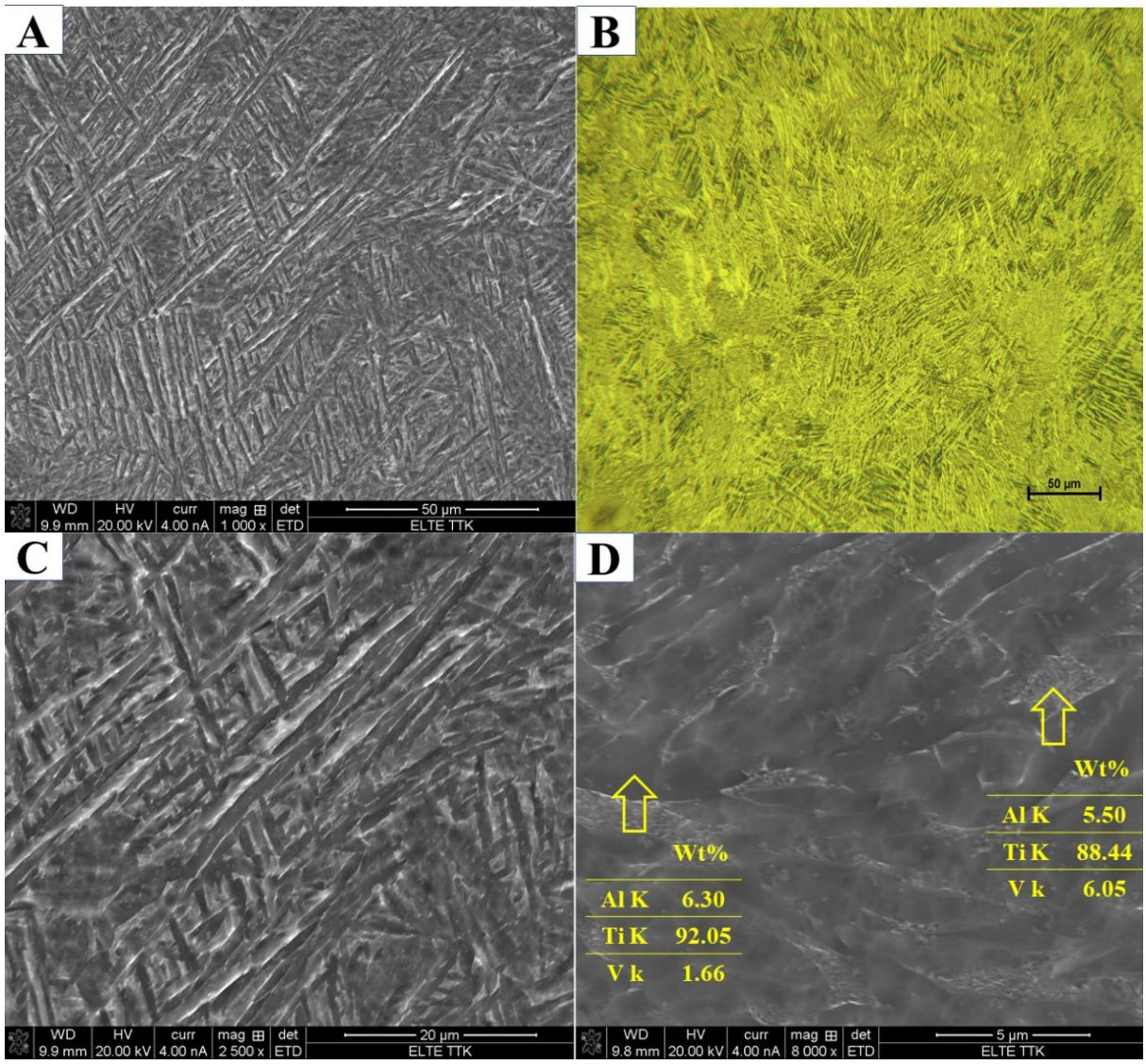


*Figure 2-21: SEM and optical micrographs showing microstructure of the HT850WC + AG sample at various magnifications.*

After aging the HT850 WC specimen at 550℃, the average lath thickness of α phase was increased from 1.024 to 1.342 µm and the average volume fraction of α phase was increased from 68.42 to 74.39%. According to the microstructure of the HT850WC+AG specimen at high magnification in Figure 2-21 d, this considerable grain growth is due to the transformation of nanoscale particles dispersed on the α phase in the microstructure of the HT850WC (Figure 2-17 c) into the α phase. The EDS in Figure 2-21 d would seems to show that for the HT850WC+AG treated specimens, the β phase poor in vanadium re-maintenance itself during aging by increasing the concentration of vanadium from 2.28 wt% for the HT850WC specimen to 6.05

wt% for the HT850WC+AG specimen due to the diffusion of vanadium from decomposed nanoscale particles into the β phase.

Subtransus heat treatment at 850 °C for 2 hours, followed by furnace cooling and water quenching, highlights approximately different microstructure evolution, as detailed in Figure 2-22. A comparison of the two figures, it can be seen that there are significant differences in the thickness of α phase. The average lath thickness of α phase is 1.403 µm after furnace cooling and 1.024 µm after water quenching. Nevertheless, the lath thickness of α phase was higher after furnace cooling than after water quenching, which can be attributed to the low cooling rates during furnace cooling that allow the grains to grow. Therefore, we can conclude that cooling rate is an important factor when cooling from 850°C below the $\beta_{tr}$. It is worth mentioning that the volume fraction of α phase is higher after furnace cooling than after water quenching. The average volume fraction of α phase after furnace cooling and after water quenching was found to be 78.71% and 69.42%, respectively.

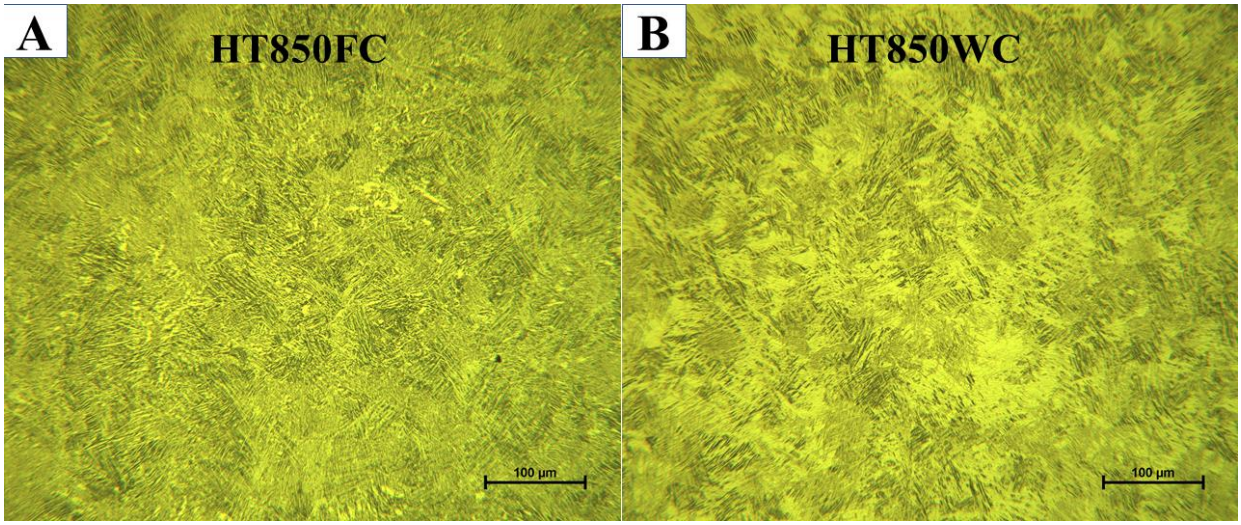


*Figure 2-22: Comparison of the structure morphologies similarity for sample HT850FC and sample HT880WC.*

#### *2.5.1.3 Microstructure of supertransus heat treatments*

Figure 2-23 A presents the XRD patterns of the HT1020FC specimen in which reflections related to α and β phases were identified. It is interesting to note that some reflections such as (200), (112), and (201) consist of a series of subpeaks as shown in Figure 2-23 B. According to the literature, these findings demonstrate that α phases are precipitated at different temperatures with

the same a and different c lattice parameters [135]. At the same time, the chemical composition and morphology of the α phases precipitated at different temperatures are also different. Figure 2-24 shows the optical and SEM images of Ti64 microstructure after HT1020FC heat treatment, revealing a lamellar microstructure of α and β phases. Figure 2-24 (C) shows the chemical composition of these phases. As can be seen, the β phase is rich in V (12.75 Wt%) compared to the α phase (0.63 Wt%). The mean amount for β phase after HT1020FC was about 9.14 ± 1 wt.%. Peak temperatures above the $\beta_{tr}$ occur during this heat treatment, which convert the α′ microstructure to 100% β. Owing to the slow cooling rate, β is subsequently converted to the dual phase microstructure of α and β. It is noteworthy that some grains of α phase exhibited particles of β phase, as highlighted by a yellow circle in Figure 2-24 (c and d). The presence of β particles has been reported in heat treatment of as-manufactured Ti64 at 1150 °C for 2 hours followed by air cooling [141]. The hardness values of the HT 1020 FC averaged at 342 HV, is lower than the hardness of the as-manufactured specimen. This is due to the decomposition of α′ martensite as well as the grain coarsening of α phase during the heat treatments.

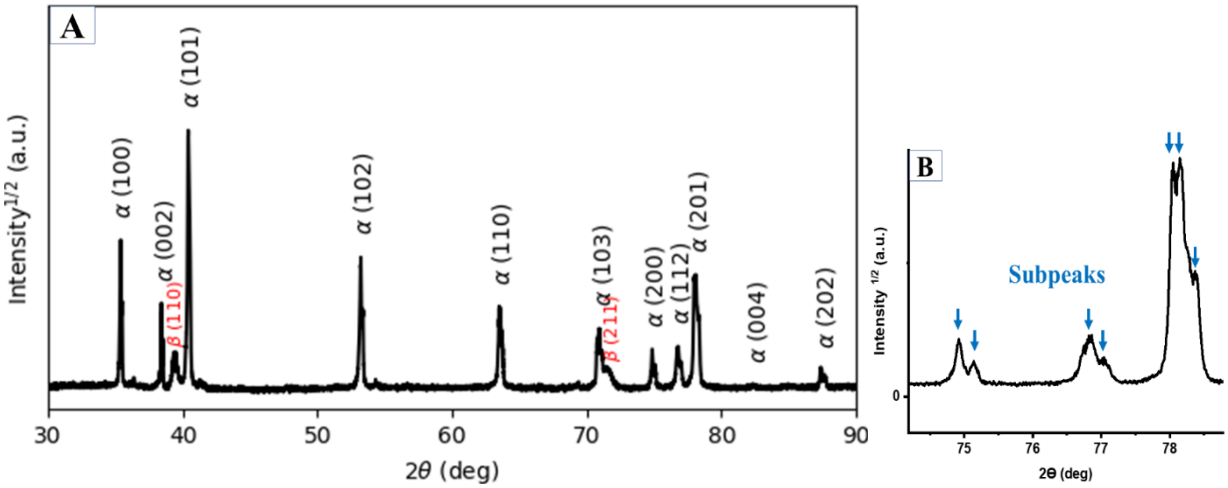


*Figure 2-23: A: The XRD pattern of the HT1020FC sample indexing α and β phases. B: Enlargements of the (200), (112), and (201) peaks from 74° to 80° diffraction angles indicating the formation of subpeaks.*

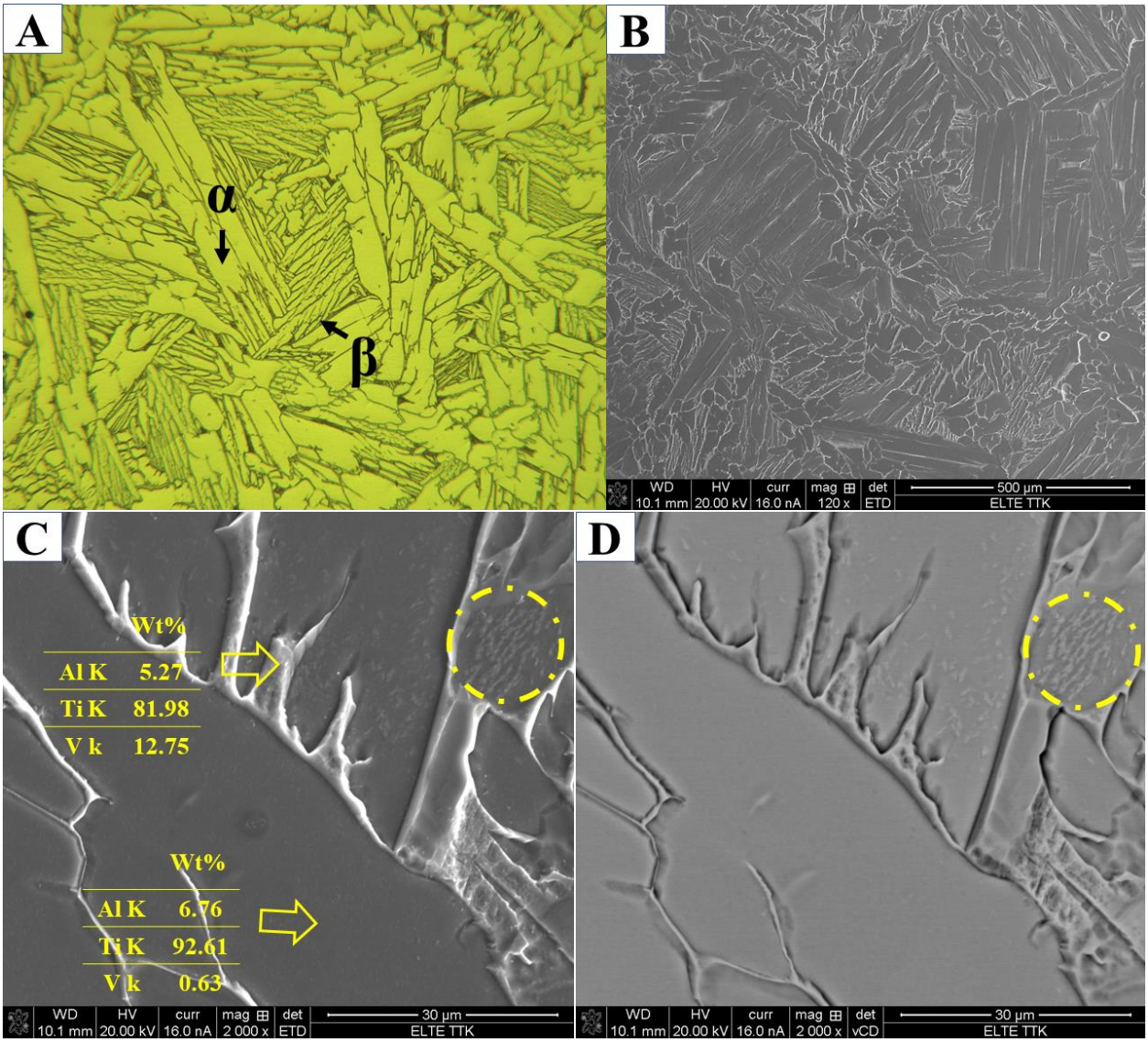


*Figure 2-24: SEM and optical micrographs showing microstructure of the HT1020FC sample at various magnifications.*

The microstructure analysis of HT1020WC specimens after XRD measurements (Figure 2-25) showed the presence of α′, α, and α″ phases. No evidence of β phase was found. In contrast, α′, α, β, and α″ phases were revealed in the HT1020WC+AG specimen (Figure 2-26). Moreover, the intensity of the (110) peak was significantly higher in the HT1020WC+A specimen than in HT1020WC. Both α and α′ phases exhibit a hexagonal structure. Therefore, it is difficult to distinguish between α and α′ phases by XRD. One of the most important metallurgical differences between α and α′ phases is the content of V element. The content of V of α′ phase is higher than that of the α phase, which is due to rapid cooling that prevents the diffusion of

vanadium. Figure 2-27 shows the SEM and optical micrographs of the HT1020WC specimen at different magnifications. As can be seen, the EDS analysis (Figure 2-27 C) reveals that α′ phase is rich in V (3.19 Wt%) compared to the α phase (0.42 Wt%). The formation of α and α′ phases instead of α′ martensite is surprising. According to previous studies [142], the β phase formed when heated above $\beta_{tr}$ temperature is converted to a complete α′ martensitic phase when quenched with water. However, the reason is probably that the $\beta_{tr}$ of the powder can be higher than 1020 °C. The higher hardness of HT1020WC (~ 379 HV) compared to as-manufactured specimen (~ 377 HV) is due to the formation of α′ martensite plus α phase.

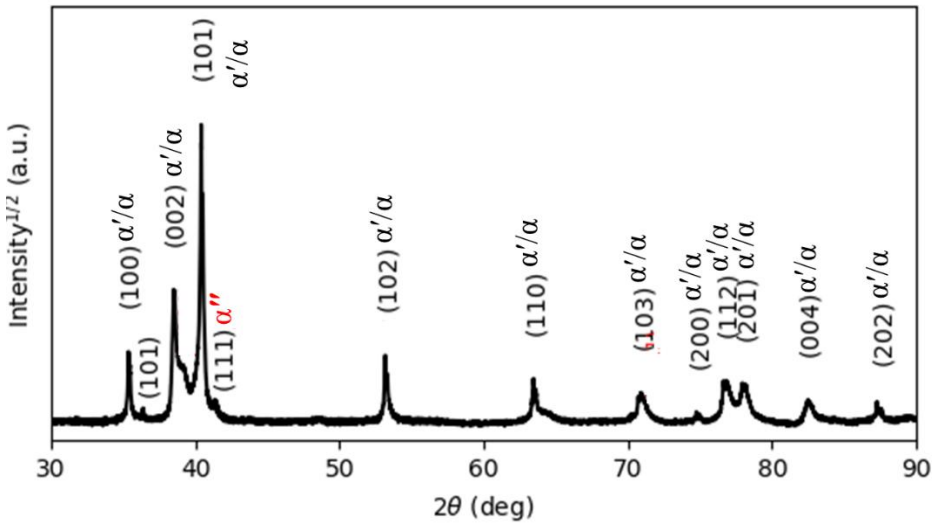


*Figure 2-25: The XRD pattern of the HT1020WC sample indexing α′, α, and α″ phases.*

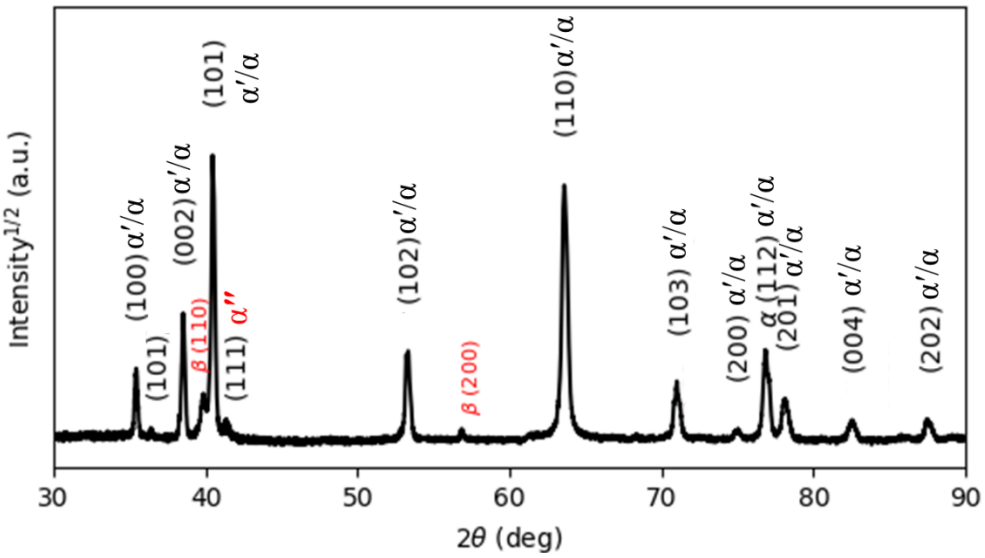


*Figure 2-26: The XRD pattern of the HT1020WC+AG sample indexing α′, α, β, and α″ phases.*

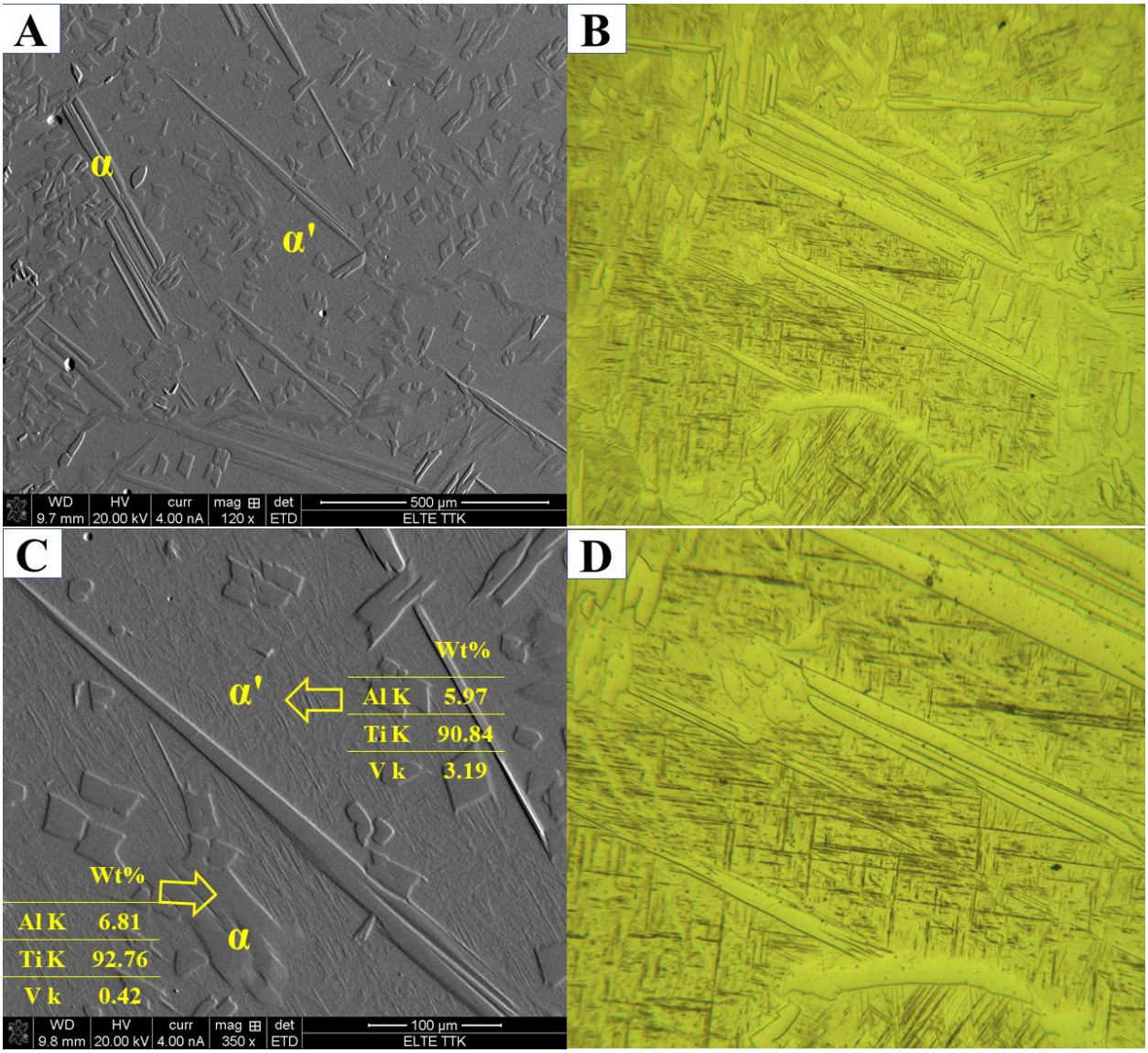


*Figure 2-27: SEM and optical micrographs showing microstructure of the HT1020WC sample at various magnifications.*

In contrast to the HT1020FC process, where the formation of α+β lamellae were the main metallurgical features (Figure 2-24), in the HT1020WC process the columnar prior β structure of the as-manufactured Ti64 is replaced by semi-equiaxed β grains with a diameter of about 170 µm with longer elongated α grains and α′, as shown in Figure 2-28. The β phase undergoes more complicated microstructural transformations during solidification after HT1020WC, such as the formation of the α′ phase by the displacing transformation with a shear mechanism and the formation of the semi-equiaxed β grains morphology by a nucleation process.

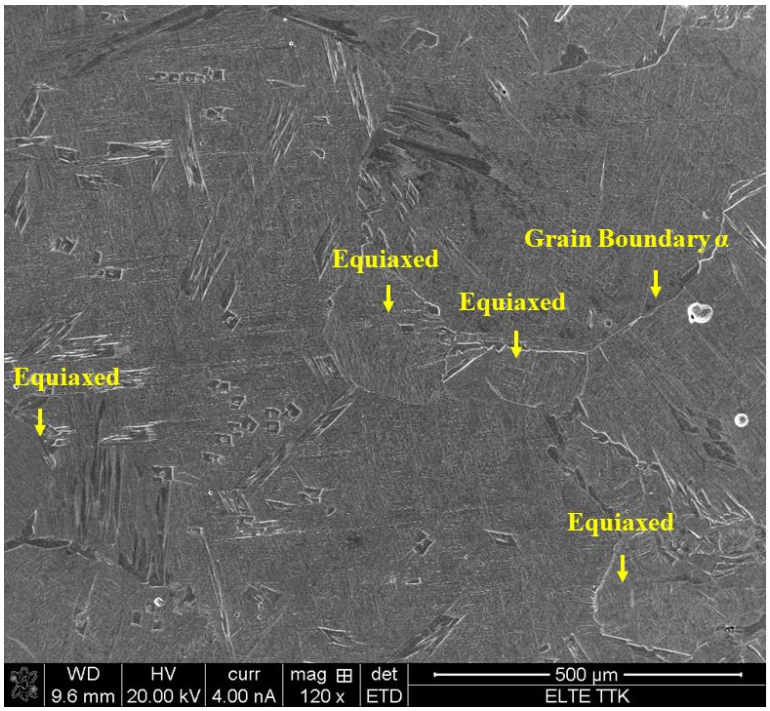


*Figure 2-28: SEM micrograph showing semi-equiaxed β grains morphology of the HT1020WC sample.*

The effect of aging (550 °C/3 h/FC) on the microstructure of HT1020WC specimens is summarized in Figure 2-29 at various magnifications. It can be seen that the longer elongated α grains have started to fragment and globularize as indicated by the arrows in Figure 2-29. This result leads us to conclude that the aging is the key factor in determining the final dimensions and the morphology of the α phase. The formation of β phase after HT1020 WC+AG was not revealed by optical and SEM results. In contrast, XRD result after HT1020 WC+AG indicating the formation of a small amount of β phase (Figure 2-26). The microhardness results confirm the SEM result of HT1020 WC +AG, as there is a slight increase after aging (384 HV instead of 379 HV for the HT1020WC specimen). Figure 2-30 shows the microstructure of the HT1020 WC+AG specimen at a higher magnification. It can be seen that some nanoscale particles are dispersed on the α-phase.

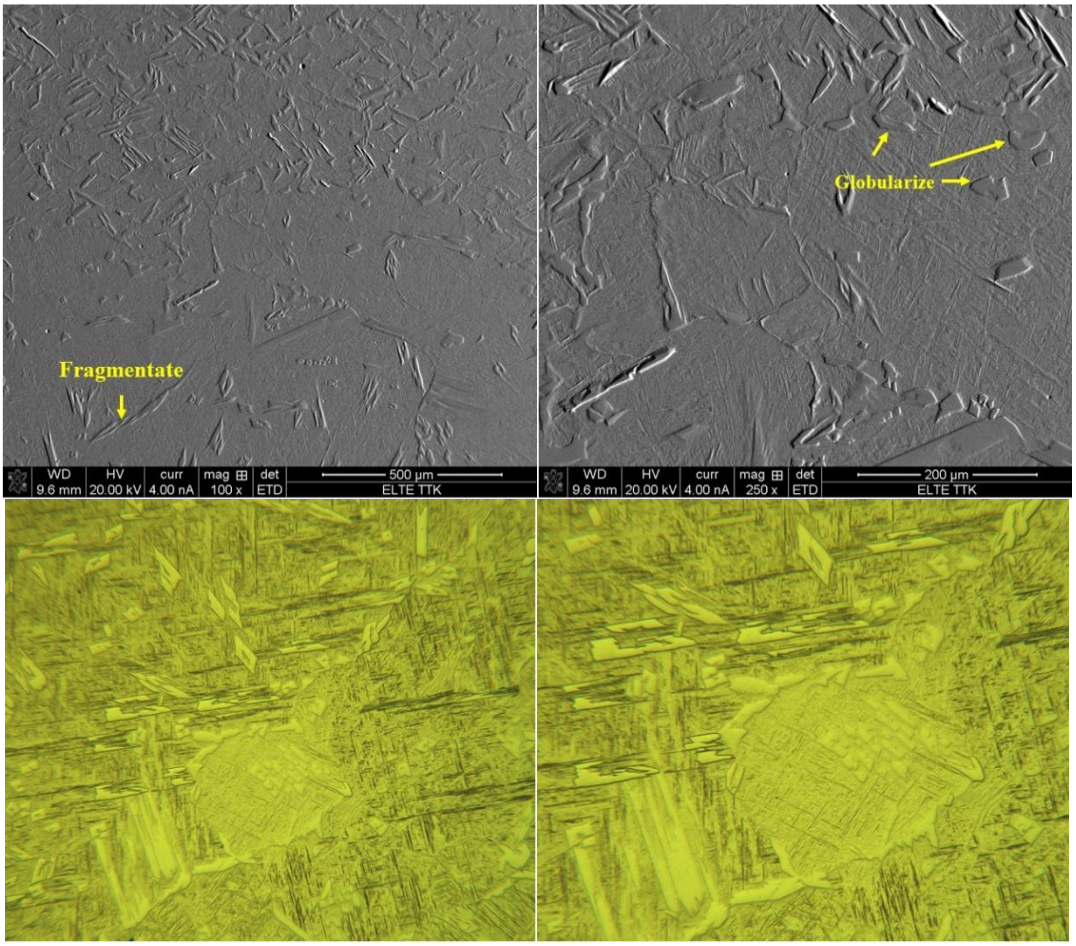


*Figure 2-29: SEM and optical micrographs showing microstructure of the HT1020WC+AG sample at various magnifications.*

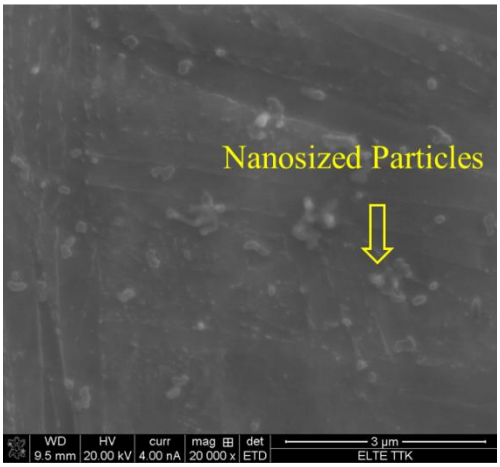


*Figure 2-30: SEM micrographs at higher magnifications showing microstructure of the HT1020WC+AG sample indicating the formation of β nanosized particles dispersed on the α phase.*

### 2.5.2 Tensile properties

The results of the mechanical properties obtained from the tensile test of as manufactured and heat-treated specimens are summarised and compared in Table 2-3. As expected, the as-manufactured specimen has a high yield (1060 MPa) and a high ultimate tensile strength (1180 MPa) but a low ductility (8%) of less than 10%. This is due to the formation of a fine α′ martensitic microstructure. Interestingly, the ductility of all heat-treated SLM specimens is higher than that of the as-manufactured specimen, except for specimen (HT1020WC+AG). On the other hand, the strength of all heat-treated SLM specimens is lower than that of the as-manufactured specimen. This is might be explained by the complete decomposition of α′ and the coarsening of the microstructure of heat-treated specimens compared to the original fine α′ martensite.

The evolution of mechanical properties during heat treatment of SLM parts is controlled by the decomposition of α′ martensitic microstructure. It is important to note that the HT850FC produces the best possible combination of ductility (13%) and strength properties ($\sigma_y$=932, $\sigma_u$=986 MPa) and the microstructure is comprised of β and α phases among all. This is due to the formation of β phase in Ti64 alloy, resulting in a decrease in tensile strength and an increase in ductility. The lower strength of HT850WC ($\sigma_y$=870, $\sigma_u$=930 MPa) and HT850WC+AG ($\sigma_y$=892, $\sigma_u$=970MPa) compared to HT850FC ($\sigma_y$=932, $\sigma_u$=986 MPa) could be interpreted that the soft martensitic α″ microstructure is formed in prior β grains during rapid solidification of β phase, upon water quenching.

It has been found that the mechanical properties of Ti alloys are a function of thickness of α lath and α colony as well as grain boundary α [143]. A larger α-lath and a complete degradation of α′ martensite may describe the lower strength of treatment at HT1020FC ($\sigma_y$=748, $\sigma_u$=833 MPa) in comparison with HT850FC. The average lath thickness of α phase was 10.63 µm after HT1020FC compared to 1.403 µm after HT850FC and 0.420 µm after printing.

HT1020WC exhibits high strength ($\sigma_y$=878, $\sigma_u$=990MPa) and low ductility (8.6) compared to all heat treatments processes. At the same time, the tensile strength of the HT1020WC specimens decreases compared to the as-manufactured specimens, but the ductility does not increase. This is due to the presence of 27.33 vol.-% of lamellar α and 72.67 of α′ in microstructure instead of complete α′, which leads to a decrease in strength. Another possible reason is that the lath

thickness of α (13.6 μm) in HT1020WC specimens is higher than that of the as-manufactured and other heat treatments specimens, which can reduce the mechanical properties.

Interestingly, the strength of the HT850 WC+AG (σy=944, σu=1035 MPa) is slightly higher than that of HT1020WC but its ductility is lower (7.2%). The reason is probably the presence of some nanoscale β particles distributed on the α′, which in turn increases the strength and decreases the ductility.

*Table 2-3: Mechanical properties of the of as printed sample and samples subjected to different heat treatments.*

| No. | T/ºC | t/h | Cooling Rate | Aging | | | YS/MPa | UTS/MPa | BE% |
|---|---|---|---|---|---|---|---|---|---|
| | | | | T/ºC | t/h | Cooling | | | |
| 1 | | | | | | | 1060 ± 21 | 1180 ± 29 | 8 ± 0.2 |
| 2 | 850 | 2 | FC | - | - | - | 932 ± 6 | 986 ± 9 | 13 ± 0.15 |
| 3 | 850 | 2 | WC | - | - | - | 870 ± 8 | 930 ± 13 | 10.4 ± 0.3 |
| 4 | 850 | 2 | WC | 550 | 3 | FC | 892 ± 5 | 970 ± 23 | 9.3 ± 0.27 |
| 5 | 1020 | 1 | FC | - | - | - | 748 ± 12 | 833 ± 10 | 14.5 ± 0.6 |
| 6 | 1020 | 1 | WC | - | - | - | 878 ± 17 | 990 ± 11 | 8.6 ± 0.24 |
| 7 | 1020 | 1 | WC | 550 | 3 | FC | 944 ± 14 | 1035 ± 19 | 7.2 ± 0.13 |

## 2.6 Conclusions

1. In the microstructure of Ti64, a very fine acicular martensite α′ with a small amount of β and α″ structure developed due to the extremely high cooling rate associated with the SLM. Microstructural observations confirmed the complete decomposition of the fine acicular martensite α′ during the post heat treatments cycle, the transformation of α′ to α, β, and α″ phases, and the formation of some nanoscale β particles during the cooling stage, confirming the need for post treatments after SLM of Ti64.
2. The optimal mechanical properties were obtained by heat treatment at 850 °C followed by cooling in the furnace. This heat treatment enhanced the ductility to 13%, compared to 8% for as-manufactured specimens The improved ductility of the HT850FC can be attributed to the complete decomposition of α′ into mainly α plus β and small amount of

α″ phases as well as the coarsening of the microstructure of HT850FC compared to the original fine α′ martensite.

3. No improvement in mechanical properties was observed for HT850WC due to the formation of soft orthorhombic α″, α, and β. The presence of α″ is responsible for a significant decrease in hardness.
4. Microstructure of HT1020FC is featured by the formation of an α+β lamellar. In contrast, the microstructure of HT1020WC is featured by the formation of semi-equiaxial β-grains with a diameter of about 170 μm with longer, elongated α-grains and basket-weave α′. Moreover, XRD analysis confirmed the presence of α″.

# 3 Selective Laser Melting of Ti6Al4V-Hydroxyapatite

## 3.1 Introduction

Metallic alloys (stainless steel, CoCrMo, Ti alloys) are biomaterials used in orthopedic bone, joint replacements, and dental implants to interact with living tissue. Due to their excellent biocompatibility, high relative strength, favorable osseointegration, and superior corrosion resistance, Ti64 alloys play a crucial role in biomedical applications. Moreover, the elastic modulus of Ti64 alloys (105-110 GPa) is lower than that of 316 L stainless steel (210 GPa) and cobalt-chromium alloys (230 GPa) [144]. Although Ti64 has many remarkable properties, there are also some unresolved issues regarding bone resorption, stability and fixation of Ti64 implants, and the body's inflammatory response.

The resorption of the bone is a process of bone loss resulting from the large difference in Young's modulus between bones (10–30 GPa) and the Ti64 implants (105-110 GPa) for younger patients under 40 years [145]. The significant difference in Young modulus results in a non-gradual transfer of stresses to the bone surrounding the implant, resulting in stress shielding and bone absorption. Figure 3-1 illustrates the natural history of this problem clearly.

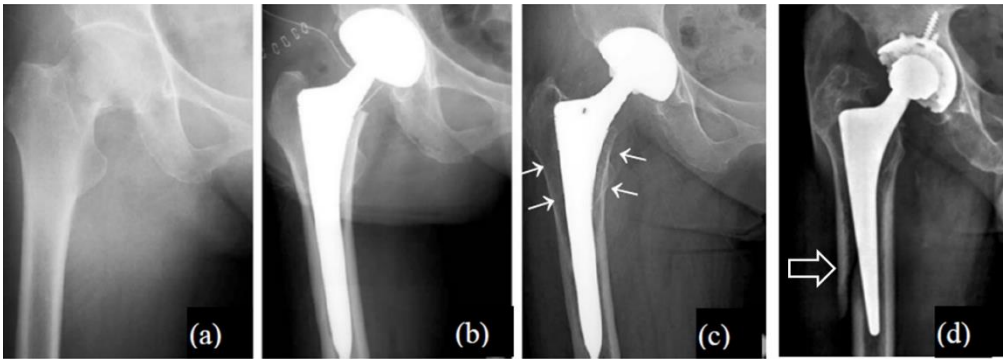


*Figure 3-1: a: Before the surgery. b: Immediately after the surgery. c: Beginning of the bone resorption. d: Fracture* [146].

Stability and fixation of a Ti64 implant inside the bone and bone ingrowth at the interface are the greatest challenges after implantation [147]. There are several types of implant fixation: bone cement, mechanical fixation (screws), and activated surfaces of implants (coating)[74]. Bone cement is used in hip replacements to fix the bone stems, and to tackle the Young's modulus mismatch between the implant and the bone. The major limitation of bone cement is related to the cracks or infections which may occur after implantation in the joint [148]. In recent decades,

coating implants with hydroxyapatite (HA) has been an innovative alternative to cemented fixation [149]. Although implants coated by HA show good interfacial bonding between bone tissue and implants [101], there have been some issues regarding the failure of the metal coating at the interface, for which there is still no accepted solution [95, 96]. Another disadvantage of using Ti64 implants is that they allow the release of metallic ions which leads to an inflammatory reaction in the bone surrounding the implant[150].

## 3.2 Objective

This work outlines a SLM of Ti64-HA as a composite powder to solve the main Ti64 implant problems. HA was added in order to provide a solid biological fixation between Ti64 implants and bone tissue without the use of bone cements. It is well known that the crystallographic and chemical composition of HA ($Ca_{10}(PO_4)_6(OH)_2$) is similar to that of bone tissue, which can dramatically enhance osseointegration and biological fixation. Other advantages of HA, which may have reduced inflammatory reaction or allergic risk and accelerated bonding, are bioactive, biocompatible, non-inflammatory, non-toxic, non-immunogenic and osteoconductive [47].

Until recently, very little research has been carried out on the SLM of Ti-HA composites. Han et al.[106] investigated the microstructure and mechanical properties of SLM-processed pure titanium (CP Ti)-HA composites. Marcu et al.[151] studied the effect of SLM variables on the microstructure evolution and mechanical properties of Ti6Al7Nb-HA composites. Therefore, the present paper aims to study the phases, microstructure, and mechanical properties of Ti64 - 2%HA composite samples manufactured by SLM. Moreover, the microstructure and mechanical properties of Ti64-2%HA were compared with pure SLM-fabricated Ti64.

## 3.3 Materials and Methods

### 3.3.1 Materials preparation

In this work, 2wt% HA powder (nanoXIM•HA203, fluidinova, Portugal) was added into Ti64 powder (Gr.23, LPW Technology/UK) followed by mechanical mixing and SLM processing. Figure 3-2 schematically describes preparation and manufacturing process. The gas-atomized spherical Ti64 powder (Figure 3-3 a) had a nominal particle size of 15 to 45 µm. Figure 3-3 b shows SEM microscopic images of the mixture of the Ti64 and HA powders and their diameter distributions. The hydroxyapatite powder had an average particle size $d_{50}$ of 10 $\mu$m and specific

surface area ≥ 100 $m^2/g$. Mechanical mixing to produce the composite Ti64 -2%HA was performed with a planetary ball mill (Retsch PM400). The mixing time was 8 h.

*Figure 3-2: Schematic representation of preparation and manufacturing process.*

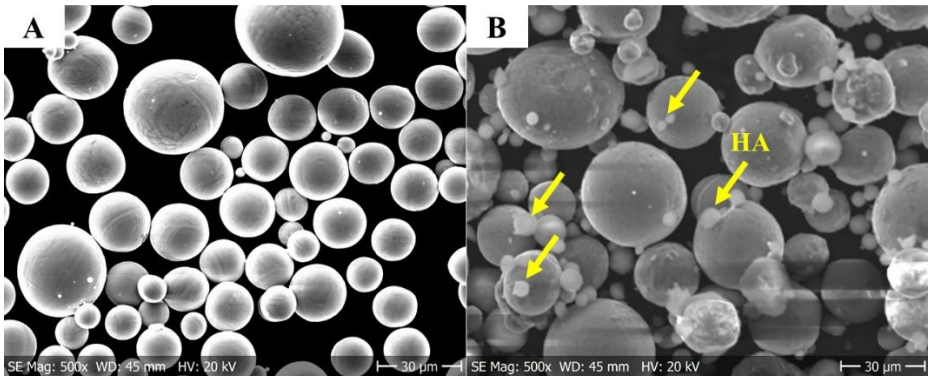


*Figure 3-3: Morphology of the powders.: a) SEM micrograph of pure Ti64 powder. b) SEM micrograph Ti64 powder mixed with 2 wt% of HA powder.*

### 3.3.2 SLM system and processing

SLM was conducted with a commercial SLM (Sisma MYSINT 100) system with a 200 W laser fiber and a 55 µm laser spot. Laser power, scanning speed, and layer thickness were kept constant (optimum conditions) at 125 W, 1000 mm/s, and 20 µm, respectively. Parameters of

SLM are selected based on a guideline available with a Sisma MYSINT 100 machine and some trial and errors. Pure argon gas was used to shield at a flow rate of 35 L/min.

The tensile test was conducted to investigate the mechanical performance of the printed samples. Mechanical performance of the printed samples was described in terms of yield and ultimate tensile strength and the total elongation. The sample dimensions were as described by ASTM E8. The tensile test was conducted through the use of a non-computerized testing machine (FORM+TEST, Model: TTM 100, Germany) at a crosshead speed of 1mm/min. Average of three tests is performed for each tensile testing.

### 3.3.3 Materials characterization

Samples for metallographic examination through the cross section were prepared using standard metallography procedure, and Keller's reagent (92 mL H20, 6 mL HNO3, and 2 mL HF) was used to reveal the microstructure. X-ray diffraction (XRD) with Cu-Kα radiation and the wavelength of λ= 1.5406 Å at 40 kV and 30 mA was used to determine the phase constituent of the microstructures of the printed samples. In order to investigate of the microstructural evolution, optical microscopy (OM, Neophot 2, Jena, Germany) and FEI Quanta 3D scanning electron microscope (SEM) fitted with an EDS were utilized. The EDS spot examinations was carried out to describe the chemical composition of the phases. To examine the chemical composition profile across the grain boundaries and phases, the EDS line scan analysis was done. EDS mapping analysis allowed to characterize the distribution of the HA (Ca, O and P spectra) precipitates on the Ti64 matrix. In order to understand the relationship between the microstructure and mechanical properties, Microhardness Vickers testing (Leitz-Wetzlar, Germany) was conducted with a dwell time of 10 s and a load of 0.5 kg f. Furthermore, micro/ nanoindentation tests (CSM micro-indentation tester) was done with an applied load of 3500 mN and holding time of 10 s.

## 3.4 Results and Discussion

### 3.4.1 Material behavior during the SLM process of Ti6Al4V -HA composites

The Ti64 powder was mixed with different weight ratios of HA, including 2 wt%, 3 wt%, 4 wt % and 5 wt %. The Ti64-HA composites, especially with high amounts of HA, showed complicated production behaviour; several explosions (popups) occurred during SLM processing, resulting in the crash of the support structure. Figure 3-4 clearly illustrates this problem. As far as we know,

trapped water in the mesoporous structure of the HA powder or the decomposition of HA can generate $H_2O$ gases, which could be responsible for these explosions. It has been found [93, 152] that HA [$Ca_{10}(PO_4)_6(OH)_2$] dissociates into $H_2O$ (gas) and tetracalcium phosphate [$Ca_4(PO_4)_2O$] and/or tricalcium phosphate [$Ca_3(PO_4)_2$] at high temperatures above 1300 ºC.

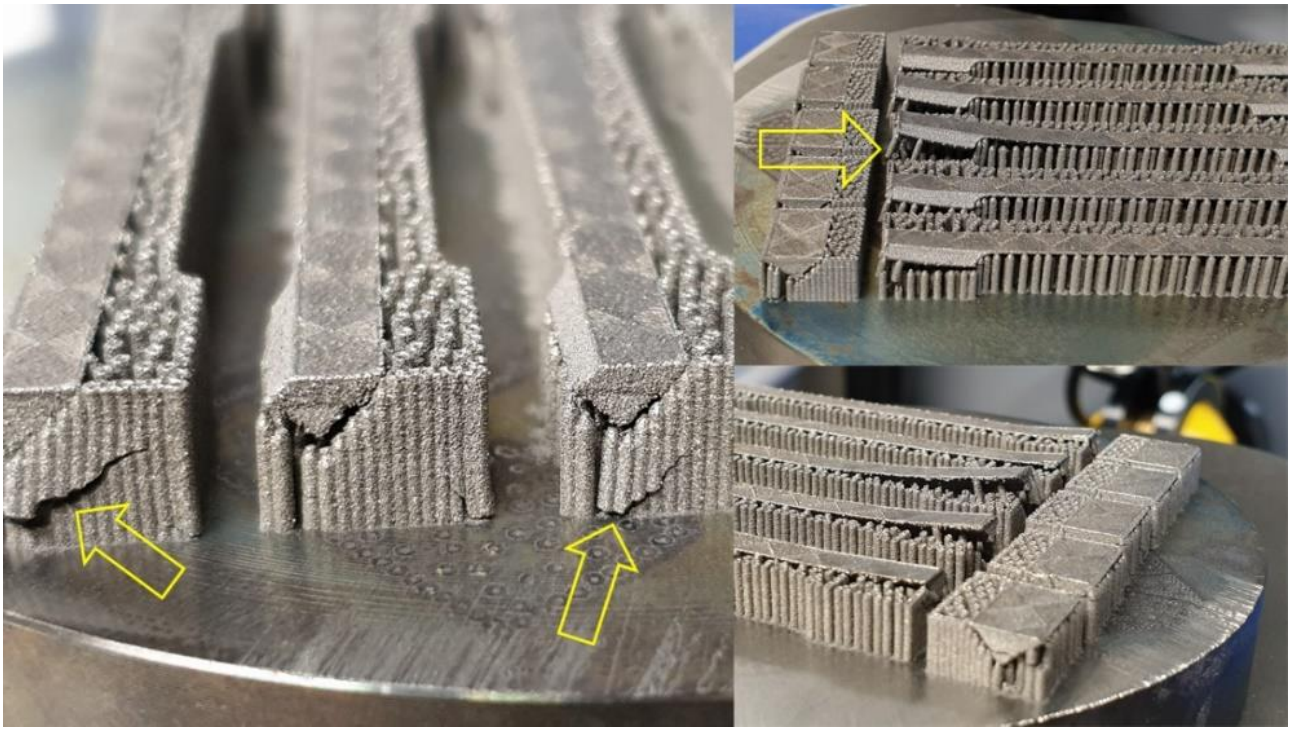

*Figure 3-4: The crash of the support structure during SLM of Ti64-2%HA composite.*

To eliminate the effects of trapped/generated water and reduce the impact of this "gas/explosion" problem on the SLM-produced Ti64 -2% HA, preheating of the HA powder is required. Therefore, the HA powder was heated to 1000 ºC for 2 hours and the heating and cooling rate was 10 ºC/min. Heat treatment of HA was performed in a muffle furnace at 1000 ºC for 2 hours and the heating and cooling rate was 10 ºC/min. After heat treatment, the HA powder was characterized by Fourier transform infrared spectroscopy (FTIR) and X-ray diffraction (XRD). The FTIR spectra (Figure 3-5) confirmed the stability of HA by the presence of peaks related to phosphate [$(PO_4)^{3-}$ and $PO_4$], $OH^-$, and $HPO_4$ groups, which are important in the molecules of HA. XRD analysis (Figure 3-6) indicated that the material is HA as shown by the (ICDD 00-024-0033) pattern.

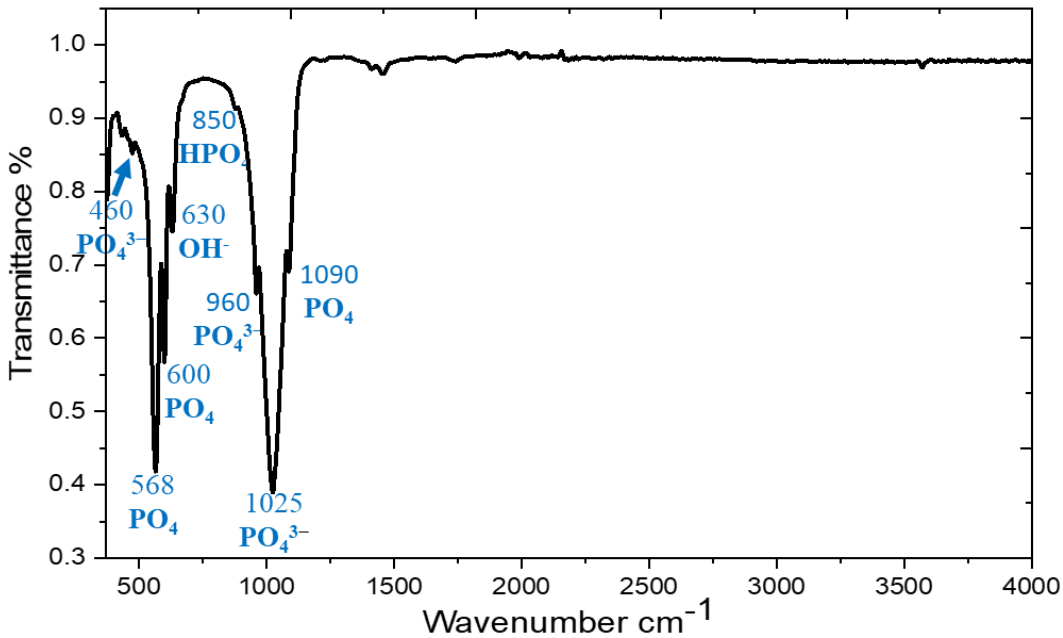


*Figure 3-5: FTIR spectra of HA powder heated at 1000 ºC.*

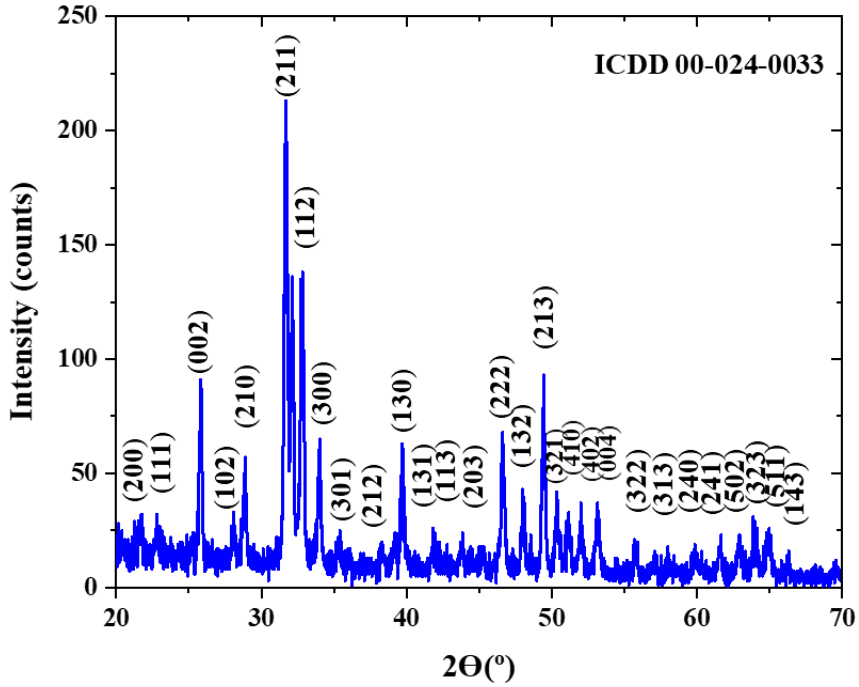


*Figure 3-6: X-ray diffraction pattern of HA powder heated at 1000 °C.*

### 3.4.2 Phase structure evolution

The results of OM and SEM for the Ti64 samples and Ti64-2%HA composites are compared in Figure 3-7. Figure 3-7 a and b show typical OM and SEM micrographs of the Ti64 samples

indicating a lath microstructure, consisting mainly of an α′ martensitic structure and a small amount of β-titanium (β-Ti) at grain boundaries. The analysis of XRD (Figure 3-8 a) confirmed findings of SEM and the formation of α′ martensite due to the appearance of hexagonal close-packed (hcp) peaks related to a martensitic structure. Figure 3-7 c and d show typical OM and SEM micrographs of the Ti64-2%HA composite showing the existence of small grain structures associated with dark grain boundaries and some light green areas. The phases formed during solidification of the Ti64-2%HA composite were investigated by XRD, EDS-line, EDS- spot and EDS-map.

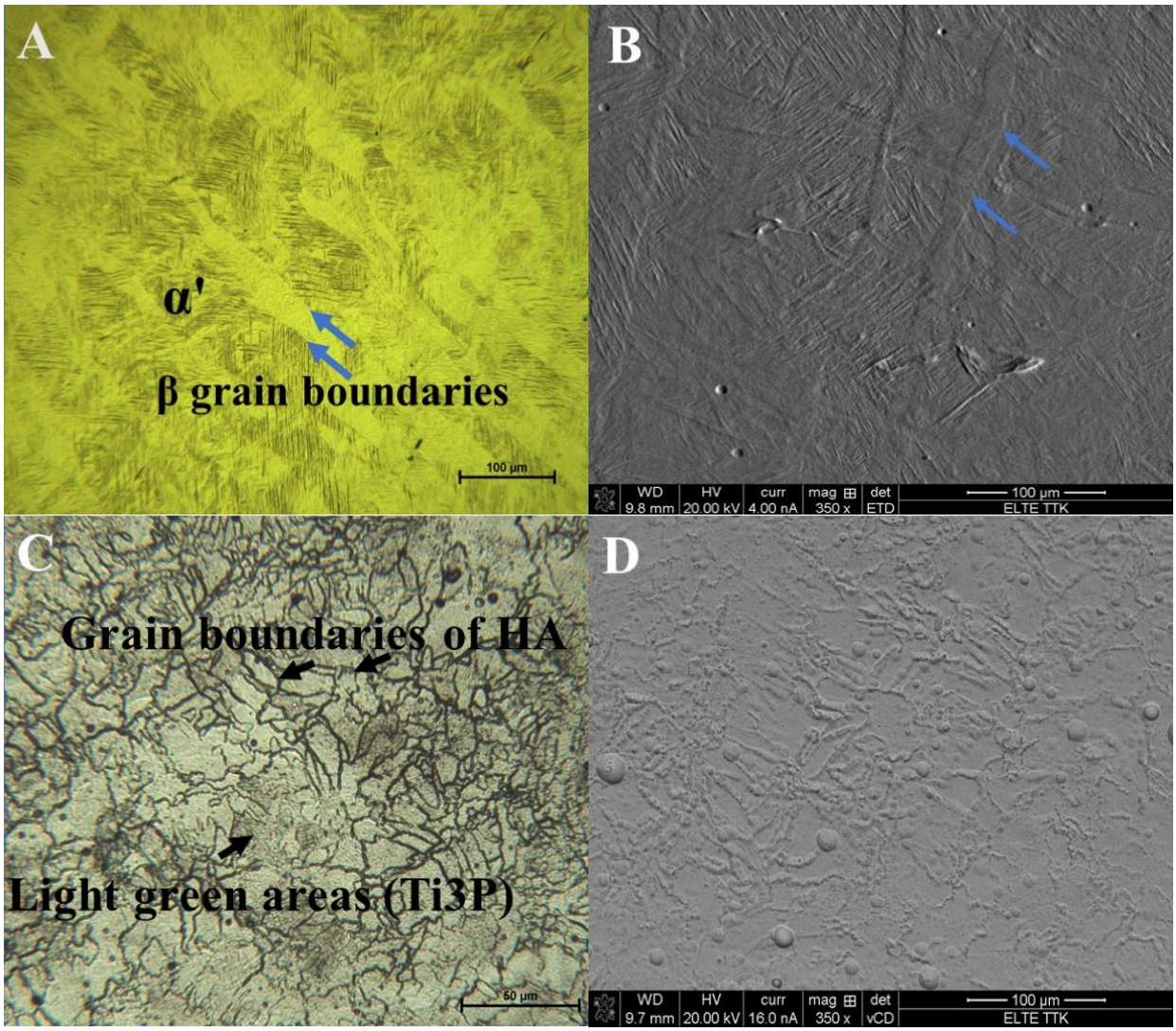


*Figure 3-7: a), optical image and b), SEM image showing microstructure of the Ti64 manufactured by SLM. C), optical image and d), SEM image showing microstructure of the Ti64-2%HA composite manufactured by SLM.*

Figure 3-8 b presents the XRD pattern of the Ti64-2%HA composites in which reflections of α Ti (hcp) and HA phases were revealed. The HA structure is indicated by the peak of 2Θ=57.2° which represents the (322) diffraction planes according to (ICDD 00-024-0033). This peak is virtually identical to the peak found in Ref [153]. Some phase identifications of Ti64-2%HA composites can be very difficult because the high concentration of Ti, which leads to strong diffraction peaks which in turn overshadow the peaks of the other phases which result from the decomposition of HA or interaction of Ti64-HA. Therefore, it would seem that the XRD identified other phases such as $Ti_3P$, different titanium oxides $Ti_xO$ ($Ti_3O$ and $Ti_2O$), and $CaTiO_3$. According to the Ti-P phase diagram (Figure 3-9) [154], P weight fraction of 24 can form the $Ti_3P$ phase. At the same time, the enthalpies of mixing of Ti-P, Ti-Al, and Ti-V are -100.5, -30, and -4 kJ/mol respectively [155]. Therefore, the P in HA could be reacting with the Ti in Ti64 to form the $Ti_3P$ phase during SLM. From the binary Ti-O phase diagram (Figure 3-10) [156], it can be deduced that O weight fractions of 20 to 40, $Ti_3O$, $Ti_2O$, and $Ti_3O_2$ can form in the structure.

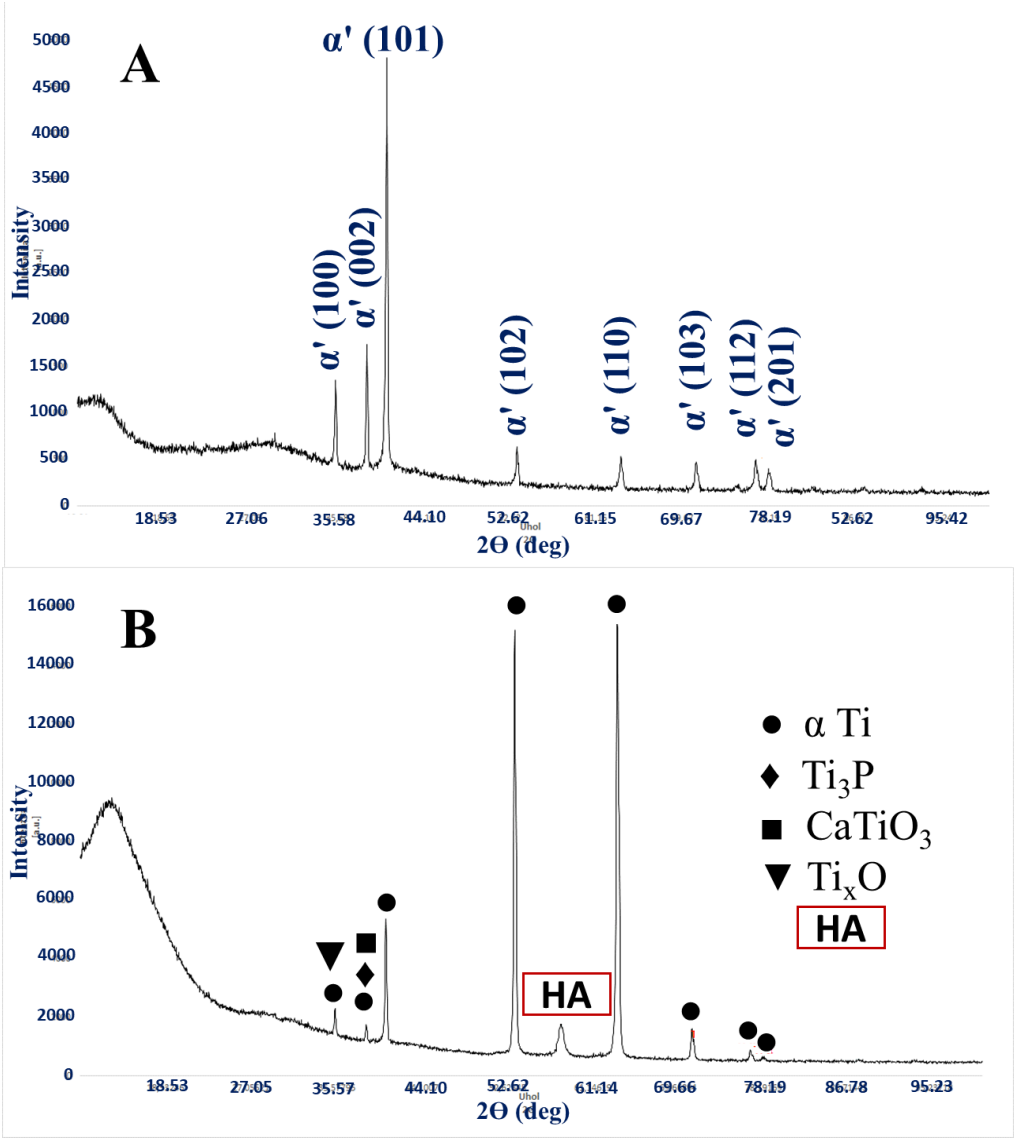


*Figure 3-8: a) the x-ray diffraction of the SLM of Ti64 indexing α' martensitic structure. b) the x-ray diffraction of the SLM of Ti64-2%HA indexing α Ti, HA, $Ti_3P$, $CaTiO_3$, and $Ti_xO$ phases.*

EDS mapping of the selected area (Figure 3-11) indicated a homogeneous distribution of Ti, V, and O, while the other elements P, and Ca were assumed to be inhomogeneous. It can be seen that in some zones there was no significant overlap between Ca, P and O, as shown in Figure 8 (white circles). On combining this result with the XRD, we conclude that the powders of HA were partially decomposed and interacted with Ti, which is converted into $Ti_3P$, $Ti_xO$, and $CaTiO_3$ phases. Moreover, the intensity of XRD peaks of Ti64-2%HA are significantly higher than that of Ti64. The decomposition of a certain percentage of HA has been reported in the selective laser sintering of NiTi–HA system [157].

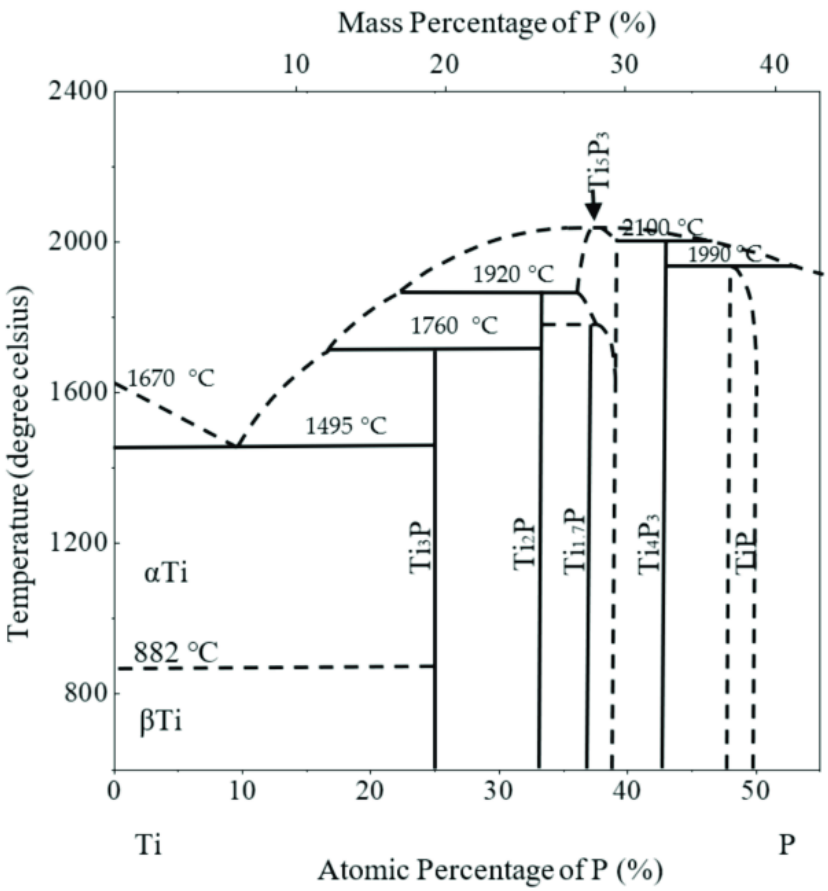


*Figure 3-9: Phase diagram of Ti-P (Titanium-Phosphorus) [154].*

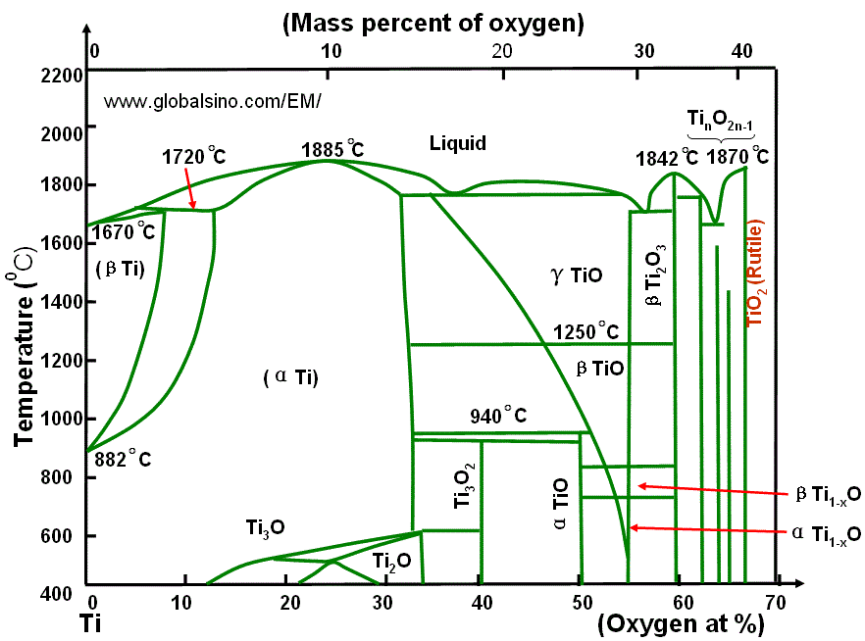


*Figure 3-10: Phase diagram of Ti-0 (Titanium-Oxygen) [156].*

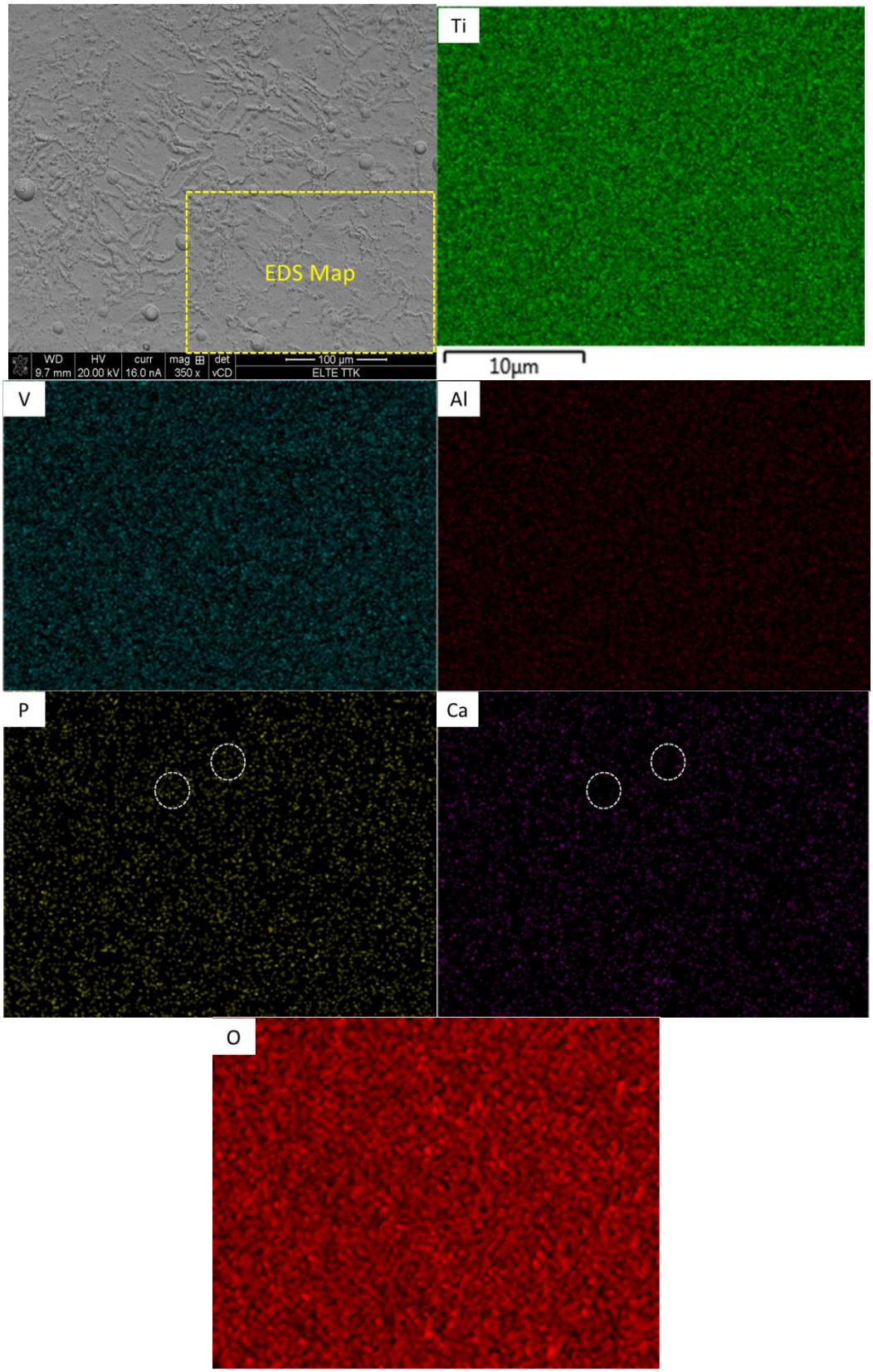


*Figure 3-11: EDS mapping analysis of SLM Ti64-2%HA composites.*

Figure 3-12 reveals EDS-line scan across the grain boundaries and inside grain domains in the structure, indicating the partitioning tendencies of Ti and O elements that are present in the grain boundaries when compared to that of the inside grain domains. As detailed in Figure 9, the phase formed in the grain boundaries is significantly enriched with O. The quite low and high concentration of the O element in the discrete peaks of O could be attributed to the formation of HA and $Ti_xO$. Another possible explanation for the formation of $Ti_xO$ is that the O element content is relatively high, which could have led the formation of some $Ti_xO$ in the microstructure after solidification as well.

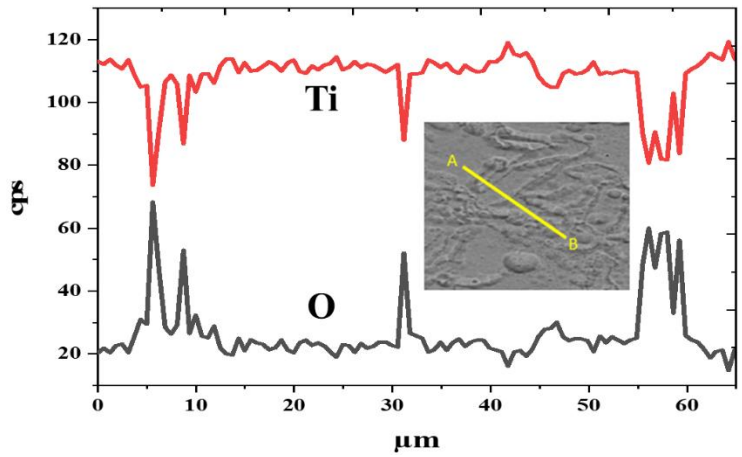


*Figure 3-12: EDS line scan across the grain boundaries in structure of SLM Ti64-2%HA composites.*

The EDS-spot analysis (Table 3-1) revealed that grain boundaries have small amounts of Ca and P, suggesting that HA is formed in the grain boundaries. The high tendency for precipitation of HA (Ca, P and O) in grain boundaries could be attributed to the low melting point of Ca, P, and O elements. A small amount of Ca and P can be explained by their partial absence during the standard metallographic procedure. It has been shown that nonmetallic elements (Ca and P) can be easily removed during grinding and polishing [158]. In addition, the EDS-spot analysis of the selected B and C points (Table 3-1) revealed that these points are enriched in phosphorus, suggesting that $Ti_3P$ is formed in these points. It is interesting to note that some spherical nano-sized white particles are found to be dispersed on the microstructure of the Ti64-2%HA composite at high magnification as shown in Figure 3-13. The white nano-sized particles could be interpreted as being a result of P diffusion due to their small atomic radius which causes a high diffusion of P into the Ti64 matrix during the SLM process.

*Table 3-1: EDS spot analysis of grain boundary (GB) and inside grain domains in in structure of SLM Ti64-2%HA composites.*

| 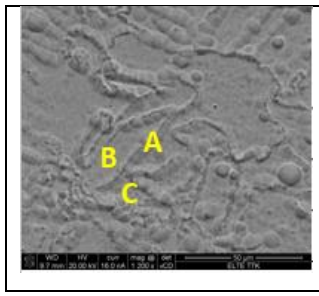 | Analysis points | Element wt% | | | | | |
|---|---|---|---|---|---|---|---|
| | | Ti | Al | V | O | P | Ca |
| | A | 83.61 | 4.36 | 2.58 | 8.36 | 1 | 0.09 |
| | B | 86.28 | 7.75 | 2.57 | 3.2 | 0.20 | - |
| | C | 85.94 | 7.44 | 2.55 | 3.8 | 0.27 | - |



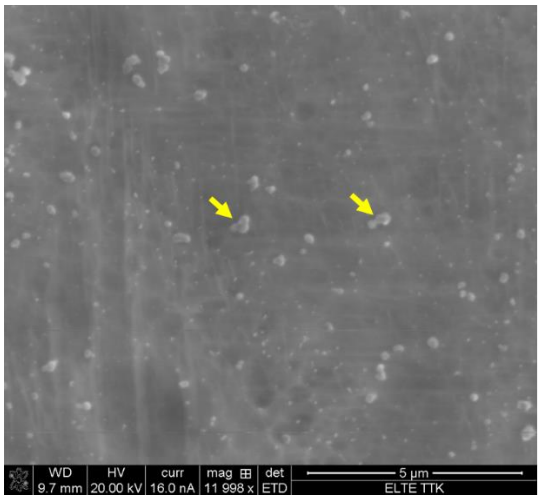


*Figure 3-13: Nanosized particles on the microstructure of the SLM Ti64-2%HA composites.*

To additionally investigate and reveal the phases during SLM of the Ti64-2%HA composite, Vickers microhardness testing was performed. The results are illustrated in Figure 3-14. The average hardness of the Ti64 is ~ 374 HV, which is in good agreement with its predominantly α' martensitic structure. The hardness of the Ti64-2%HA, averaged at 478 HV, is higher than the hardness of the Ti64. This increase in hardness can be explained by the presence of HA at grain boundaries and also by the presence of Ca, P, and O elements due to partial decomposition of HA, which results in the structure strengthening via a solid solution mechanism. Another possible reason for the increase in hardness is the formation of the fine α Ti phase in the Ti64-HA structure. It has been shown that the fine α Ti phase is harder than the α' martensite phase [132, 159]. The heterogeneous hardness profile of Ti64-2%HA compared to that of Ti64 is a result of different phases formed in the structure of the Ti64-2%HA composite. The higher value of the hardness in the region (563 HV) compared to the vicinity zones (470 HV) can be

attributed to the formation of the HA phase. It has been reported that the hardness of the HA phase is about 600HV [46].

Consequently, the microstructure of the SLM of Ti64-2%HA composite is a complex mixture of α Ti, HA, $Ti_3P$, $Ti_xO$, P, and $CaTiO_3$. The average volume fraction of HA in the microstructure of the Ti64-HA is about 10% based on Image J software. The formation of HA has been reported in electron beam melting of Ti-HA composites [153]. It should be noted that the formation of HA and dispersed Ca, P, and O elements in the microstructure of implants may result in higher tendency of good bone osseointegration and biocompatibility.

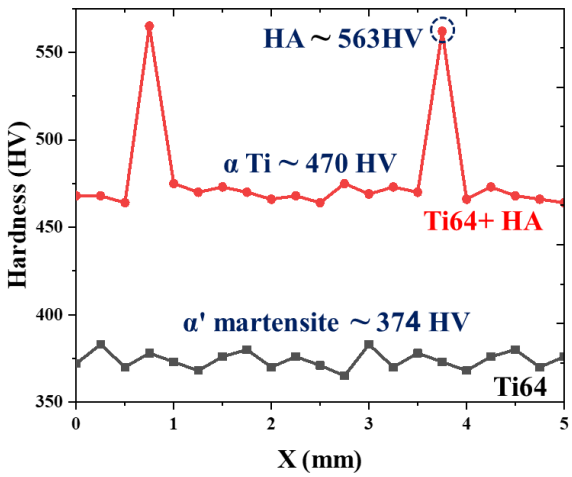


*Figure 3-14: Corresponding microstructures are labelled on Vickers microhardness of the SLM Ti64 and Ti64-2%HA composites.*

### 3.4.3 Mechanical properties

Tensile tests and nanoindentation tests were performed to investigate the mechanical properties of Ti64 and Ti64-2% HA. Figure 3-15 summarizes the results of the tensile tests on the SLM-processed Ti64-2% HA composite and compares them with those of pure Ti64. The experimental results of the tensile test indicate that the addition of HA has a significant effect on the load carrying capacity of selective laser melting. As can be seen, the addition of 2%wt HA lowered yield strength, maximum tensile strength, and elongation of the selective laser melting from 1060, 1180, and 8 to 223, 255 and 0.9, respectively. The deteriorating of tensile properties and improvement of hardness are due to the formation of brittle phases including $Ti_3P$, $CaTiO_3$, and the precipitation of HA in grain boundaries. Nevertheless, the tensile strength of the composite Ti64-2% HA produced by SLM is about 2-3 times higher than that of human bone. It has been

reported that the tensile strength of human bones are between 60 and 130 MPa [103, 160]. Figure 3-16 shows a typical load/nano-indentation depth curves for Ti64 and Ti64-2%HA samples at a peak load of 3.5 mN. The penetration depths of the Ti64 and Ti64-2%HA samples are 580 and 450 nm, respectively. According to Figure 3-16, the hardness of the Ti64-2%HA is higher than the hardness of the Ti64. This is due to the formation of a hard and brittle structure in the Ti64-2%HA sample as compared to the lath microstructure, consisting mainly of α′ martensitic structure in the Ti64 sample.

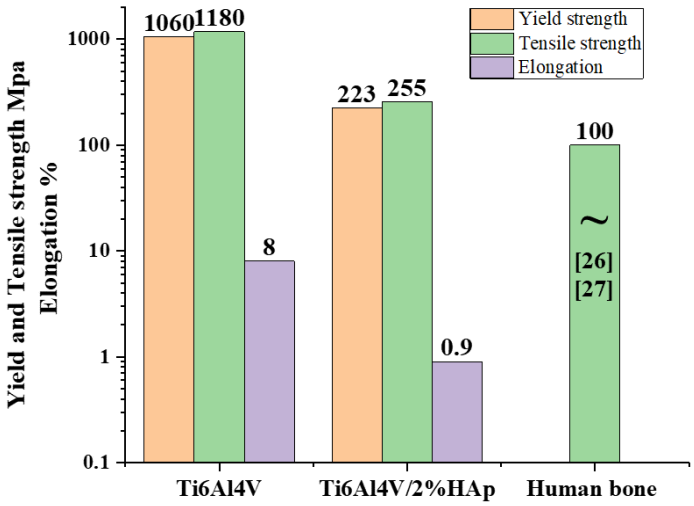


*Figure 3-15: Tensile properties of the SLM Ti64 and Ti64-2%HA composites.*

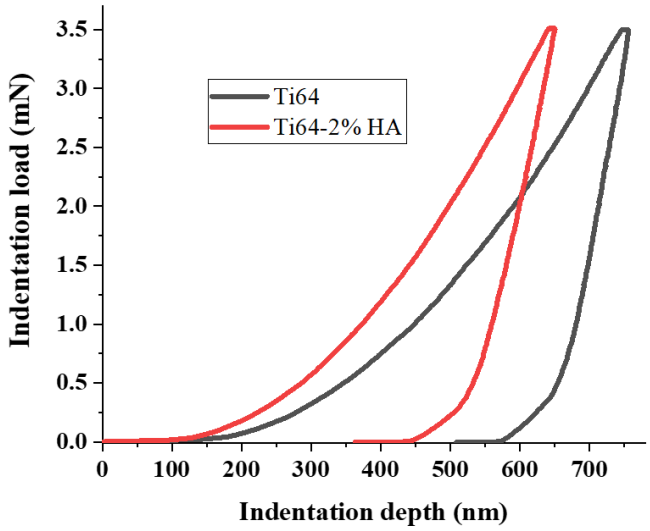


*Figure 3-16: Load/nano-indentation depth curves of the SLM Ti64 and Ti64-2%HA composites.*

## 3.5 Conclusions of the SLM of Ti6Al4V-Hydroxyapatite

1. SLM of Ti64 components exhibit a lath microstructure consisting mainly of an α'-martensitic structure and a small amount of β-titanium (β-Ti) at the grain boundaries.
2. SLM of Ti64-2%HA composite components exhibits small grains of α Ti coupled with dark grain boundaries of HA and some light green regions of $Ti_3P$, and other phases of $Ti_xO$, P, and $CaTiO_3$.
3. The tensile properties of SLM components made of Ti64-2% HA are significantly higher than those of human bone in the literature. Therefore, it is recommended that further research be conducted in the field of SLM of titanium hydroxyapatite with graded composition/structure (functionally graded materials/structures) to mimic natural bone and ensure good interfacial bonding between bone tissue and metal implants.
4. For the same HA amount (2 wt%), a decrease in energy density resulted in lower tensile strength. On the other hand, an increased energy density input has a negative effect on the fabrication behavior, since several explosions (popups) occurred, leading to the collapse of the support structure. Therefore, it can be suggested that a preheating treatment of the HA powder is required to eliminate the effects of this "gas/explosion" problem on the SLM fabricated Ti64 -2% HA.
5. The SLM of Ti64- HA exhibited the lower tensile properties compared to the SLM of Ti64. This was attributed to the formation of very brittle and hard HA in the grain boundary, which promotes the growth of cracks.

# 4 SLM Process on Ti6Al4V Alloy Hybrid Powders with Spherical and Irregular Shapes

## 4.1 Introduction

SLM is a challenging process where a large number of parameters can affect the mechanical performance and microstructure of a finished part [10]. The parameters of the SLM process can be divided into four groups: Laser, Scan, Temperature and Powder, as shown in Figure 1-5. The parameters for the laser and the scan in SLM of Ti64 have been studied by many authors [11, 161–167]. Several studies, for instance [130, 168–170], have been performed on the effects of SLM temperature parameters on the Ti64 alloy. In contrast, few studies have been done to investigate the effect of powder parameters of Ti64 [121, 171]. The qualities of SLM components such as dimensional accuracy, defects, and surface roughness are mainly influenced by flowability, size distribution, shape, composition, and surface morphology of the powder particles [122, 172, 173].

Most previous studies have focused only on the use of plasma atomized powders (spherical particles) with excellent flowability [174] (28 s/50g for plasma atomized 100% spherical Ti64 powder [175, 176]) for powder bed additive manufacturing. To date, there is no accepted definition for the influence of powder properties in the SLM process [173, 177–179]. Therefore, there is a clear practical need to gain a comprehensive understanding of the relationship between powder and final workpiece properties, which requires further advanced research on the various powder parameters (see Figure 4-1).

## 4.2 Objective

The objective of my work was to extend the current knowledge on the relationship between powder and finished part properties. This work is a preliminary attempt to investigate the SLM of hybrid powder of Ti64, which consists of 50 wt% spherically atomized plasma and 50 wt% irregular hydride dehydride (HDH) powder, with acceptable flowability (36.5 s/50g). It is well known that powder flowability (fluidity) is a critical factor in powder bed additive manufacturing [172, 173]. Flowability or fluidity is defined in JIS Z 2502:2012 [180] as the time required for a given mass (50 g) of powder to flow out of a given orifice under given conditions. Figure 4-2 details the method of flowmeter apparatus (Hall Funnel) to calculate the flowability of powder.

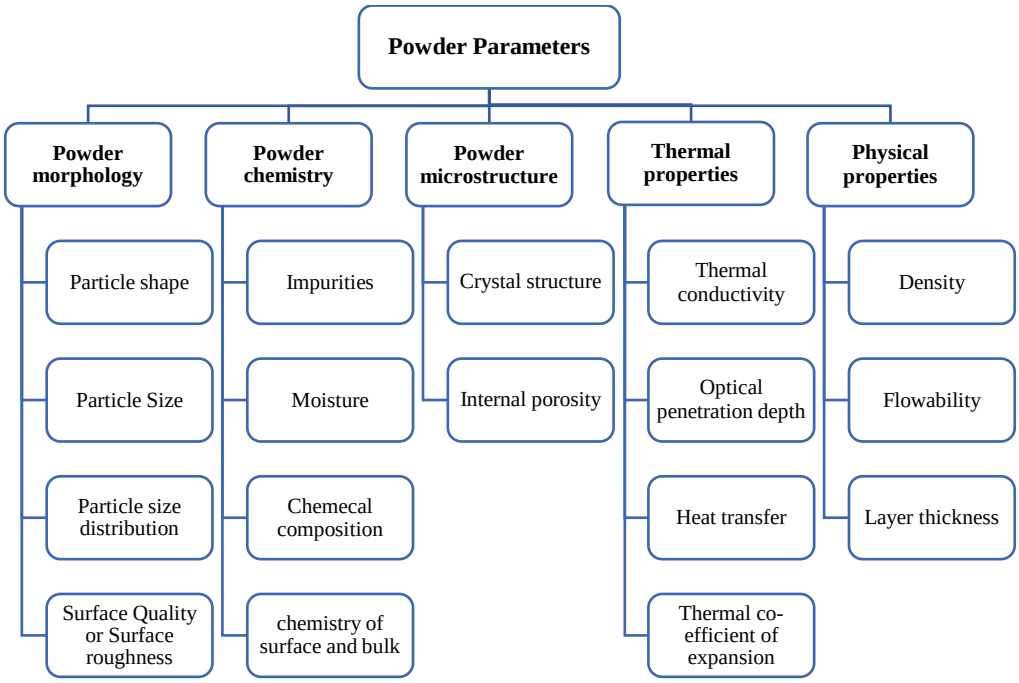


*Figure 4-1: Powder parameters influencing on the properties of SLM manufactured parts.*

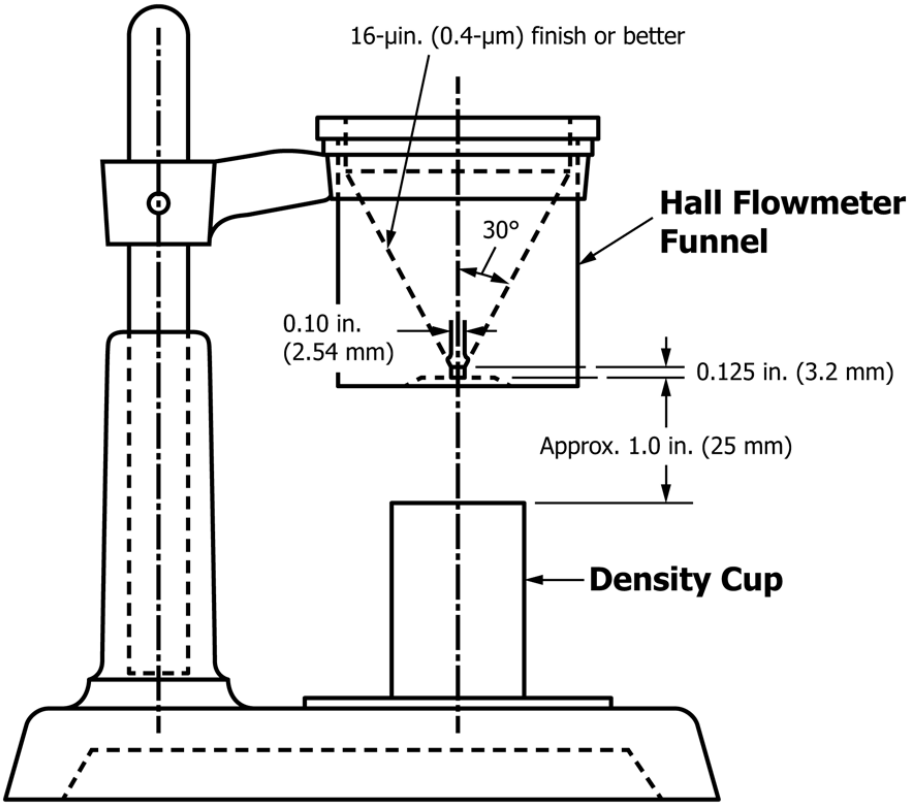


*Figure 4-2: flowmeter apparatus (Hall Funnel) to calculate the flowability of powder [181].*

In addition, one of the main obstacles to the use of spherical titanium powder in powder bed additive manufacturing is that it is often expensive [3, 182] (200-450 $/kg[183]). Irregularly shaped HDH powder is a lower cost product than spherical titanium powder [172, 184] (66-176 $/kg[183]). For this reason, much attention has been paid to the fabrication of a low-cost hydride-dehydride (HDH) irregularly shaped Ti alloy for powder bed additive manufacturing [185, 186]. Therefore, it is necessary to determine whether the hybrid powder of Ti64 can be printed without affecting the microstructural and mechanical properties of the components fabricated by the SLM system.

## 4.3 Experimental work

A hybrid powder (see Figure 4-3) consisting of 50% spherical plasma- atomized (PA) and 50% irregularly shaped hydride-dehydride-based (HDH) Ti64 alloy (provided by TOHO Titanium company/Japan) was used as the base material. The size distribution of the hybrid powder is in the range of 45-150 µm. The chemical compositions and ASTM specification (ASTM B348 Gr.5) of the Ti64 hybrid powder are given in Table 4-1. As detailed in Figure 4-4, the value of flowability of (50% PA+50%HDH) powder is 36.5 s/50g according to JIS Z 2502:2012 [175, 176]. An additional Ti64 (Gr.23) plasma atomized spherical powder (provided by LPW Technology/UK), as demonstrated in Figure 4-5, was used as a reference powder to facilitate discussion of tensile properties. The chemical composition (wt %) of the reference powder is given in Table 4-1, and the size distribution is in the range of 15-45 µm.

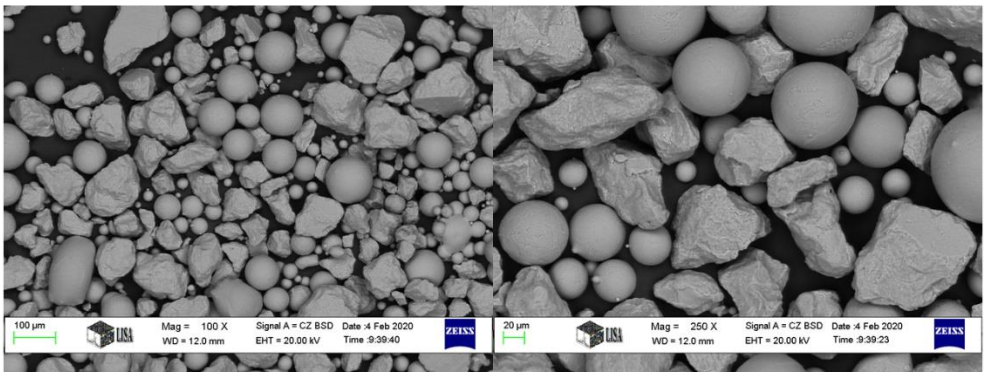


*Figure 4-3: SEM micrograph of Ti64 alloy hybrid powder at two different magnifications.*

*Table 4-1: Chemical analysis of hybrid powder and reference powder.*

| (Mass%) | | Al | V | Fe | O | N | C | H | Ti |
|---|---|---|---|---|---|---|---|---|---|
| Hybrid powder (50%/50%) | | 6.31 | 4.15 | 0.18 | 0.170 | 0.008 | 0.01 | 0.008 | Bal |
| | Max | 6.75 | 4.50 | 0.40 | 0.20 | 0.05 | 0.08 | 0.015 | Bal |

| | | | | | | | | | |
|---|---|---|---|---|---|---|---|---|---|
| ASTM B348 Gr.5 | Min | 5.50 | 3.50 | - | - | - | - | - | - |
| Reference powder (100%) | | 6.11 | 4.02 | 0.17 | 0.090 | 0.023 | 0.01 | 0.003 | Bal |
| ASTM B348 Gr.23 | Max | 6.75 | 4.50 | 0.25 | 0.13 | 0.03 | 0.03 | 0.012 | Bal |
| | Min | 5.50 | 3.50 | - | - | - | - | - | - |

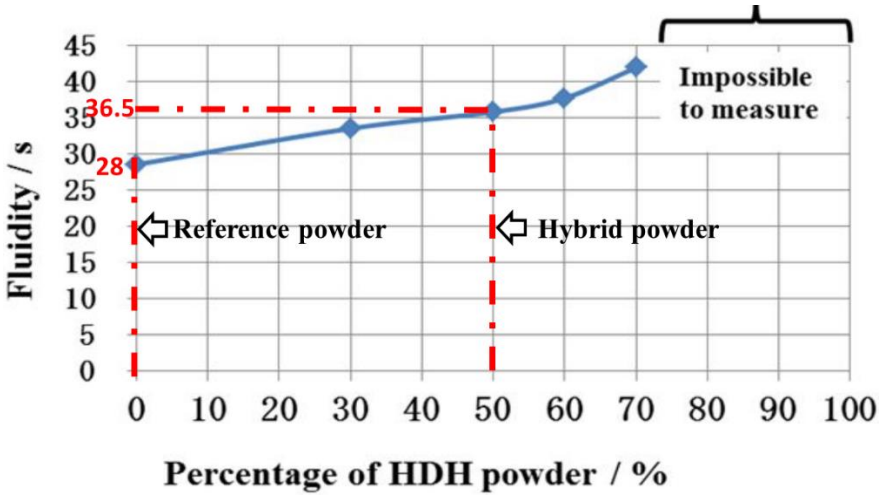


*Figure 4-4: Flowability (fluidity) of (50% PA+50%HDH) hybrid Ti64 powder and (100% PA) reference powder* [175].

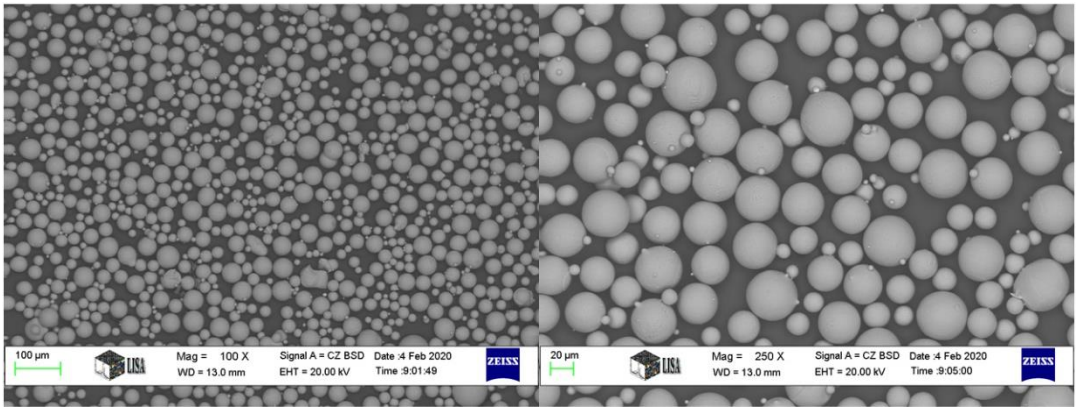


*Figure 4-5: SEM micrograph of Ti64 alloy reference powder at two different magnifications.*

Ti64 samples were manufactured using commercial SLM equipment (Sisma mysint 100) fitted with a fiber laser 200 W with a laser spot of 55 µm. Laser power, scanning speed, and layer thickness were kept constant (optimum conditions) at 125 W, 1000 mm/s, and 20 µm, respectively. Pure argon gas with a flow rate of 35 L/min was used for shielding. The samples of the tensile test were prepared with dimensions of 60 mm in length, 10 mm in width and 2 mm in thickness. Tensile tests were carried out at a cross head of 1 mm/min. Each tensile testing was

collected from an average of three experiments. The purpose of the tensile test was to evaluate the mechanical properties of manufactured samples in terms of yielding strength, ultimate tensile strength, and total elongation. Metallurgical characteristics of the SLM-fabricated Ti64 parts were examined using X-ray diffraction, optical microscopy, and scanning electron microscopy. All metallographic sample examinations were prepared following the standard metallography procedure for titanium alloys. Keller's No. 193 etching reagent [134] was used to reveal the microstructure of the samples.

## 4.4 Results and Discussion

### 4.4.1 Formation of defects in building sample

SLM building sample defects made while using hybrid and reference Ti64 powders were determined by examination of the cross-sectional surfaces. Two types of defects (Figure 4-6 A) were observed during the SEM test in the samples made using the hybrid powder. These included gas porosity, which is accompanied by a spherical or elliptic shape, and lack of fusion voids, which is accompanied by an irregular shape with sharp tips. In contrast, only gas porosity (Figure 4-6 B) was observed in the samples made using the reference powder.

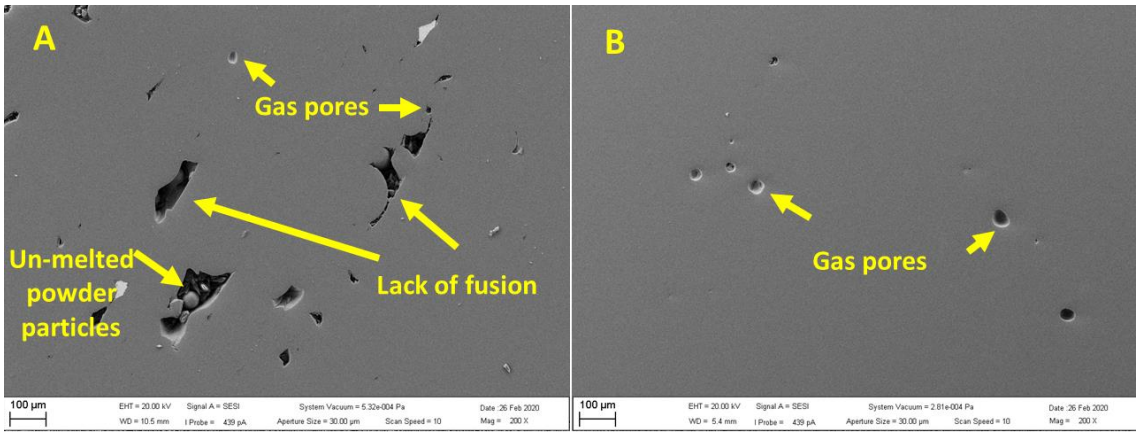


*Figure 4-6: Gas porosity and lack of fusion defects during SLM of A) hybrid powder and B) reference powder.*

*Gas porosity*: In the SLM process, gas pores are formed from trapped inert gas in the molten pool not insoluble in liquid metals which resulted in a void in the solidified pool. There are two sources for gas porosity formation in the SLM building sample: the inert shielding gas such as He and Ar entrapped between the powder particles and gas entrapped inside the powder fabricated via gas atomization [122]. A good way to avoid the use of He and Ar is to use $N_2$ (non-inert shielding gas) instead. Elmer et al.[187] in their work on the effect of $N_2$ and Ar on

porosity formation in laser welds found that porosity formation can be reduced or eliminated in stainless steel welds by using $N_2$ instead of Ar. It is common knowledge that $N_2$ dissolves before solidifying the liquid melt pool. Unfortunately, this can't be used in Ti alloys due to the fact that Ti is highly reactive and sensitive to nitrogen in the liquid state or when heated in air at temperatures above 650 °C [48].

*Lack of fusion voids*: Lack of fusion voids are evident in the cross-sectional surfaces, which result from insufficient laser energy per unit volume, which can cause inadequate penetration. Figure 4-7 highlights severe defects of the SLM building sample made by using the hybrid Ti64 powder, whereas parts fabricated using the reference powder achieve near full density under the same processing parameters as detailed in Figure 4-6. It is well known that increasing laser energy with sufficient penetration by altering the parameters of the SLM process decreases lack of fusion voids. Nesma et al.[10] showed that increasing scan speed increases the formation of voids; on the other hand, Bauereiß et al. [188] found that increasing laser power decreases the formation of voids. The hot isostatic pressed (HIP) approach has been put forward to solve this issue [189–191].

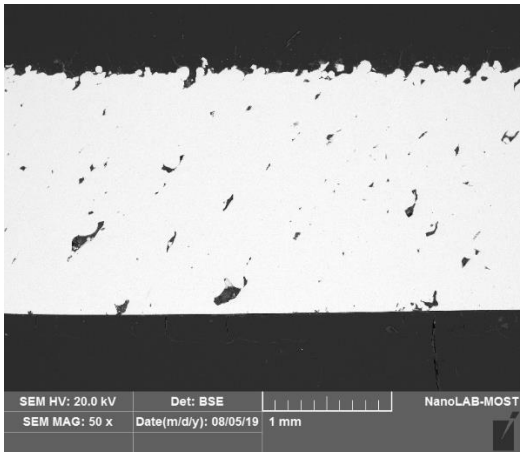


*Figure 4-7: Macrographs of fabricated samples by using the hybrid powder in as-polished condition.*

In contrast with applying 100% spherical powder which leads to high density of fabricated parts (Figure 4-8), we believe that applying the hybrid powder with its different shape and flowability could leave gaps (or cavities) between such particles which leads to the existence of pores on the final products as highlighted in Figure 4-9 (a-b). In my view, several new techniques can be suggested and will assist researchers in overcoming this problem, including:

- Reducing the hybrid Ti64 powder sizes to a range of 20 to 60 µm,

- The lack of fusion voids can be reduced by decreasing the amount (ratio) of HDH irregular from 50% to 25% or 15% wt.,
- Using the double scanned or re-melted strategy in order to solve this problem, as highlighted in Figure 4-9 (a-c).

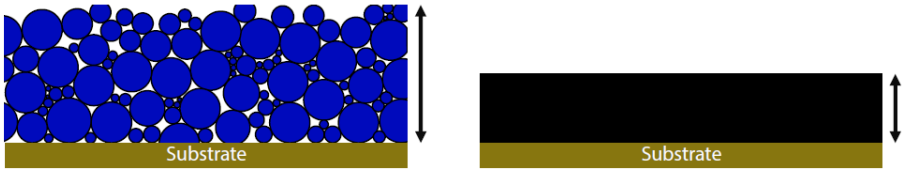


*Figure 4-8: Applying 100% spherical powder.*

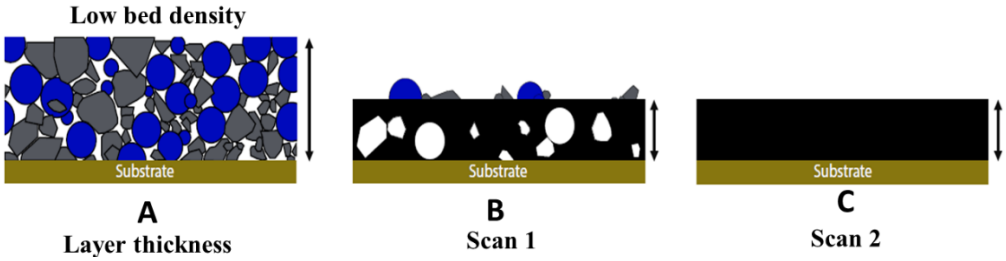


*Figure 4-9: Applying hybrid powder with different shape and size.*

### 4.4.2 Mechanical performance

The mechanical performance of SLM building samples is generally considered under tensile loading conditions [112, 161]. Mechanical performance of the SLM-fabricated Ti64 parts was described in terms of yielding strength ($\sigma_{0.2}$), ultimate tensile strength, and total elongation to failure. As highlighted from Figure 4-10, there is a significant difference in tensile properties between the SLM-fabricated Ti64 parts with 100% spherical powder and SLM-fabricated Ti64 parts with hybrid powder. The average yielding strength, tensile strength, and total elongation of the Ti64 parts manufactured using hybrid powder were 21%, 17%, and 31% lower than that of the Ti64 parts manufactured using 100 wt% spherical powder respectively. These results could be correlated to sharp tips of lack of fusion voids which are susceptible to focused local stress, leading to premature failure under loading conditions, especially static / quasi-static tensile [192]. The lack of fusion voids have strongly affected the mechanical performance of 3D manufactured products during the tensile test when compared to the gas porosity [193].

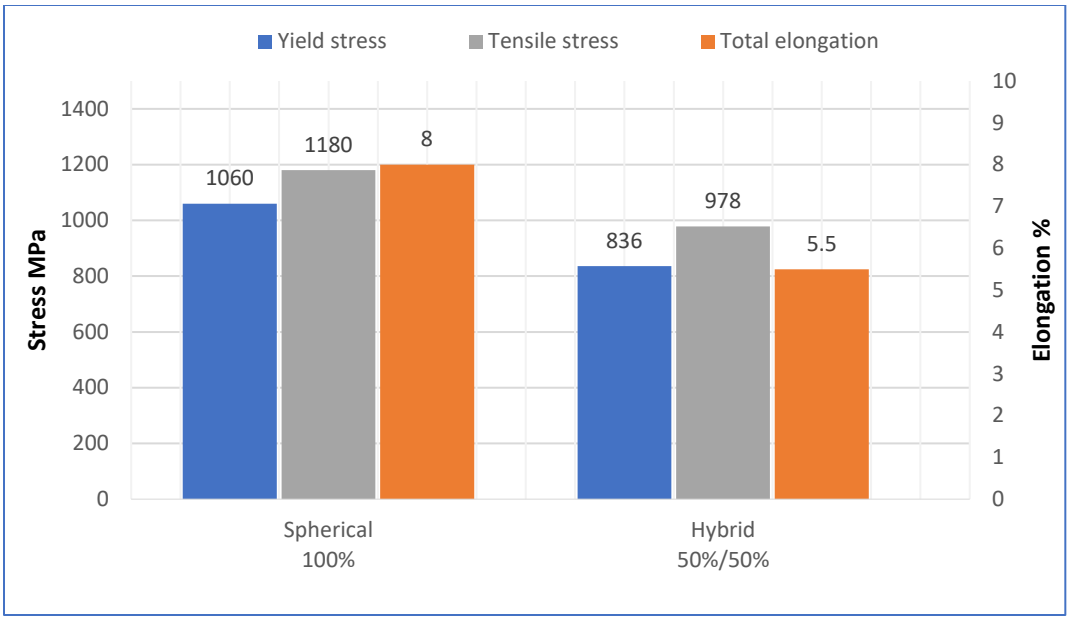


*Figure 4-10: Yielding strength, tensile strength, and total elongation of Ti64 parts manufactured using hybrid powder and spherical powder.*

### 4.4.3 Metallurgical characteristic

The metallurgical characteristics of Ti64 alloys are recognized as being the most important factor which affects their mechanical properties. It is common knowledge that Ti64 alloy microstructure evolution is controlled by a solidification reaction and solid-state phase transformation. The microstructural evolution of the Ti64 alloy during SLM is more complicated than that of the conventional manufacturing process due to a large number of SLM parameters that can affect the cooling rate and reheating. Figure 4-11 shows a schematic representation of the effect of temperature history on the microstructure of a single layer of the Ti64 alloy in the last 7 layers [1]. It can be seen in Figure 4-11 that each layer was subjected to two liquid solid transformation, one L+β / solid transformation, one β transformation, and two alpha-beta transformations. This figure largely depends on the SLM parameters mainly laser power, scan speed and layer thickness.

The SLM process involves a complex interaction between the metallurgical and physical characteristics of the printed material and the process phenomena. Figure 4-12 (a and b) shows an X-ray diffraction (XRD) pattern and a typical microstructure of a Ti64 part manufactured by SLM. The XRD analysis reveals a dual phase crystalline structure of hexagonal close packed (hcp) and body center cube (bcc).

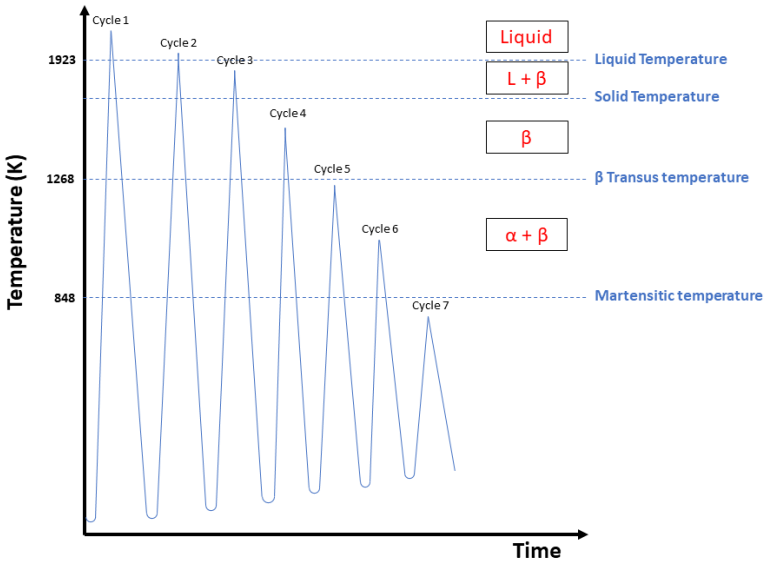


*Figure 4-11: Schematic representation of thermal cycles that can occur during SLM.*

The presence of the hcp structure is due to the formation of alpha prime (α′) martensite or alpha (α) phase, or the intermetallic aluminide phase ($Ti_3Al$). As is well known, in Ti alloys, the structure of α′, α, and $Ti_3Al$ is hcp; therefore, it is difficult to distinguish between each other with regard to XRD analysis. The difference in the metallurgical content between α′ and α phases of Ti64 alloy is related to the vanadium (V) content in the atomic structure. The V content in α′ phase is higher than α phase resulting in the formation of a higher deformation of the crystal structure of α′ phase[120].

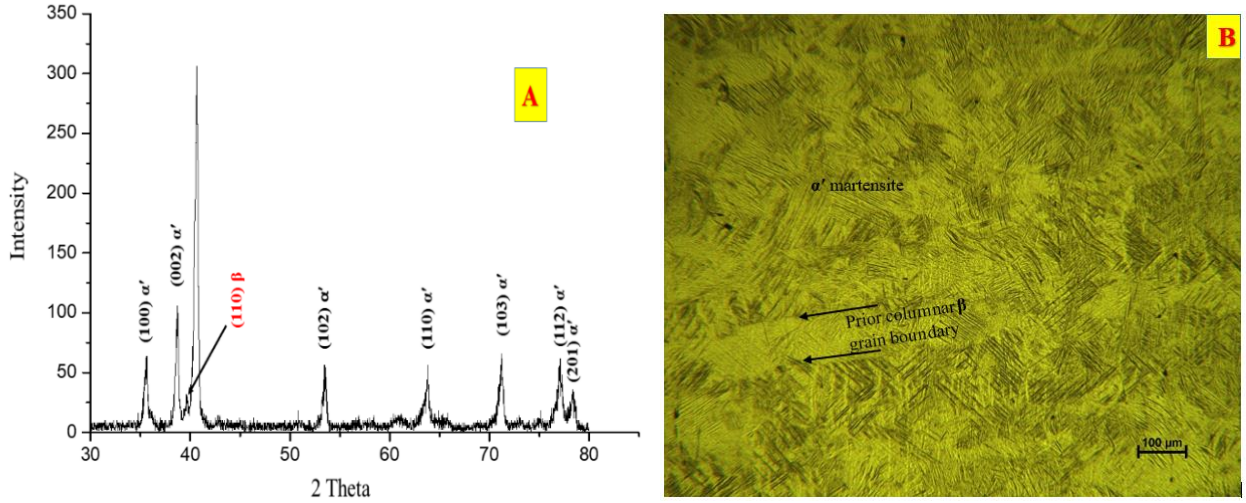


*Figure 4-12: a) X-ray diffraction patterns of fabricated Ti-6Al-4V sample and b) SEM micrograph showing fabricated Ti64 microstructure.*

The effect of the cooling rate on the final microstructure of the Ti64 alloy during the solidification process has been comprehensively studied [31]. It has been shown that at high cooling rates of more than 410 °C $s^{-1}$, beta phase transforms into a fully alpha prime (α′) martensite. Moreover, the optimum cooling rate of SLM has been reported in the range of $10^4$ – $10^6$ K $s^{-1}$ [1, 108, 109]. Additionally, peak temperature has been noted between 1900 and 2700 ºC in the molten pool of Ti64 during SLM [194]. Therefore, alpha prime (α′) martensite formation in SLM of Ti64 is highlighted because the cooling rate in SLM is higher than 410 ºC/s. Several researchers [110–112] have shown that Ti64's SLM microstructure is completely (α′) martensitic.

It is fundamental to note that a serious matter during Ti64 printing by SLM is probable that ($Ti_3Al$) may have precipitated in grain boundaries, which can dramatically reduce fracture toughness of the manufactured parts [195, 196]. It is well known that $Ti_3Al$ is a typically hard and brittle phase, which leads to brittle fractures. Sun et al. [195] investigated the formation of $Ti_3Al$ via an XRD test. They reported that the planes at (100), (101), and (110) are related to $Ti_3Al$. They also reported that the formation of $Ti_3Al$ due to the extremely high cooling rates in SLM and much higher values for Al content than the content of the supersaturated solid solution, which leads to precipitate of $Ti_3Al$ in the grain boundary. In addition, the solubility of Al in Ti is greatly reduced during the solidification of the molten pool [197]. Thijs et al.[196] noted that the presence of dark bands in the optical micrograph of the Ti64 microstructure manufactured by a SLM system. They found that the primary cause of the present dark bands was due to the precipitation of $Ti_3Al$ on the basis of the EDX measurement. This study has not confirmed previous research on the precipitation of $Ti_3Al$. This is due to uniform Al concentration in the EDX measurement along the line 300 µm, as shown in Figure 4-13. Furthermore, the calculation of lattice parameter (a) not confirmed the formation of $Ti_3Al$, it was found that the average score for (a) of my XRD results = 2.9366 Å, which is in complete agreement with those of α′ martensite [164], whereas lattice parameter of (a) for $Ti_3Al$ is 5.751 Å [198].

The presence of the bcc structure is related to the β phase due to several possible reasons: Firstly, the pores are usually filled with unmelted Ti64 powder particles during the SLM process, as shown in Figure 4-6 a. As is well known, the microstructure of unmelted Ti64 powder consists of β+α phases. The lower intensity of the XRD peak of β phases in the 2θ = 39.8 compared to the intensity of the α′ may be due to the low volume fraction. It has been found that the volume

fraction of β phase accounted for approximately 5% of fabricated SLM Ti64 structure [159]. Secondly, the β phase in temperatures above beta transus could have been solidified rapidly under a fast cooling rate and the solid solution atoms (V) did not have sufficient time to spread from unit cells, therefore, transformation into α phase is difficult [195, 199].

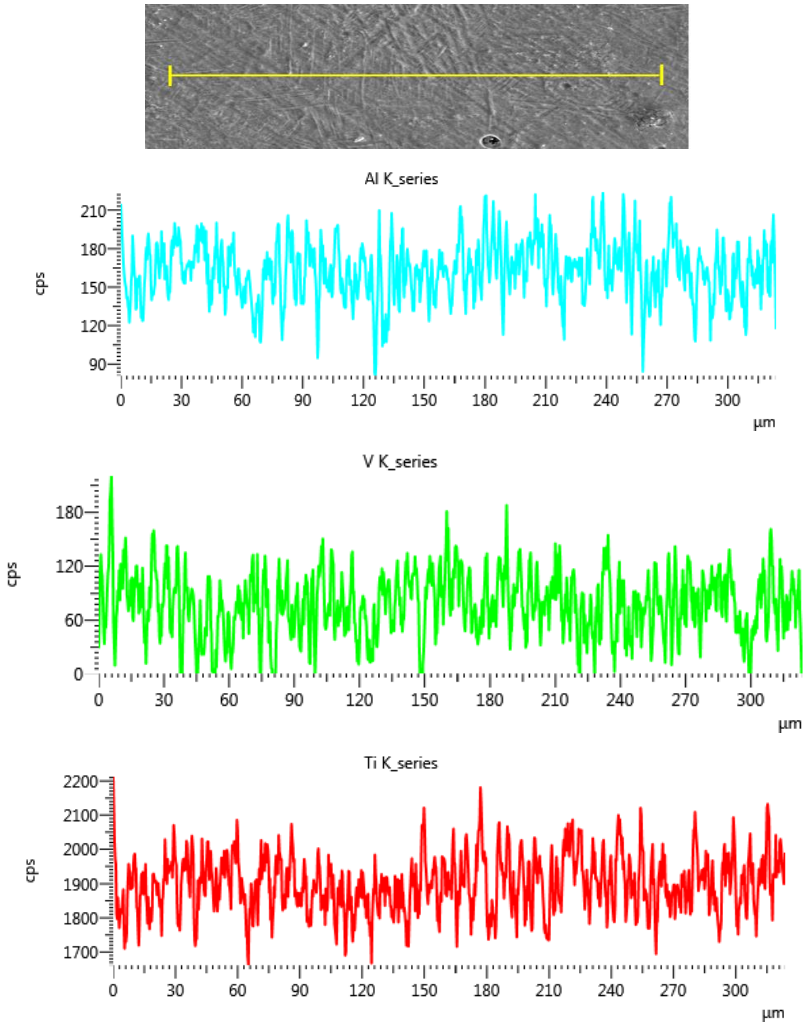


Figure 4-13: X-ray line scan (EDX) in the manufactured parts, not indicating the formation of (Ti3Al) in grain boundaries.

## 4.5 Conclusion

1- The results of this investigation show that a decrease in powder flowability (36.5 s) results in an increase in susceptibility to the formation of lack of fusion defects with dropped tensile properties.

2- The findings of this study add substantially to our understanding of SLM and indicate that hybrid powder (50/50) wt% of Ti64 with larger powder particles are less desirable in SLM system.

3- The Ti64 fabricated part's microstructure features alpha prime (α′) martensite- prior β grain boundaries which is in contrast to the α′, β, and $Ti_3Al$ microstructure predicted by the Sun et al. and Thijs et al.

# 5 Summary of New Scientific Results

The dissertation findings are summarized in seven thesis points. In square brackets are the author's works in which the actual thesis points were published.

**Thesis 1 [Publications: J1]**: I have found that the structure of Ti64 manufactured by SLM has two different martensite variants, namely the HCP martensite of the **α′**-phase and the orthorhombic martensite of the **α′′**-phase. I also found that the martensitic **α′** microstructure of as-manufactured Ti64 is characterized by a hierarchical structure composed of four different types of **α′** based on dimensions: primary (L = 125 µm), secondary (64 µm), tertiary (32 µm), and quaternary (8 µm). The parameters of the SLM process were laser power = 125 W, scanning speed = 1000 m/s, and layer thickness = 20 µm.

**Thesis 2 [Publications: J1]**: I have proved that **solution treatment** at 1020 °C and 850 °C has a slight effect on elongation improvement. After solution treatment at 1020 °C, the elongation increased from 8% (as-printed) to 8.6%, and the tensile strength decreased from 1180 MPa (as-printed) to 990 MPa due to the formation of **α**, **α′**, and **α′′**. After solution treatment at 850 °C, the elongation increased from 8% (as-printed) to 10.4%, and the tensile strength decreased from 1180 MPa (as-printed) to 930 MPa due to the formation of **α**, **β**, and **α′′**.

**Thesis 3 [Publications: J1, C1]**: I have underlined that the SLM-manufactured Ti64 parts with an **annealing treatment** at 1020 °C followed by cooling in the furnace had higher elongation but significantly reduced strength. The elongation increased from 8% (as-printed) to 14.5 %, and the tensile strength decreased from 1180 MPa (as-printed) to 833 MPa due to the formation of an **α** and **β** lamellar structure.

**Thesis 4 [Publications: J1]**: I have highlighted that **ageing at 550 ºC for 3 hours** followed by cooling in the furnace after solution heat treatment at 850 ºC and 1020 ºC had a negative effect on elongation improvement. After HT850WC + AG (heat treatment at 850 ºC followed by water cooling and ageing), the elongation decreased from 10.4% to 9.3%, and the tensile strength increased from 930 MPa to 970 MPa due to the partial dissolution of soft **α′′** and its transformation into **α**, **β**, and **α′′**. After HT1020WC + AG (heat treatment at 1020 ºC followed by water cooling and ageing), the elongation decreased from 8.6% to 7.2%, and the tensile strength

increased from 990 MPa to1035 MPa due to the fragmentation and globalization of longer, elongated α-grains.

**Thesis 5 [Publications: J1, C1]**: I have demonstrated that the microstructure of HT1020FC (heat treatment at 1020 ºC followed by furnace cooling) is characterized by the formation of an α + β lamellar structure. In contrast, the microstructure of HT1020WC (heat treatment at 1020 ºC followed by water cooling) is characterized by the formation of semi-equiaxial β grains with a diameter of average 170 µm with longer elongated α grains and basket-weave **α′**. I also demonstrated that the β phase undergoes more complicated microstructural transformations during solidification after HT1020WC, such as the formation of the **α′** phase by the displacing transformation with a shear mechanism and the formation of the semi-equiaxed β grains morphology by a nucleation process.

**Thesis 6 [Publication: J2 and J3]**: I have reported the characterization and mechanical properties of a novel Ti6Al4V/2% Hydroxyapatite metal/bio-ceramic composite fabricated using the additive SLM manufacturing process. According to XRD, SEM, EDX (point, line, and maps), OM, and hardness tests, I have revealed that the SLM components made from Ti64-2% HA have small grains of α Ti associated with dark grain boundaries of HA and some light green regions of $Ti_3P$ and other phases of $Ti_xO$, P and $CaTiO_3$. I have showed that the behavior of HA during SLM of Ti64/2%HA goes through two paths: Decomposition and Stability. Part of HA decomposes and interacts with the Ti, which is transformed into $Ti_3P$, $Ti_xO$, P, and $CaTiO_3$ phases. Other HA was stable, and no decomposition occurred. The average volume fraction of HA in the microstructure of Ti64- HA was about 10%.

**Thesis 7 [Publication: J3]**: I have highlighted that the composite SLM Ti64-2% HA has a heterogeneous hardness profile compared to Ti64, which is due to the formation of different phases in the structure of the composite SLM Ti64-2% HA. The peak microhardness (~ 563 HV) compared to the ambient zones (~ 470 HV) is due to the formation of the phase HA. I have also highlighted that the composite Ti64-2% HA has a higher microhardness (~ 478 HV) than the pure Ti64 (~ 374 HV), which is due to the presence of HA at the grain boundaries and the presence of Ca, P and O elements as a result of the partial decomposition of HA.

# 6 List of Publications

## 6.1 Articles in internationally reviewed academic journals

**J1** **Hassanen J.**; Kónya, J.; Kulcsár, K.; Kovács, T. Effects of Annealing and Solution Treatments on the Microstructure and Mechanical Properties of Ti6Al4V Manufactured by Selective Laser Melting. Materials, 15, 1978, (**2022**). (WoS, Scopus IF = 4.7, Q1) https://doi.org/10.3390/ma15051978

**J2** **Hassanen J.**; Kónya, J.; Anna Kovács, T. Selective Laser Melting of Ti6Al4V-2%Hydroxyapatite Composites: Manufacturing Behavior and Microstructure Evolution. Metals, 11, 1295, (**2021**). (WoS, Scopus IF = 3.8, Q1) https://doi.org/10.3390/met11081295

**J3** **Hassanen J**, Tunde K. Selective laser melting of Ti alloys and hydroxyapatite for tissue engineering: progress and challenges. *Materials Research Express*. Vol 6 No 8:082003. (**2019**). (WoS, Scopus IF = 4.2, Q1) https://doi.org/10.1088/2053-1591/ab1dee

**J4** **Hassanen J**, Tunde Kovacs & Kónya János. Investigating the impact of a selective laser melting process on Ti6Al4V alloy hybrid powders with spherical and irregular shapes, *Advances in Materials and Processing Technologies*, (**2020**). https://doi.org/10.1080/2374068X.2020.1829960 (WoS, Scopus IF = 3.4, Q2)

**J5** **Hassanen J**, Tunde K. Preparation and Synthesis of Hydroxyapatite Bio-Ceramic from Bovine bone by Thermal Treatment. *Építôanyag: Journal of Silicate Based and Composite Materials*. Vol 71 No 3. Pp. 98-101 (**2019**). (WoS IF=0.3, Q4) https://doi.org/10.14382/epitoanyag-jsbcm.2019.18

## 6.2 Papers at international scientific conferences

**C1** **Hassanen J**.; Kónya, J.; Kulcsár, K.; Kovács, T. The effect of annealing temperature on the microstructure and tensile properties of Ti6Al4V parts produced by selective laser melting. 6TH International Conference on Competitive Materials and Technology Processes, Miskolc. Accepted

**C2** **Hassanen J**, Tunde K. Development of Selective Laser Melting of Ti6Al4V Alloy for Tissue Engineering: Review. Bánki Közlemények. Vol 3 No 1. Pp. 19-23. (**2020**). http://bk.bgk.uni-obuda.hu/index.php/BK/article/view/113/115

## 6.3 Publications in other scientific fields

1. **Hassanen J**, Kovacs, T. (**2018**). Dissimilar Resistance Spot Welding of Ferrite-Martensite Dual Phase Steel/Low Carbon Steel: Phase Transformations and Mechanical Properties. In: Jármai, K., Bolló, B. (eds) Vehicle and Automotive Engineering 2. VAE 2018. Lecture Notes in Mechanical Engineering. Springer. (Scopus, Chapter) https://doi.org/10.1007/978-3-319-75677-6_60
2. Márton Schramkó, Zoltán Nyikes, **Hassanen Jaber**, Tünde Anna Kovács. (**2022**). Dissimilar Joining by Ultrasonic Welding. Journal of Hunan University Natural Sciences. https://doi.org/10.55463/issn.1674-2974.49.3.20 (Scopus IF = 0.9, Q3)
3. **Hassanen J**, Kovacs, T. (**2019**). The effect of nano-quenching media on the tensile properties and microstructure of medium carbon steel. European Journal of Materials Science and Engineering. Volume 4, Issue 1. https://doi.org/10.36868/ejmse.2019.04.02.092
4. **Hassanen J**, Kovacs, T. (**2018**). Similar and Dissimilar Resistance Spot Welds of DP600 and X8Cr17 steels sheets: Welding Current and Fracture Toughness. Bánki Közlemények. Vol 1, No 1. http://bk.bgk.uni-obuda.hu/index.php/BK/article/view/35

# 7 Future studies

This dissertation mainly focuses on the progress and challenges in SLM of Ti6Al4V and SLM of Titanium-Hydroxyapatite. The first challenge, which is the focus of this dissertation, is related to the characterization and mechanical properties of a novel Ti6Al4V/ Hydroxyapatite composite fabricated using the additive SLM manufacturing process for biomedical applications, which aims to improve the osseointegration between metallic implants and the hard tissue of the human body. The second challenge is to improve the mechanical performance of Ti6Al4V alloys manufactured by selective laser melting (SLM), especially ductility, by applying annealing and solution treatments as post-heat treatments. The third challenge is to reduce costs by using hybrid powders of Ti6Al4V alloy with spherical and irregular shapes. However, several aspects need to be further investigated and include:

- SLM of Titanium Zirconium (TiZr) Alloys such as Ti-13Nb-13Zr.
- Fabrication of a novel implant of functionally graded materials and structures (FGM/S) with porosity and chemical composition of Ti and HA by SLM process. By designing FGM/S implants in which 100% Ti alloys form the core of the implants, followed by different ratios of Ti- HA and 100% HA the surface of the implants and the structure of the implants, which contain different size and density of porosity to eliminate the mismatch of the elastic modulus between bone and metallic implant.
- Effect of double-scanning or remelting strategy of SLM process on the Microstructure and Mechanical Properties of Ti6Al4V alloy hybrid powders with spherical and irregular shapes.
- Effect of quenching-aging treatment on as-fabricated Ti6Al4V samples by SLM.

# Figures

Figure 1-1: Classification of AM technologies. ..... 1
Figure 1-2: Powder bed fusion (PBF)process flow [4]. ..... 1
Figure 1-3:Concept of SLM process [7]. ..... 2
Figure 1-4: The experimental setup of Selective Laser Melting (SLM) [8]. ..... 2
Figure 1-5: Parameters in SLM process[10]. ..... 3
Figure 1-6: Schematic diagram of SLM process parameters: laser power, scanning speed, hatch spacing, and layer thickness [11]. ..... 3
*Figure 1-7: Biomedical parts: (a) and (b) Dental prosthesis manufactured by SLM* [12], *(c) 3-unit dental bridge manufactured by SLM* [13], *and (d) Hip stems manufactured by EBM* [13]. ... 4
*Figure 1-8: Automotive parts manufactured by SLM technology* [13]*: (a) Oil pump housing, (b) Exhaust manifold, and (c) Water pump for a motorsport's car.* ..... 4
Figure 1-9: Aerospace parts manufactured by SLM technology: (a) Flight crew rest compartment bracket [14], (b) Engine housing [13], and (c) Turbine blade with internal cooling channels[13]. 4
Figure 1-10: Lack of fusion during SLM process. ..... 6
Figure 1-11: Classification of alloying elements in titanium alloys. ..... 8
Figure 1-12: Characteristics of the Beta → Alpha + Beta Transformation. ..... 9
Figure 1-13: : Healthy bone and femoral implant after applying stress [62]. ..... 12
Figure 1-14: Functionally graded materials and structures (FGM/S) implant with porosity and chemical composition. ..... 16
Figure 1-15: Pseudo-binary β isomorphous phase diagram [107]. ..... 17
Figure 1-16: Equilibrium phase diagram for titanium alloyed with a Beta eutectoid stabilizer [107]. ..... 17
Figure 1-17: SEM micrograph showing the α′ martensite structure of the Ti64 manufactured by SLM. ..... 19
Figure 1-18: SEM micrographs showing microstructure of annealed SLMed Ti64 at (a) 850 and (B) 1020 C, respectively, indicating the transformation of α′ to α+β. ..... 19
Figure 2-1: Typical Equilibrium Phase diagram for Ti64 alloys. ..... 24
Figure 2-2:SEM micrographs show morphology of Ti64 powder at different magnifications (250x and 1000x). ..... 24
Figure 2-3: The shape and size of the tensile specimen (mm). ..... 25

Figure 2-4: Schematic representation of heat treatment cycle used in this work. ..... 26
Figure 2-5: The XRD pattern of the as printed Ti64 indexing α′ and α″ phases. ..... 27
Figure 2-6:EBSD phase maps of as printed Ti64 sample indicating the volume fraction of α′ and β phases. ..... 29
Figure 2-7:SEM images of Ti64 produced by SLM showing α′ martensite microstructure and the formation of gas pores. ..... 30
Figure 2-8: EBSD phase maps and grain size of the α′ martensite microstructure. ..... 30
Figure 2-9: An optical micrograph showing hierarchical structure of α′ martensitic microstructure. ..... 30
Figure 2-10: Typical hardness profile of as printed sample and samples subjected to different heat treatments. ..... 31
Figure 2-11: a: An optical micrograph of the top view of as printed Ti64 indicating equiaxed β grains morphologies fully with α′ martensite. b: An optical micrograph of the side view of as printed Ti64 indicating β columnar grains. ..... 32
Figure 2-12: The XRD pattern of the HT850FC sample indexing α, β, and α″ phases. ..... 33
Figure 2-13:SEM micrographs showing microstructure of the HT850FC sample at different magnifications indicating α phase (dark phase) coupled with β phase (lighter phase). ..... 33
Figure 2-14: SEM (BSE) micrograph showing microstructure of the HT850FC sample indicating the slight chemical contrast between the α and β phases. ..... 34
Figure 2-15: SEM micrographs at higher magnifications showing microstructure of the HT850FC sample indicating the formation of β nanosized particles dispersed on the α phase. .. 35
Figure 2-16: The XRD pattern of the HT850WC sample indexing α, β, and α″ phases. ..... 35
Figure 2-17: SEM micrographs showing microstructure of the HT850WC sample at different magnifications indicating the formation of a dual phase microstructure. ..... 36
Figure 2-18: SEM (BSE) micrograph showing microstructure of the HT850WC sample indicating the consid-erable chemical contrast between two phases. ..... 37
Figure 2-19: The line scan EDS results of HT850WC showing some areas are rich in V and some are poor in V. ..... 37
Figure 2-20: The XRD pattern of the HT850WC+AG sample indexing α, β, and α″ phases. ..... 38
Figure 2-21: SEM and optical micrographs showing microstructure of the HT850WC + AG sample at various magnifications. ..... 39

Figure 2-22: Comparison of the structure morphologies similarity for sample HT850FC and sample HT880WC. ..... 40
Figure 2-23: A: The XRD pattern of the HT1020FC sample indexing α and β phases. B: Enlargements of the (200), (112), and (201) peaks from 74° to 80° diffraction angles indicating the formation of subpeaks. ..... 41
Figure 2-24: SEM and optical micrographs showing microstructure of the HT1020FC sample at various magnifications. ..... 42
Figure 2-25: The XRD pattern of the HT1020WC sample indexing α′, α, and α″ phases. ..... 43
Figure 2-26: The XRD pattern of the HT1020WC+AG sample indexing α′, α, β, and α″ phases. ..... 43
Figure 2-27: SEM and optical micrographs showing microstructure of the HT1020WC sample at various magnifications. ..... 44
Figure 2-28: SEM micrograph showing semi-equiaxed β grains morphology of the HT1020WC sample. ..... 45
Figure 2-29: SEM and optical micrographs showing microstructure of the HT1020WC+AG sample at various magnifications. ..... 46
Figure 2-30: SEM micrographs at higher magnifications showing microstructure of the HT1020WC+AG sample indicating the formation of β nanosized particles dispersed on the α phase. ..... 46
Figure 3-1: a: Before the surgery. b: Immediately after the surgery. c: Beginning of the bone resorption. d: Fracture [146]. ..... 50
Figure 3-2: Schematic representation of preparation and manufacturing process. ..... 52
Figure 3-3: Morphology of the powders.: a) SEM micrograph of pure Ti64 powder. b) SEM micrograph Ti64 powder mixed with 2 wt% of HA powder. ..... 52
Figure 3-4: The crash of the support structure during SLM of Ti64-2%HA composite. ..... 54
Figure 3-5: FTIR spectra of HA powder heated at 1000 ºC. ..... 55
Figure 3-6: X-ray diffraction pattern of HA powder heated at 1000 °C. ..... 55
Figure 3-7: a), optical image and b), SEM image showing microstructure of the Ti64 manufactured by SLM. C), optical image and d), SEM image showing microstructure of the Ti64-2%HA composite manufactured by SLM. ..... 56

Figure 3-8: a) the x-ray diffraction of the SLM of Ti64 indexing α' martensitic structure. b) the x-ray diffraction of the SLM of Ti64-2%HA indexing α Ti, HA, $Ti_3P$, $CaTiO_3$, and $Ti_xO$ phases. 58
Figure 3-9: Phase diagram of Ti-P (Titanium-Phosphorus) [154]. ..... 59
Figure 3-10: Phase diagram of Ti-0 (Titanium-Oxygen) [156]. ..... 59
Figure 3-11: EDS mapping analysis of SLM Ti64-2%HA composites. ..... 60
Figure 3-12: EDS line scan across the grain boundaries in structure of SLM Ti64-2%HA composites. ..... 61
Figure 3-13: Nanosized particles on the microstructure of the SLM Ti64-2%HA composites.... 62
Figure 3-14: Corresponding microstructures are labelled on Vickers microhardness of the SLM Ti64 and Ti64-2%HA composites. ..... 63
Figure 3-15: Tensile properties of the SLM Ti64 and Ti64-2%HA composites. ..... 64
Figure 3-16: Load/nano-indentation depth curves of the SLM Ti64 and Ti64-2%HA composites. ..... 64
Figure 4-1: Powder parameters influencing on the properties of SLM manufactured parts. ..... 67
Figure 4-2: flowmeter apparatus (Hall Funnel) to calculate the flowability of powder [181]. .... 67
Figure 4-3: SEM micrograph of Ti64 alloy hybrid powder at two different magnifications. ..... 68
Figure 4-4: Flowability (fluidity) of (50% PA+50%HDH) hybrid Ti64 powder and (100% PA) reference powder [175]. ..... 69
Figure 4-5: SEM micrograph of Ti64 alloy reference powder at two different magnifications... 69
Figure 4-6: Gas porosity and lack of fusion defects during SLM of A) hybrid powder and B) reference powder. ..... 70
Figure 4-7: Macrographs of fabricated samples by using the hybrid powder in as-polished condition. ..... 71
Figure 4-8: Applying 100% spherical powder. ..... 72
Figure 4-9: Applying hybrid powder with different shape and size. ..... 72
Figure 4-10: Yielding strength, tensile strength, and total elongation of Ti64 parts manufactured using hybrid powder and spherical powder. ..... 73
Figure 4-11: Schematic representation of thermal cycles that can occur during SLM. ..... 74
Figure 4-12: a) X-ray diffraction patterns of fabricated Ti-6Al-4V sample and b) SEM micrograph showing fabricated Ti64 microstructure. ..... 74

Figure 4-13: X-ray line scan (EDX) in the manufactured parts, not indicating the formation of (Ti3Al) in grain boundaries. ..... 76

# Tables

Table 1-1: Titanium alloys with the ASTM designations and (UNS) numbers. ..... 9
Table 1-2: Thermal properties of metallic implants. ..... 10
*Table 1-3: Physiochemical, mechanical and biological properties of HA* [46–48]. ..... 11
Table 1-4: Young's modulus of biomedical β- titanium alloys..... 14
Table 2-1: Chemical composition of Ti64 powder and ASTM specification..... 25
Table 2-2: Lattice parameters and FWHM of the main α/α′ and β peaks at 2θ=40.56° and 39.80° respectively of as printed sample and samples subjected to different heat treatments. ..... 28
Table 2-3: Mechanical properties of the of as printed sample and samples subjected to different heat treatments. ..... 48
Table 3-1: EDS spot analysis of grain boundary (GB) and inside grain domains in in structure of SLM Ti64-2%HA composites. ..... 62
Table 4-1: Chemical analysis of hybrid powder and reference powder. ..... 68

# Bibliography


1. Frazier, W. E. (2014). Metal additive manufacturing: A review. *Journal of Materials Engineering and Performance*, *23*(6), 1917–1928. https://doi.org/10.1007/s11665-014-0958-z

2. Kai, C. C., How, W. C., & Yee, Y. W. (2017). *Standards , Quality Control , and Measurement Sciences in 3D PRINTING AND ADDITIVE MANUFACTURING*. (B. Guerin & K. Chan, Eds.). UK, USA: Elsevier Ltd.

3. Dutta, B., & Froes, F. H. (2016). *Additive Manufacturing of Titanium Alloys State of the Art , Challenges , and Opportunities*. Elsevier Inc.

4. Diegel, O. (2014). Additive Manufacturing: An Overview. In *Comprehensive Materials Processing* (Vol. 10, pp. 3–18). Elsevier. https://doi.org/10.1016/B978-0-08-096532-1.01000-1

5. Harun, W. S. W., Kamariah, M. S. I. N., Muhamad, N., Ghani, S. A. C., Ahmad, F., & Mohamed, Z. (2018). A review of powder additive manufacturing processes for metallic biomaterials. *Powder Technology*, *327*(December), 128–151. https://doi.org/10.1016/j.powtec.2017.12.058

6. Fukuda, A., Takemoto, M., Saito, T., Fujibayashi, S., Neo, M., Pattanayak, D. K., … Nakamura, T. (2011). Osteoinduction of porous Ti implants with a channel structure fabricated by selective laser melting. *Acta Biomaterialia*, *7*(5), 2327–2336. https://doi.org/10.1016/j.actbio.2011.01.037

7. Yap, C. Y., Chua, C. K., Dong, Z. L., Liu, Z. H., Zhang, D. Q., Loh, L. E., & Sing, S. L. (2015). Review of selective laser melting: Materials and applications. *Applied Physics Reviews*, *2*(4), 1–22. https://doi.org/10.1063/1.4935926

8. Kusuma, C. (2016). *The effect of laser power and scan speed on melt pool characteristics of pure Titanium and Ti-6Al-4V alloy for selective laser melting*. *Master thesis*. Wright State University.

9. Vandenbroucke, B., & Kruth, J. P. (2007). Selective laser melting of biocompatible metals for rapid manufacturing of medical parts. *Rapid Prototyping Journal*, *13*(4), 196–203.

https://doi.org/10.1108/13552540710776142

10. Aboulkhair, N. T., Everitt, N. M., Ashcroft, I., & Tuck, C. (2014). Reducing porosity in AlSi10Mg parts processed by selective laser melting. *Additive Manufacturing*, *1*, 77–86. https://doi.org/10.1016/j.addma.2014.08.001

11. Shipley, H., Mcdonnell, D., Culleton, M., Coull, R., Lupoi, R., Donnell, G. O., & Trimble, D. (2018). Optimisation of process parameters to address fundamental challenges during selective laser melting of Ti-6Al-4V : A review. *International Journal of Machine Tools and Manufacture*, *128*(January), 1–20. https://doi.org/10.1016/j.ijmachtools.2018.01.003

12. Dent-Art-Technik Ltd. (n.d.). Retrieved from http://dentarttechnik.net/

13. Guo, N., & Leu, M. C. (2013). Additive manufacturing: technology, applications and research needs. *Frontiers of Mechanical Engineering*, *8*(3), 215–243. https://doi.org/10.1007/s11465-013-0248-8

14. Blakey-Milner, B., Gradl, P., Snedden, G., Brooks, M., Pitot, J., Lopez, E., … du Plessis, A. (2021). Metal additive manufacturing in aerospace: A review. *Materials and Design*, *209*, 110008. https://doi.org/10.1016/j.matdes.2021.110008

15. Zhou, X., Liu, X., Zhang, D., Shen, Z., & Liu, W. (2015). Balling phenomena in selective laser melted tungsten. *Journal of Materials Processing Tech.*, *222*, 33–42. https://doi.org/10.1016/j.jmatprotec.2015.02.032

16. Li, R., Liu, J., Shi, Y., Wang, L., & Jiang, W. (2012). Balling behavior of stainless steel and nickel powder during selective laser melting process. *International Journal of Advanced Manufacturing Technology*, *59*(9–12), 1025–1035. https://doi.org/10.1007/s00170-011-3566-1

17. Zhang, L. C., Klemm, D., Eckert, J., Hao, Y. L., & Sercombe, T. B. (2011). Manufacture by selective laser melting and mechanical behavior of a biomedical Ti – 24Nb – 4Zr – 8Sn alloy. *Scripta Materialia*, *65*(1), 21–24. https://doi.org/10.1016/j.scriptamat.2011.03.024

18. Gong, H., Rafi, K., Gu, H., Starr, T., & Stucker, B. (2014). Analysis of defect generation in Ti-6Al-4V parts made using powder bed fusion additive manufacturing processes. *Additive Manufacturing*, *1*, 87–98. https://doi.org/10.1016/j.addma.2014.08.002

19. King, W., Barth, H., Castillo, V., Gallegos, G., Gibbs, J., Hahn, D., … Rubenchik, A. (2014). Observation of keyhole-mode laser melting in laser powder-bed fusion additive manufacturing Wayne. *Journal of Materials Processing Tech.*, *214*(12), 2915–2925. https://doi.org/10.1016/j.jmatprotec.2014.06.005

20. Rai, R., Elmer, J. W., Palmer, T., & DebRoy, T. (2007). Heat transfer and fluid flow during keyhole mode laser welding of tantalum, Ti–6Al–4V, 304L stainless steel and vanadium. *Journal of Physics D: Applied Physics*, *40*(18), 5753–5766. https://doi.org/10.1088/0022-3727/40/18/037

21. Kruth, J. P., Froyen, L., Vaerenbergh, J. Van, Mercelis, P., Rombouts, M., & Lauwers, B. (2004). Selective laser melting of iron-based powder. *Journal of Materials Processing Technology*, *149*, 616–622. https://doi.org/10.1016/j.jmatprotec.2003.11.051

22. Olakanmi, E. O., Cochrane, R. F., & Dalgarno, K. W. (2015). A review on selective laser sintering/melting (SLS/SLM) of aluminium alloy powders: Processing, microstructure, and properties. *JOURNAL OF PROGRESS IN MATERIALS SCIENCE*, *74*, 401–477. https://doi.org/10.1016/j.pmatsci.2015.03.002

23. Attar, H., Calin, M., Zhang, L. C., Scudino, S., & Eckert, J. (2014). Manufacture by selective laser melting and mechanical behavior of commercially pure titanium. *Materials Science and Engineering A*, *593*, 170–177. https://doi.org/10.1016/j.msea.2013.11.038

24. Niinomi, M., Narushima, T., & Nakai, M. (2015). *Advances in Metallic Biomaterials Processing and Applications*. London: Springer Series in Biomaterials Science and Engineering. https://doi.org/10.1007/978-3-662-46842-5

25. Singh, S., Ramakrishna, S., & Singh, R. (2017). Material issues in additive manufacturing : A review. *Journal of Manufacturing Processes*, *25*, 185–200. https://doi.org/10.1016/j.jmapro.2016.11.006

26. Williams, G. L. ·James C. (2003). *Titanium*. *Springer-Verlag Berlin Heidelberg*. Springer-Verlag Berlin Heidelberg. https://doi.org/10.10007/978-3-540-71398-2

27. Kolli, R. P. (2018). A Review of Metastable Beta Titanium Alloys. *metals*, *8*(506), 1–41. https://doi.org/10.3390/met8070506

28. Oshida, Y. (2007). *Bioscience and Bioengineering of Titanium Materials*. Elsevier Ltd.

29. Lütjering, G. (1998). Influence of processing on microstructure and mechanical properties of (α+β) titanium alloys. *Materials Science and Engineering: A*, *243*, 32–45. https://doi.org/10.1016/S0921-5093(97)00778-8

30. Galarraga, H., Warren, R. J., Lados, D. A., Dehoff, R. R., Kirka, M. M., & Nandwana, P. (2017). Effects of heat treatments on microstructure and properties of Ti-6Al-4V ELI alloy fabricated by electron beam melting (EBM). *Materials Science and Engineering A*, *685*, 417–428. https://doi.org/10.1016/j.msea.2017.01.019

31. Ahmed, T., & Rack, H. J. (1998). Phase transformations during cooling in α+β titanium alloys. *Materials Science and Engineering A*, *243*, 206–211. https://doi.org/10.1016/S0921-5093(97)00802-2

32. Peters, M. (2005). *Titanium and Titanium Alloys: Fundamentals and Applications*. (D. C. L. D. M. Peters, Ed.). Wiley-VCH Verlag GmbH & Co. KGaA. https://doi.org/10.1002/3527602119

33. Ankem, S., & Greene, C. A. (1999). Recent developments in microstructure / property relationships of beta titanium alloys. *Materials Science and Engineering A*, *263*, 127–131. https://doi.org/10.1016/S0921-5093(98)01170-8

34. Weiss, I., & Semiatin, S. L. (1998). Thermomechanical processing of beta titanium alloys — an overview. *Materials Science and Engineering: A*, *243*, 46–65. https://doi.org/10.1016/S0921-5093(97)00783-1

35. Boivineau, M., Cagran, C., Doytier, D., Eyraud, V., Nadal, M., Wilthan, B., & Pottlacher, G. (2006). Thermophysical Properties of Solid and Liquid Ti-6Al-4V ( TA6V ) Alloy. *International Journal of Thermophysics*, *27*(2), 507–529. https://doi.org/10.1007/s10765-005-0001-6

36. ASM International. (1998). *Metals Handbook: Heat Treating*. *ASM International* (Vol. 4). USA.

37. Wei, L. C., Ehrlich, L. E., J., M., Montgomery, C., Jonathan, J. B., & Malen, A. (2018). Thermal conductivity of metal powders for powder bed additive manufacturing. *Additive*

*Manufacturing*, *21*, 201–208. https://doi.org/10.1016/j.addma.2018.02.002

38. ASM International. (2001). *Metals Handbook: Composites*. *ASM International* (Vol. 21). USA.

39. ISO 5832-4: Implants for surgery - Metallic materials. (1996). *International Standaed*, *part 4*(CoCrMo), https://www.makeitfrom.com/material-properties/UNS.

40. Henriques, B., Gasik, M., Souza, J. C. M., & Nascimento, R. M. (2014). Mechanical and thermal properties of hot pressed CoCrMo – porcelain composites developed for prosthetic dentistry. *Journal of the Mechanical Behavior of Biomedical Materials*, *30*, 103–110. https://doi.org/10.1016/j.jmbbm.2013.10.023

41. Alcisto, J., Enriquez, A., Garcia, H., Hinkson, S., Steelman, T., Silverman, E., … Es-Said, O. S. (2011). Tensile properties and microstructures of laser-formed Ti-6Al-4V. *Journal of Materials Engineering and Performance*, *20*(2), 203–212. https://doi.org/10.1007/s11665-010-9670-9

42. Sobczak-kupiec, A., Pluta, K., & Malina, D. (2017). Studies on Bone-Derived Calcium Phosphate Materials. *Journal of Renewable Materials*, *5*(3–4), 180–188. https://doi.org/10.7569/JRM.2017.634106

43. Mucalo, M. (2015). *Hydroxyapatite (HAp) for Biomedical Applications*. Elsevier Ltd.

44. Bose, S., & Tarafder, S. (2012). Calcium phosphate ceramic systems in growth factor and drug delivery for bone tissue engineering : A review. *Acta Biomaterialia*, *8*(4), 1401–1421. https://doi.org/10.1016/j.actbio.2011.11.017

45. Akram, M., & Ahmed, R. (2014). Extracting hydroxyapatite and its precursors from natural resources. *Journal of Materials Science*, *49*(4), 1461–1475. https://doi.org/10.1007/s10853-013-7864-x

46. Murugan, R., & Ramakrishna, S. (2005). Development of nanocomposites for bone grafting. *Composites Science and Technology*, *65*, 2385–2406. https://doi.org/10.1016/j.compscitech.2005.07.022

47. Jaber, H. L., Hammood, A. S., & Parvin, N. (2018). Synthesis and characterization of

hydroxyapatite powder from natural Camelus bone. *Journal of the Australian Ceramic Society*, *54*(1), 1–10. https://doi.org/10.1007/s41779-017-0120-0

48. Hassanen, J., & Tunde, K. (2019). Selective laser melting of Ti alloys and hydroxyapatite for tissue engineering: progress and challenges. *Materials Research Express*, *6*(8), 082003. https://doi.org/10.1088/2053-1591/ab1dee

49. Krishna, B. V., Bose, S., & Bandyopadhyay, A. (2007). Low stiffness porous Ti structures for load-bearing implants. *Acta Biomaterialia*, *3*(6), 997–1006. https://doi.org/10.1016/j.actbio.2007.03.008

50. Elias, C. N. (2010). Improving osseointegration of dental implants. *Expert Review of Medical Devices*, *7*(2), 241–256. https://doi.org/10.1586/ERD.09.74

51. España, F. A., Balla, V. K., Bose, S., & Bandyopadhyay, A. (2010). Design and fabrication of CoCrMo alloy based novel structures for load bearing implants using laser engineered net shaping. *Materials Science and Engineering C*, *30*, 50–57. https://doi.org/10.1016/j.msec.2009.08.006

52. Traini, T., Mangano, C., Sammons, R. L., Mangano, F., Macchi, A., & Piattelli, A. (2008). Direct laser metal sintering as a new approach to fabrication of an isoelastic functionally graded material for manufacture of porous titanium dental implants. *dental materials*, *24*(11), 1525–1533. https://doi.org/10.1016/j.dental.2008.03.029

53. Berglundh, T. (2005). Peri-implantitis. *The dental clinics of north america*, *49*, 661–676. https://doi.org/10.1016/j.cden.2005.03.007

54. Parithimarkalaignan, S., & Padmanabhan, T. V. (2013). Osseointegration : An Update. *The Journal of Indian Prosthodontic Society*, *13*(1), 2–6. https://doi.org/10.1007/s13191-013-0252-z

55. Xin, X. Z., Xiang, N., Chen, J., & Wei, B. (2012). In vitro biocompatibility of Co – Cr alloy fabricated by selective laser melting or traditional casting techniques. *Materials Letters*, *88*, 101–103. https://doi.org/10.1016/j.matlet.2012.08.032

56. Murr, L. E. (2017). Additive manufacturing of biomedical devices : an overview. *Materials Technology*, *7857*(November), 1–14.

https://doi.org/10.1080/10667857.2017.1389052

57. Zhao, S., Li, S. J., Hou, W. T., Hao, Y. L., Yang, R., & Misra, R. D. K. (2016). The in fl uence of cell morphology on the compressive fatigue behavior of Ti-6Al-4V meshes fabricated by electron beam melting. *Journal of the Mechanical Behavior of Biomedical Materials*, *59*, 251–264. https://doi.org/10.1016/j.jmbbm.2016.01.034

58. Wang, X., Xu, S., Zhou, S., Xu, W., Leary, M., Choong, P., … Min, Y. (2016). Biomaterials Topological design and additive manufacturing of porous metals for bone scaffolds and orthopaedic implants : A review. *Biomaterials*, *83*, 127–141. https://doi.org/10.1016/j.biomaterials.2016.01.012

59. Kadirgama, K., Harun, W. S. W. W., Tarlochan, F., Samykano, M., Ramasamy, D., Azir, M. Z., & Mehboob, H. (2018). Statistical and optimize of lattice structures with selective laser melting (SLM) of Ti6AL4V material. *International Journal of Advanced Manufacturing Technology*, *97*(1–4), 495–510. https://doi.org/10.1007/s00170-018-1913-1

60. Geetha, M., Singh, A. K., Asokamani, R., & Gogia, A. K. (2009). Ti based biomaterials , the ultimate choice for orthopaedic implants – A review. *Progress in Materials Science*, *54*(3), 397–425. https://doi.org/10.1016/j.pmatsci.2008.06.004

61. Meurechy, N. De, Braem, A., & Biomaterials, M. Y. M. (2017). Biomaterials in temporomandibular joint replacement : current status and future perspectives — a narrative review. *International Journal of Oral & Maxillofacial Surgery*, *47*(4), 5–11. https://doi.org/10.1016/j.ijom.2017.10.001

62. Stress Shielding. (2020). *University of Cambridge*. Retrieved from https://www.doitpoms.ac.uk/tlplib/bones/stem.php

63. Gao, C., Peng, S., Feng, P., & Shuai, C. (2017). Bone biomaterials and interactions with stem cells. *Bone Research*, *5*(October), 1–33. https://doi.org/10.1038/boneres.2017.59

64. They, D., & Stress, I. (2006). New Femoral Designs. *CLINICAL ORTHOPAEDICS AND RELATED RESEARCH*, (453), 64–74. https://doi.org/10.1097/01.blo.0000246541.41951.20

65. Smallman, R. E., & Ngan, A. H. W. (2007). *Physical Metallurgy and Advanced Materials Engineering* (Seventh.). Elsevier Ltd.

66. Torres, Y., Trueba, P., Pavón, J., Montealegre, I., & Rodríguez-ortiz, J. A. (2014). Designing , processing and characterisation of titanium cylinders with graded porosity : An alternative to stress-shielding solutions. *JOURNAL OF MATERIALS&DESIGN*, *63*, 316–324. https://doi.org/10.1016/j.matdes.2014.06.012

67. Hussaini, S., Quran, F. A. Al, Ehrenberg, D., & Weiner, S. (2015). Peri-Implant Strain in an In Vitro Model. *Journal of Oral Implantology*, *41*(5), 532–536. https://doi.org/10.1563/AAID-JOI-D-12-00305

68. Duraccio, D., Mussano, F., & Giulia, M. (2015). Biomaterials for dental implants : current and future trends. *Journal of Materials Science*, *50*(14), 4779–4812. https://doi.org/10.1007/s10853-015-9056-3

69. Bandyopadhyay, A., Espana, F., Balla, V. K., Bose, S., Ohgami, Y., & Davies, N. M. (2010). Influence of porosity on mechanical properties and in vivo response of Ti6Al4V implants. *Acta Biomaterialia*, *6*(4), 1640–1648. https://doi.org/10.1016/j.actbio.2009.11.011

70. Speirs, M., Van Humbeeck, J., Schrooten, J., Luyten, J., & Kruth, J. P. (2013). The effect of pore geometry on the mechanical properties of selective laser melted Ti-13Nb-13Zr scaffolds. *Procedia CIRP*, *5*, 79–82. https://doi.org/10.1016/j.procir.2013.01.016

71. Chen, S. Y., Huang, J. C., Pan, C. T., Lin, C. H., Yang, T. L., Huang, Y. S., … Yang, C. C. (2017). Microstructure and mechanical properties of open-cell porous Ti-6Al- 4V fabricated by selective laser melting. *Journal of Alloys and Compounds*, *713*, 248–254. https://doi.org/10.1016/j.jallcom.2017.04.190

72. Bagheri, Z. S., Melancon, D., Liu, L., Johnston, R. B., & Pasini, D. (2017). Compensation strategy to reduce geometry and mechanics mismatches in porous biomaterials built with Selective Laser Melting. *Journal of the Mechanical Behavior of Biomedical Materials*, *70*, 17–27. https://doi.org/10.1016/j.jmbbm.2016.04.041

73. Bobyn, J. D., Stackpool, G. J., Hacking, S. A., Tanzer, M., & Krygier, J. J. (1999).

Characteristics of bone ingrowth and interface mechanics of a new porous tantalum biomaterial. *journal of bone and joint surgery*, *81-B*(5), 907–914.

74. Mullen, L., Stamp, R. C., Fox, P., Jones, E., Ngo, C., & Sutcliffe, C. J. (2009). Selective Laser Melting : A Unit Cell Approach for the Manufacture of Porous , Titanium , Bone In-Growth Constructs , Suitable for Orthopedic Applications . *Journal of Biomedical Materials Research Part B: Applied Biomaterials*, *92B*(1), 178–188. https://doi.org/10.1002/jbm.b.31504

75. Limmahakhun, S., Oloyede, A., Sitthiseripratip, K., Xiao, Y., & Yan, C. (2016). Stiffness and strength tailoring ofcobalt chromium graded cellular structures for stress-shielding reduction. *Materials & Design*, *114*, 633–641. https://doi.org/10.1016/j.matdes.2016.11.090

76. Limmahakhun, S., Oloyede, A., Sitthiseripratip, K., Xiao, Y., & Yan, C. (2017). Title: 3D−printed cellular structures for bone biomimetic implants. *Additive Manufacturing*, *15*, 93–101. https://doi.org/10.1016/j.addma.2017.03.010

77. Bael, S. Van, Chai, Y. C., Truscello, S., Moesen, M., Kerckhofs, G., & Oosterwyck, H. Van. (2012). The effect of pore geometry on the in vitro biological behavior of human periosteum-derived cells seeded on selective laser-melted Ti6Al4V bone scaffolds. *Acta Biomaterialia*, *8*(7), 2824–2834. https://doi.org/10.1016/j.actbio.2012.04.001

78. MahamoodEsther, R. M., & Akinlabi, T. (2017). *Functionally Graded Materials*. Springer International Publishing. https://doi.org/10.1007/978-3-319-53756-6

79. Han, C., Li, Y., Wang, Q., Wen, S., Wei, Q., Yan, C., & Hao, L. (2018). Continuous functionally graded porous titanium scaffolds manufactured by selective laser melting for bone implants. *Journal of the Mechanical Behavior of Biomedical Materials*, *80*(January), 119–127. https://doi.org/10.1016/j.jmbbm.2018.01.013

80. Boyer, R. R., & Briggs, R. D. (2005). The Use of Titanium Alloys in the Aerospace Industry. *Journal of Materials Engineering and Performance*, *22*(October), 2916–2920. https://doi.org/10.1007/s11665-013-0728-3

81. Taddei, E. B., Henriques, V. A. R., Silva, C. R. M., & Cairo, C. A. A. (2004). Production

of new titanium alloy for orthopedic implants. *Materials Science & Engineering C*, *24*, 683–687. https://doi.org/10.1016/j.msec.2004.08.011

82. JL, D. (1996). Vanadium: A review of the reproductive and developmental toxicity. *Reproductive Toxicology*, *I*(3), 175–182. https://doi.org/10.1016/0890-6238(96)00019-6

83. Bondy, S. C. (2010). NeuroToxicology The neurotoxicity of environmental aluminum is still an issue. *Neurotoxicology*, *31*(5), 575–581. https://doi.org/10.1016/j.neuro.2010.05.009

84. Bondy, S. C., & Bondy, S. C. (2016). Low levels of aluminum can lead to behavioral and morphological changes associated with Alzheimer's disease and age-related neurodegeneration. *Neurotoxicology*, *52*, 222–229. https://doi.org/10.1016/j.neuro.2015.12.002

85. Ma, L. W., Cheng, H. S., & Chung, C. Y. (2013). Effect of thermo-mechanical treatment on superelastic behavior of Ti e 19Nb e 14Zr ( at .%) shape memory alloy. *Intermetallics*, *32*, 44–50. https://doi.org/10.1016/j.intermet.2012.07.024

86. Laheurte, P., Prima, F., Eberhardt, A., Gloriant, T., Wary, M., & Patoor, E. (2010). Mechanical properties of low modulus β titanium alloys designed from the electronic approach. *Journal of the Mechanical Behavior of Biomedical Materials*, *3*(8), 565–573. https://doi.org/10.1016/j.jmbbm.2010.07.001

87. Liu, Q., Meng, Q., Guo, S., & Zhao, X. (2013). Progress in Natural Science : Materials International α ′ Type Ti – Nb – Zr alloys with ultra-low Young ' s modulus and high strength. *Progress in Natural Science: Materials International*, *23*(6), 562–565. https://doi.org/10.1016/j.pnsc.2013.11.005

88. Hao, Y. L., Li, S. J., Sun, S. Y., Zheng, C. Y., & Yang, R. (2007). Elastic deformation behaviour of Ti – 24Nb – 4Zr – 7 . 9Sn for biomedical applications. *Acta Biomaterialia*, *3*, 277–286. https://doi.org/10.1016/j.actbio.2006.11.002

89. Bertrand, E., Gloriant, T., Gordin, D. M., Vasilescu, E., Drob, P., Vasilescu, C., & Drob, S. I. (2010). Synthesis and characterisation of a new superelastic Ti – 25Ta – 25Nb biomedical alloy. *Journal of the Mechanical Behavior of Biomedical Materials*, *3*(8), 559–

564. https://doi.org/10.1016/j.jmbbm.2010.06.007

90. Zhou, Y., & Niinomi, M. (2009). Ti – 25Ta alloy with the best mechanical compatibility in Ti – Ta alloys for biomedical applications. *Materials Science & Engineering C*, *29*(3), 1061–1065. https://doi.org/10.1016/j.msec.2008.09.012

91. Zhao, C., Zhang, X., & Cao, P. (2011). Mechanical and electrochemical characterization of Ti – 12Mo – 5Zr alloy for biomedical application. *Journal of Alloys and Compounds*, *509*(32), 8235–8238. https://doi.org/10.1016/j.jallcom.2011.05.090

92. Majumdar, P., Singh, S. B., & Chakraborty, M. (2008). Elastic modulus of biomedical titanium alloys by nano-indentation and ultrasonic techniques — A comparative study. *Materials Science and Engineering A*, *489*, 419–425. https://doi.org/10.1016/j.msea.2007.12.029

93. Gu, Y. W., Loh, N. H., Khor, K. A., Tor, S. B., & Cheang, P. (2002). Spark plasma sintering of hydroxyapatite powders. *Biomaterials*, *23*, 37–43. https://doi.org/10.1016/S0142-9612(01)00076-X

94. Singh, G., Singh, S., & Prakash, S. (2011). Surface & Coatings Technology Surface characterization of plasma sprayed pure and reinforced hydroxyapatite coating on Ti6Al4V alloy. *Surface & Coatings Technology*, *205*(20), 4814–4820. https://doi.org/10.1016/j.surfcoat.2011.04.064

95. Kaya, B. C., Singh, I., & Boccaccini, A. R. (2008). Multi-walled Carbon Nanotube-Reinforced Hydroxyapatite Layers on Ti6Al4V Medical Implants by Electrophoretic Deposition ( EPD ). *Advanced Engineering Materials*, *10*(1–2), 131–138. https://doi.org/10.1002/adem.200700241

96. Vilotijevic, M., Markovi, P., Jokanovi, V., Marinkovi, S., & Jokanovi, V. (2011). Hydroxyapatite coatings prepared by a high power laminar plasma jet. *Journal of Materials Processing Technology*, *211*, 996–1004. https://doi.org/10.1016/j.jmatprotec.2010.12.018

97. Inthong, S., Kamnoy, M., Intatha, U., Intawin, P., Pengpat, K., Tunkasiri, T., & Eitssayeam, S. (2018). Phase, mechanical and bioactivity properties of hydroxyapatite-

calcium titanate composite. *Materials Research Express*, *6*(2). https://doi.org/10.1088/2053-1591/aaeec2

98. Kutbay, I., Evis, Z., & Usta, M. (2013). Effect of YF 3 on the phase stability and sinterability of hydroxyapatite — Partially stabilized zirconia composites. *Ceramics International*, *39*, 7869–7877. https://doi.org/10.1016/j.ceramint.2013.03.048

99. Yilmaz, B., Evis, Z., & Usta, M. (2014). Effect of calcium fl uoride on mechanical behavior and sinterability of nano-hydroxyapatite and titania composites. *CeramicsInternational*, *40*(9), 14817–14826. https://doi.org/10.1016/j.ceramint.2014.06.075

100. Santhanakrishnan, S., Ho, Y. H., & Dahotre, N. B. (2016). Laser coating of hydroxyapatite on Mg for enhanced physiological corrosion resistance and biodegradability Laser coating of hydroxyapatite on Mg for enhanced physiological corrosion resistance and biodegradability. *Materials Technology Advanced*, *7857*(March), 273–277. https://doi.org/10.1179/1753555712Y.0000000022

101. Biemond, J. E., Hannink, G., Verdonschot, N., & Buma, P. (2013). Bone ingrowth potential of electron beam and selective laser melting produced trabecular-like implant surfaces with and without a biomimetic coating. *Journal of Materials Science: Materials in Medicine*, *24*(3), 745–753. https://doi.org/10.1007/s10856-012-4836-7

102. Zhang, M. Y., Ye, C., Erasquin, U. J., Huynh, T., Cai, C., & Cheng, G. J. (2011). Laser Engineered Multilayer Coating of Biphasic Calcium Phosphate / Titanium Nanocomposite on Metal Substrates. *ACS Applied Materials & Interfaces*, *3*(2), 339–350. https://doi.org/10.1021/am100962m

103. Wei, Q., Li, S., Han, C., Li, W., Cheng, L., Hao, L., & Shi, Y. (2015). Selective laser melting of stainless-steel/nano-hydroxyapatite composites for medical applications: microstructure, element distribution, crack and mechanical properties. *Journal of Materials Processing Tech.*, *222*, 444–453. https://doi.org/10.1016/j.jmatprotec.2015.02.010

104. Hao, L., Dadbakhsh, S., Seaman, O., & Felstead, M. (2009). Selective laser melting of a

stainless steel and hydroxyapatite composite for load-bearing implant development. *Journal of Materials Processing Technology*, *209*(17), 5793–5801. https://doi.org/10.1016/j.jmatprotec.2009.06.012

105. Han, C., Li, Y., Wang, Q., Cai, D., Wei, Q., Yang, L., … Shi, Y. (2017). Titanium/hydroxyapatite (Ti/HA) gradient materials with quasi-continuous ratios fabricated by SLM: material interface and fracture toughness. *Materials & Design*, *141*, 256–266. https://doi.org/10.1016/j.matdes.2017.12.037

106. Han, C., Wang, Q., Song, B., Li, W., Wei, Q., Wen, S., … Shi, Y. (2017). Microstructure and property evolutions of titanium/nano-hydroxyapatite composites in-situ prepared by selective laser melting. *Journal of the Mechanical Behavior of Biomedical Materials*, *71*, 85–94. https://doi.org/10.1016/j.jmbbm.2017.02.021

107. Donachie, M. J. (2000). *Titanium: A Technical Guide: ASM International*.

108. Vilaro, T., Colin, C., & Bartout, J. D. (2011). As-Fabricated and Heat-Treated Microstructures of the Ti-6Al-4V Alloy Processed by Selective Laser Melting. *Metallurgical and Materials Transactions A*, *42*(10), 3190–3199. https://doi.org/10.1007/s11661-011-0731-y

109. Song, B., Zhao, X., Li, S., Han, C., Wei, Q., Wen, S., … Shi, Y. (2015). Differences in microstructure and properties between selective laser melting and traditional manufacturing for fabrication of metal parts : A review. *Frontiers of Mechanical Engineering*, *10*(2), 111–125. https://doi.org/10.1007/s11465-015-0341-2

110. Sallica-Leva, E., Jardini, A. L., & Fogagnolo, J. B. (2013). Microstructure and mechanical behavior of porous Ti-6Al-4V parts obtained by selective laser melting. *Journal of the Mechanical Behavior of Biomedical Materials*, *26*, 98–108. https://doi.org/10.1016/j.jmbbm.2013.05.011

111. Qiu, C., Adkins, N. J. E., & Attallah, M. M. (2013). Microstructure and tensile properties of selectively laser-melted and of HIPed laser-melted Ti-6Al-4V. *Materials Science and Engineering A*, *578*, 230–239. https://doi.org/10.1016/j.msea.2013.04.099

112. Xu, W., Brandt, M., Sun, S., Elambasseril, J., Liu, Q., Latham, K., … Qian, M. (2015).

Additive manufacturing of strong and ductile Ti–6Al–4V by selective laser melting via in situ martensite decomposition. *Acta Materialia*, *85*, 74–84. https://doi.org/10.1016/j.actamat.2014.11.028

113. Fotovvati, B., Namdari, N., & Dehghanghadikolaei, A. (2018). Fatigue performance of selective laser melted Ti6Al4V components: state of the art. *Materials Research Express*, *6*(1). https://doi.org/10.1088/2053-1591/aae10e

114. Attar, H., Ehtemam-haghighi, S., Wu, X., & Dargusch, M. S. (2017). Comparative study of commercially pure titanium produced by laser engineered net shaping, selective laser melting and casting processes. *Materials Science & Engineering A*, *705*, 385–393. https://doi.org/10.1016/j.msea.2017.08.103

115. Wysocki, B., Maj, P., Krawczyńska, A., Rożniatowski, K., Zdunek, J., Kurzydłowski, K. J., & Święszkowski, W. (2016). Microstructure and mechanical properties investigation of CP Titanium processed by Selective Laser Melting (SLM). *Journal of Materials Processing Tech.*, *241*, 13–23. https://doi.org/10.1016/j.jmatprotec.2016.10.022

116. Chlebus, E., Kurzynowski, T., & Dyba, B. (2011). Microstructure and mechanical behaviour of Ti — 6Al — 7Nb alloy produced by selective laser melting. *Materials Characterization*, *62*(5), 3–10. https://doi.org/10.1016/j.matchar.2011.03.006

117. Murr, L. E., Quinones, S. A., Gaytan, S. M., Lopez, M. I., Rodela, A., Martinez, E. Y., … Wicker, R. B. (2009). Microstructure and mechanical behavior of Ti-6Al-4V produced by rapid-layer manufacturing, for biomedical applications. *Journal of the Mechanical Behavior of Biomedical Materials*, *2*(1), 20–32. https://doi.org/10.1016/j.jmbbm.2008.05.004

118. Facchini, L., Magalini, E., Robotti, P., Molinari, A., Höges, S., Wissenbach, K., … Facchini, L. (2011). Ductility of a Ti-6Al-4V alloy produced by selective laser melting of prealloyed powders. *Rapid Prototyping Journal*, *16*(6), 450–459. https://doi.org/10.1108/13552541011083371

119. Vrancken, B., Thijs, L., Kruth, J. P., & Van Humbeeck, J. (2012). Heat treatment of Ti6Al4V produced by Selective Laser Melting: Microstructure and mechanical properties.

*Journal of Alloys and Compounds*, *541*, 177–185. https://doi.org/10.1016/j.jallcom.2012.07.022

120. Sallica-leva, E., Caram, R., Jardini, A. L., & Fogagnolo, J. B. (2016). Ductility improvement due to martensite α 0 decomposition in porous Ti – 6Al – 4V parts produced by selective laser melting for orthopedic implants. *Journal of the Mechanical Behavior of Biomedical Materials*, *54*, 149–158. https://doi.org/10.1016/j.jmbbm.2015.09.020

121. Xu, W., Lui, E. W., Pateras, A., Qian, M., & Brandt, M. (2017). In situ tailoring microstructure in additively manufactured Ti-6Al-4V for superior mechanical performance. *Acta Materialia*, *125*, 390–400. https://doi.org/10.1016/j.actamat.2016.12.027

122. Debroy, T., Wei, H. L., Zuback, J. S., Mukherjee, T., Elmer, J. W., Milewski, J. O., … Zhang, W. (2018). Additive manufacturing of metallic components – Process , structure and properties. *Progress in Materials Science*, *92*, 112–224. https://doi.org/10.1016/j.pmatsci.2017.10.001

123. Motyka, M., Kubiak, K., Sieniawski, J., & Ziaja, W. (2014). Phase Transformations and Characterization of α + β Titanium Alloys. In *Comprehensive Materials Processing* (Vol. 2, pp. 7–36). Elsevier. https://doi.org/10.1016/B978-0-08-096532-1.00202-8

124. Jaber, H., Kónya, J., & Kovács, T. A. (2021). Selective laser melting of ti6al4v-2%hydroxyapatite composites: Manufacturing behavior and microstructure evolution. *Metals*, *11*(8), 1–15. https://doi.org/10.3390/met11081295

125. Jaber, H., Kovacs, T., & János, K. (2020). Investigating the impact of a selective laser melting process on Ti6Al4V alloy hybrid powders with spherical and irregular shapes. *Advances in Materials and Processing Technologies*. https://doi.org/10.1080/2374068X.2020.1829960

126. Vrancken, B. (2016). *Study of Residual Stresses in Selective Laser Melting Supervisor:* KU Leuven.

127. Leuders, S., Thöne, M., Riemer, A., Niendorf, T., Tröster, T., Richard, H. A., & Maier, H. J. (2013). On the mechanical behaviour of titanium alloy TiAl6V4 manufactured by

selective laser melting : Fatigue resistance and crack growth performance. *International Journal of Fatigue*, *48*, 300–307. https://doi.org/10.1016/j.ijfatigue.2012.11.011

128. Standard Specification for Wrought Titanium-6Aluminum-4Vanadium ELI (Extra Low Interstitial) Alloy for Surgical Implant Applications (UNS R56401). (2013). *ASTM International F136-13*. https://doi.org/10.1520/F0136-13.2

129. Standard Specification for Additive Manufacturing Titanium-6 Aluminum-4 Vanadium with Powder Bed Fusion 1. (2014). *ASTM International : F2924-14*, *i*, 1–9. https://doi.org/10.1520/F2924-14.2

130. Ali, H., Ma, L., Ghadbeigi, H., & Mumtaz, K. (2017). In-situ residual stress reduction , martensitic decomposition and mechanical properties enhancement through high temperature powder bed pre-heating of Selective Laser Melted Ti6Al4V. *Materials Science & Engineering A*, *695*(February), 211–220. https://doi.org/10.1016/j.msea.2017.04.033

131. Vrancken, B., Thijs, L., Kruth, J., & Humbeeck, J. Van. (2014). ScienceDirect Microstructure and mechanical properties of a novel b titanium metallic composite by selective laser melting. *Acta Materialia*, *68*, 150–158. https://doi.org/10.1016/j.actamat.2014.01.018

132. Muhammad, M., Pegues, J. W., Shamsaei, N., & Haghshenas, M. (2019). Effect of heat treatments on microstructure / small-scale properties of additive manufactured Ti-6Al-4V. *The International Journal of Advanced Manufacturing Technology*, *103*(9–12), 4161–4172. https://doi.org/10.1007/s00170-019-03789-w

133. Guo, Z., Malinov, S., & Sha, W. (2005). Modelling beta transus temperature of titanium alloys using artificial neural network. *Computational Materials Science*, *32*(1), 1–12. https://doi.org/10.1016/j.commatsci.2004.05.004

134. ASTM: E407. (2016). Standard Practice for Microetching Metals and Alloys 1. *ASTM International*. https://doi.org/10.1520/E0407-07R15E01.2

135. Malinov, S., Sha, W., Guo, Z., Tang, C. C., & Long, A. E. (2002). Synchrotron X-ray diffraction study of the phase transformations in titanium alloys. *Materials*

*Characterization*, *48*(4), 279–295. https://doi.org/10.1016/S1044-5803(02)00286-3

136. Kazantseva, N., Krakhmalev, P., Thuvander, M., Yadroitsev, I., Vinogradova, N., & Ezhov, I. (2018). Martensitic transformations in Ti-6Al-4V (ELI) alloy manufactured by 3D Printing. *Materials Characterization*, *146*(September), 101–112. https://doi.org/10.1016/j.matchar.2018.09.042

137. Premkumar, M., & Singh, A. K. (2010). Deformation behavior of an ordered B2 phase in Ti-25Al-25Zr alloy. *Intermetallics*, *18*(1), 199–201. https://doi.org/10.1016/j.intermet.2009.07.015

138. Brandl, E., Schoberth, A., & Leyens, C. (2012). Morphology, microstructure, and hardness of titanium (Ti-6Al-4V) blocks deposited by wire-feed additive layer manufacturing (ALM). *Materials Science and Engineering A*, *532*, 295–307. https://doi.org/10.1016/j.msea.2011.10.095

139. Katzarov, I., Malinov, S., & Sha, W. (2002). Finite element modeling of the morphology of β to α phase transformation in Ti-6Al-4V alloy. *Metallurgical and Materials Transactions A*, *33*(4), 1027–1040. https://doi.org/10.1007/s11661-002-0204-4

140. Haar, G. M. Ter, & Becker, T. H. (2018). Selective Laser Melting Produced Ti-6Al-4V : Post-Process Heat Treatments to Achieve Superior Tensile Properties. *Materials*, *11*(1), 1–15. https://doi.org/10.3390/ma11010146

141. Etesami, S. A., Fotovvati, B., & Asadi, E. (2022). Heat treatment of Ti-6Al-4V alloy manufactured by laser-based powder-bed fusion: Process, microstructures, and mechanical properties correlations. *Journal of Alloys and Compounds*, *895*, 162618. https://doi.org/10.1016/j.jallcom.2021.162618

142. Wu, S. Q., Lu, Y. J., Gan, Y. L., Huang, T. T., Zhao, C. Q., Lin, J. J., … Lin, J. X. (2016). Microstructural evolution and microhardness of a selective-laser-melted Ti-6Al-4V alloy after post heat treatments. *Journal of Alloys and Compounds*, *672*, 643–652. https://doi.org/10.1016/j.jallcom.2016.02.183

143. Lütjering G, Williams, J. C. (2006). *Titanium* (2nd ed.). Berlin: Springer.

144. Smallman, R. E., & Ngan, A. H. W. (2007). Case examination of biomaterials, sports

materials and nanomaterials. In R. E. Smallman & A. H. W. Ngan (Eds.), *Physical Metallurgy and Advanced Materials Engineering* (7th ed., pp. 583–621). Elsevier Ltd. https://doi.org/10.1016/B978-075066906-1/50015-9

145. Ke, D., Vu, A. A., Bandyopadhyay, A., & Bose, S. (2019). Compositionally graded doped hydroxyapatite coating on titanium using laser and plasma spray deposition for bone implants. *Acta Biomaterialia*, *84*(15 January), 414–423. https://doi.org/10.1016/j.actbio.2018.11.041

146. Limmahakhun, S. (2017). *DEVELOPMENT OF FUNCTIONALLY GRADED MATERIALS FOR INNOVATION IN BONE - REPLACEMENT APPLICATIONS*. Queensland University of Technology.

147. Vasconcellos, L. M. R., Oliveira, M. V., Graça, M. L. A., Vasconcellos, L. G. O., Cairo, C. A. A., & Carvalho, Y. R. (2008). Design of dental implants, influence on the osteogenesis and fixation. *Journal of Materials Science: Materials in Medicine*, *19*(8), 2851–2857. https://doi.org/10.1007/s10856-008-3421-6

148. Yousefi, A. M. (2019). A review of calcium phosphate cements and acrylic bone cements as injectable materials for bone repair and implant fixation. *Journal of Applied Biomaterials and Functional Materials*, *17*(4). https://doi.org/10.1177/2280800019872594

149. Mohseni, E., Zalnezhad, E., & Bushroa, A. R. (2014). Comparative investigation on the adhesion of hydroxyapatite coating on Ti-6Al-4V implant: A review paper. *International Journal of Adhesion and Adhesives*, *48*(January), 238–257. https://doi.org/10.1016/j.ijadhadh.2013.09.030

150. Peñarrieta-Juanito, G., Sordi, M. B., Henriques, B., Dotto, M. E. R., Teughels, W., Silva, F. S., … Souza, J. C. M. (2019). Surface damage of dental implant systems and ions release after exposure to fluoride and hydrogen peroxide. *Journal of Periodontal Research*, *54*(1), 46–52. https://doi.org/10.1111/jre.12603

151. Marcu, T., Menapace, C., Girardini, L., Leordean, D., & Popa, C. (2014). Selective laser melting of Ti6Al7Nb with hydroxyapatite addition. *Rapid Prototyping Journal*, *20*(4), 301–310. https://doi.org/10.1108/RPJ-09-2012-0083

152. Nath, S., Tripathi, R., & Basu, B. (2009). Understanding phase stability, microstructure development and biocompatibility in calcium phosphate-titania composites, synthesized from hydroxyapatite and titanium powder mix. *Materials Science and Engineering C*, *29*(1), 97–107. https://doi.org/10.1016/j.msec.2008.05.019

153. Terrazas, A., Murr, L. E., Arrieta, E., Roberson, D. A., & Wicker, R. B. (2019). Microstructure and mechanical properties of Ti-6Al-4V-5% hydroxyapatite composite fabricated using electron beam powder bed fusion. *Journal of Materials Science & Technology*, *35*(February), 309–321. https://doi.org/10.1016/j.jmst.2018.10.025

154. Liu, B., Deng, Z., & Liu, D. (2021). Preparation and properties of multilayer Ca/P bio-ceramic coating by laser cladding. *Coatings*, *11*(8), 1–17. https://doi.org/10.3390/coatings11080891

155. Takeuchi, A., & Inoue, A. (2005). Classification of Bulk Metallic Glasses by Atomic Size Difference, Heat of Mixing and Period of Constituent Elements and Its Application to Characterization of the Main Alloying Element. *Materials Transactions*, *46*(12), 2817–2829. https://doi.org/10.2320/matertrans.46.2817

156. Okamoto, H. (2011). O-Ti (Oxygen-Titanium). *Journal of Phase Equilibria and Diffusion*, *32*(5), 473–474. https://doi.org/10.1007/s11669-011-9935-5

157. Shishkovsky, I. V., Tarasova, E. Y., Zhuravel', L. V., & Petrov, A. L. (2001). The synthesis of a biocomposite based on nickel titanium and hydroxyapatite under selective laser sintering conditions. *Technical Physics Letters*, *27*(3), 211–213. https://doi.org/10.1134/1.1359830

158. Shifeng, W., Shuai, L., Qingsong, W., Yan, C., Sheng, Z., & Yusheng, S. (2014). Effect of molten pool boundaries on the mechanical properties of selective laser melting parts. *Journal of Materials Processing Technology*, *214*(11), 2660–2667. https://doi.org/10.1016/j.jmatprotec.2014.06.002

159. Yan, X., Yin, S., Chen, C., Huang, C., Bolot, R., Lupoi, R., … Liu, M. (2018). Effect of heat treatment on the phase transformation and mechanical properties of Ti6Al4V fabricated by selective laser melting. *Journal of Alloys and Compounds*, *764*(5 October),

1056–1071. https://doi.org/10.1016/j.jallcom.2018.06.076

160. Kutz, M. (2003). *Standard Handbook of Biomedical Engineering and Design*. *Bioengineering*. McGraw-Hill Professional.

161. Gong, H., Ra, K., Gu, H., Ram, G. D. J., Starr, T., & Stucker, B. (2015). Influence of defects on mechanical properties of Ti–6Al–4 V components produced by selective laser melting and electron beam melting. *Materials and Design*, *86*, 545–554. https://doi.org/10.1016/j.matdes.2015.07.147

162. Han, J., Yang, J., Yu, H., Jie Yin, M. G., Wang, Z., & Zeng, X. (2017). Microstructure and mechanical property of selective laser melted Ti6Al4V dependence on laser energy density. *Rapid Prototyping Journal*, *23*(2), 217–226. https://doi.org/10.1108/RPJ-12-2015-0193

163. Kasperovich, G., Haubrich, J., Gussone, J., & Requena, G. (2016). Correlation between porosity and processing parameters in TiAl6V4 produced by selective laser melting. *Materials and Design*, *105*, 160–170. https://doi.org/10.1016/j.matdes.2016.05.070

164. Yang, J., Yu, H., Yin, J., Gao, M., Wang, Z., & Zeng, X. (2016). Formation and control of martensite in Ti-6Al-4V alloy produced by selective laser melting. *Materials and Design*, *108*, 308–318. https://doi.org/10.1016/j.matdes.2016.06.117

165. Mumtaz, K. A., Erasenthiran, P., & Hopkinson, N. (2008). High density selective laser melting of Waspaloy®. *Journal of Materials Processing Technology*, *195*(1–3), 77–87. https://doi.org/10.1016/j.jmatprotec.2007.04.117

166. Song, B., Dong, S., Zhang, B., Liao, H., & Coddet, C. (2012). Effects of processing parameters on microstructure and mechanical property of selective laser melted Ti6Al4V. *Materials and Design*, *35*, 120–125. https://doi.org/10.1016/j.matdes.2011.09.051

167. Do, D. K., & Li, P. (2016). The effect of laser energy input on the microstructure , physical and mechanical properties of Ti-6Al-4V alloys by selective laser melting. *Virtual and Physical Prototyping*, *2759*(March), 41–47. https://doi.org/10.1080/17452759.2016.1142215

168. Weiwei, H., Wenpeng, J., Haiyan, L., Huiping, T., Xinting, K., & Yu, H. (2011). Research

on Preheating of Titanium Alloy Powder in Elec- tron Beam Melting Technology. *Rare Metal Materials and Engineering*, *40*(12), 2072–2075. https://doi.org/10.1016/S1875-5372(12)60014-9

169. Vrancken, B., Buls, S., Kruth, J.-P., & Van Humbeeck, J. (5015). Influence of preheating and oxygen content on selective laser melting of Ti6Al4V. In *Proceedings of the 16th RAPDASA Conference. RAPDASA, Annual International Conference on Rapid Product Development Association of South Africa 4–6* (pp. 1–10).

170. Verhaeghe, F., Craeghs, T., Heulens, J., & Pandelaers, L. (2009). A pragmatic model for selective laser melting with evaporation. *Acta Materialia*, *57*(20), 6006–6012. https://doi.org/10.1016/j.actamat.2009.08.027

171. Tang, H. P., Qian, M., Liu, N., Zhang, X. Z., Yang, G. Y., & Wang, J. (2015). Effect of Powder Reuse Times on Additive Manufacturing of Ti-6Al-4V by Selective Electron Beam Melting. *The Journal of The Minerals, Metals & Materials Society(JOM)*, *67*(3). https://doi.org/10.1007/s11837-015-1300-4

172. Sames, W. J., List, F. A., Pannala, S., Dehoff, R. R., & Babu, S. S. (2016). The metallurgy and processing science of metal additive manufacturing. *International Materials Reviews*, *61*(5), 1–47. https://doi.org/10.1080/09506608.2015.1116649

173. Sutton, A. T., Kriewall, C. S., Leu, M. C., & Newkirk, J. W. (2016). Powder characterisation techniques and effects of powder characteristics on part properties in powder-bed fusion processes. *Virtual and Physical Prototyping*, *2759*(December), 1–27. https://doi.org/10.1080/17452759.2016.1250605

174. ASTM B213-17. (2017). Standard Test Methods for Flow Rate of Metal Powders Using the Hall Flowmeter Funnel. *ASTM International*, 1–4. https://doi.org/10.1520/B0213-17.2

175. Data sheet of Ti-6Al-4V alloy Powder for Additive Manufacturing. (n.d.). *Toho titanium co. ltd/Japan*.

176. Kanou, O., Fukada, N., & Takenaka, S. (2017). The Use of HDH Titanium Alloy Powder for Additive Manufacturing Application. *Journal of the Japan Society of Powder and Powder Metallurgy*, *64*(6), 295–299. https://doi.org/10.2497/jjspm.64.295

177. Vock, S., Klöden, B., Kirchner, A., Weißgärber, T., & Kieback, B. (2019). Powders for powder bed fusion: a review. *Progress in Additive Manufacturing*, *4*(3), 1–15. https://doi.org/10.1007/s40964-019-00078-6

178. Jacob, G., Brown, C., Donmez, A., Watson, S., & Slotwinski, J. (2017). Effects of powder recycling on stainless steel powder and built material properties in metal powder bed fusion processes. *NIST Advanced Manufacturing Series 100-6 stainless (National Institute of Standards and Technology)*. https://doi.org/10.6028/NIST.AMS.100-6

179. Slotwinski, J. A., & Garboczi, E. J. (2015). Metrology Needs for Metal Additive Manufacturing Powders. *Jom*, *67*(3), 538–543. https://doi.org/10.1007/s11837-014-1290-7

180. Japanese Industrial Standard. (2012). Metallic powders-Determination of flow rate by means of a calibrated funnel (Hall flowmeter). *JIS Z 2502*.

181. ASTM International. (2017). B212-13: Standard Test Method for Apparent Density of Free-Flowing Metal Powders Using the Hall Flowmeter Funnel 1. *ASTM International*. https://doi.org/10.1520/B0212-17.2

182. Sun, Y. Y., Gulizia, S., Oh, C. H., Doblin, C., Yang, Y. F., & Qian, M. (2015). Manipulation and Characterization of a Novel Titanium Powder Precursor for Additive Manufacturing Applications. *The Journal of The Minerals, Metals & Materials Society (JOM)*, *67*(3), 11–15. https://doi.org/10.1007/s11837-015-1301-3

183. McCracken, C. G., Motchenbacher, C., & Barbis, D. P. (2010). Review of Titanium-Powder-Production Methods. *International Journal of Powder Metallurgy*, *46*(5), 19–26.

184. Froes FH (Sam). (2015). *Titanium physical metallurgy, processing and applications*. OH:ASM, Materials Park.

185. Froes, F. H. S. (2015). *Titanium Powder Metallurgy Science, Technology and Applications*. Elsevier Inc.

186. M.Bram, T.Ebel, M.Wolff, Barbosa, A. P. C., & N.Tuncer. (2013). Applications of powder metallurgy in biomaterials. In I. Chang & Y. Zhao (Eds.), *Advances in powder metallurgy* (p. 536). Woodhead Publishing. https://doi.org/10.1533/9780857098900.4.520

187. ELMER, J. W., VAJA, J., CARLTON, H. D., & PONG, R. (2015). The Effect of Ar and N 2 Shielding Gas on Laser Weld Porosity in Steel , Stainless Steels , and Nickel. *Welding Journal*, *94*(October), 313–325.

188. Bauereiß, A., Scharowsky, T., & Körner, C. (2014). Defect generation and propagation mechanism during additive manufacturing by selective beam melting. *Journal of Materials Processing Technology*, *214*(11), 2522–2528. https://doi.org/10.1016/j.jmatprotec.2014.05.002

189. Wu, M. W., & Lai, P. H. (2016). The positive effect of hot isostatic pressing on improving the anisotropies of bending and impact properties in selective laser melted Ti-6Al-4V alloy. *Materials Science and Engineering A*, *658*, 429–438. https://doi.org/10.1016/j.msea.2016.02.023

190. Li, P., Warner, D. H., Pegues, J. W., Roach, M. D., Shamsaei, N., & Phan, N. (2019). Investigation of the mechanisms by which hot isostatic pressing improves the fatigue performance of powder bed fused Ti-6Al-4V. *International Journal of Fatigue*, *120*(March 2019), 342–352. https://doi.org/10.1016/j.ijfatigue.2018.10.015

191. Wauthle, R., Vrancken, B., Beynaerts, B., Jorissen, K., Schrooten, J., Kruth, J. P., & Van Humbeeck, J. (2015). Effects of build orientation and heat treatment on the microstructure and mechanical properties of selective laser melted Ti6Al4V lattice structures. *Additive Manufacturing*, *5*(January 2015), 77–84. https://doi.org/10.1016/j.addma.2014.12.008

192. Li, P., Guo, W., Huang, W., Su, Y., Lin, X., & Yuan, K. (2015). Thermomechanical response of 3D laser-deposited Ti – 6Al – 4V alloy over a wide range of strain rates and temperatures. *Materials Science & Engineering A*, *647*, 34–42. https://doi.org/10.1016/j.msea.2015.08.043

193. Hrabe, N., Gnäupel-herold, T., & Quinn, T. (2017). Fatigue Properties of a Titanium Alloy (Ti-6Al-4V) Fabricated Via Electron Beam Melting (EBM): Effects of Internal Defects and Residual Stress. *International journal of fatigue*, *94*(2), 202–210. https://doi.org/10.1016/j.ijfatigue.2016.04.022

194. Yadroitsev, I., Krakhmalev, P., & Yadroitsava, I. (2013). Selective laser melting of

Ti6Al4V alloy for biomedical applications: temperature monitoring and microstructural evolution. *Journal of Alloys and Compounds*, *583*(15 January), 404–409. https://doi.org/10.1016/j.jallcom.2013.08.183

195. Sun, J., Yang, Y., & Wang, D. (2013). Mechanical Properties of a Ti6Al4V Porous Structure Produced by Selective Laser Melting. *Materials & Design*, *49*(August), 545–552. https://doi.org/10.1016/j.matdes.2013.01.038

196. Thijs, L., Verhaeghe, F., Craeghs, T., Humbeeck, J. Van, & Kruth, J. P. (2010). A study of the microstructural evolution during selective laser melting of Ti-6Al-4V. *Acta Materialia*, *58*(9), 3303–3312. https://doi.org/10.1016/j.actamat.2010.02.004

197. Boyer, R., & Welsch, G. (1994). *Materials Properties Handbook : Titanium Alloys*. Materials Park (OH): ASM International.

198. Persson, K. Materials Data on Ti3Al (SG:194) by Materials Project. , United States (2016). https://doi.org/10.17188/1192999

199. Zhang, S., Wei, Q., Cheng, L., Li, S., & Shi, Y. (2014). Effects of scan line spacing on pore characteristics and mechanical properties of porous Ti6Al4V implants. *Materials & Design*, *63*(November), 185–193. https://doi.org/10.1016/j.matdes.2014.05.021